

## **Studies of Nonlinear QED in Collisions of 46.6 GeV Electrons with Intense Laser Pulses\***

C. Bamber,<sup>†</sup> S.J. Boege,<sup>‡</sup> T. Koffas, T. Kotseroglou,<sup>§</sup> A.C. Melissinos, D.D. Meyerhofer,<sup>¶</sup>  
D.A. Reis and W. Ragg<sup>||</sup>

*Department of Physics and Astronomy, University of Rochester  
Rochester, New York 14627*

C. Bula,\*\* K.T. McDonald and E.J. Prebys  
*Joseph Henry Laboratories, Princeton University, Princeton, New Jersey 08544*

D.L. Burke, R.C. Field, G. Horton-Smith,<sup>††</sup> J.E. Spencer and D. Walz  
*Stanford Linear Accelerator Center, Stanford University, Stanford, California 94309*

S.C. Berridge, W.M. Bugg, K. Shmakov<sup>‡‡</sup> and A.W. Weidemann  
*Department of Physics and Astronomy, University of Tennessee  
Knoxville, Tennessee 37996*

---

\*Work supported by Department of Energy contract DE-AC03-76SF00515 and grants DE-FG02-91ER40671, DE-FG02-91ER40685, and DE-FG05-91ER40627.

<sup>†</sup>Present address: ELCAN Optical Technologies Ltd., Midland, Ontario, Canada L4R 2H2.

<sup>‡</sup>Present address: Lawrence Livermore National Laboratory, Livermore, CA 94551.

<sup>§</sup>Present address: Stanford Linear Accelerator Center, Stanford University, Stanford, CA 94309.

<sup>¶</sup>also Department of Mechanical Engineering.

<sup>||</sup>Present address: Panoramastrasse 8, 78589 Durbheim, Germany.

\*\*Present address: Swisslog Software AG, CH-5001 Aarau, Switzerland.

<sup>††</sup>Present address: Research Center for Neutrino Science, Tohoku University, Sendai, Japan 980-0845.

<sup>‡‡</sup>Present address: Globalstar, San Jose, CA 95164.

## Abstract

We report on measurements of quantum electrodynamic processes in an intense electromagnetic wave, where nonlinear effects (both multiphoton and vacuum polarization) are prominent. Nonlinear Compton scattering and electron-positron pair production have been observed in collisions of 46.6 GeV and 49.1 GeV electrons of the Final Focus Test Beam at SLAC with terawatt pulses of 1053 nm and 527 nm wavelengths from a Nd:glass laser. Peak laser intensities of  $\approx 0.5 \times 10^{18}$  W/cm<sup>2</sup> have been achieved, corresponding to a value of  $\approx 0.4$  for the parameter  $\eta = eE_{\text{rms}}/m\omega_0 c$ , and to a value of  $\approx 0.25$  for the parameter  $\Upsilon_e = E_{\text{rms}}^*/E_{\text{crit}} = eE_{\text{rms}}^*\hbar/m^2c^3$ , where  $E_{\text{rms}}^*$  is the rms electric field strength of the laser in the electron rest frame. We present data on the scattered electron spectra arising from nonlinear Compton scattering with up to four photons absorbed from the field. A convolved spectrum of the forward high energy photons is also given. The observed positron production rate depends on the fifth power of the laser intensity, as expected for a process where five photons are absorbed from the field. The positrons are interpreted as arising from the collision of a high-energy Compton scattered photon with the laser beam. The results are found to be in agreement with theoretical predictions.

*Submitted to Physical Review D*

# 1 Introduction

## 1.1 General

Quantum electrodynamics (QED) has been tested extensively in the weak-field regime. It has also been tested in atomic systems with focused laser beams whose electric fields of order  $10^8$  V/cm ( $1$  V/Å) lead to rapid ionization of atoms and other phenomena of nonlinear optics. Here, we report on the observation of two strong-field processes in the interaction of an ultrarelativistic electron beam with a terawatt laser pulse.

The first process is nonlinear Compton scattering, in which an electron absorbs multiple photons from the laser field, but radiates only a single photon:

$$e + n\omega \rightarrow e' + \gamma, \quad (1)$$

where  $\omega$  represents a photon from the strong electromagnetic wave,  $n$  indicates the number of such photons absorbed, and  $\gamma$  represents a high-energy photon. This process has a classical limit, Thomson scattering, and the case of  $n > 1$  corresponds to higher-multipole radiation.

In the second process, one or more of the laser photons is Compton scattered from the electron beam via process (1), producing a high-energy photon. As this photon propagates through the laser field, it can interact to produce an electron-positron pair:

$$\gamma + n\omega \rightarrow e^+e^-, \quad (2)$$

This is referred to as Breit-Wheeler pair production, and can be regarded as the materialization of a vacuum-polarization loop in a strong field.

Our first observations of processes (1) and (2) have been reported in [1] and [2], respectively.

The Introduction continues with general comments on reactions (1) and (2), followed by remarks on this and related experiments. The relevant formalism of strong-field QED is reviewed in sec. 2. Details of the experimental apparatus are presented in sec. 3, and the data analysis procedures are discussed in sec. 4, with additional details in appendices A and B (secs. 8 and 9). Physics results on nonlinear Compton scattering and on pair creation are presented in secs. 5 and 6, respectively, with conclusions in sec. 7.

## 1.2 Nonlinear Compton Scattering

The interaction of free electrons with strong fields has been considered by several authors [3, 4, 5, 6, 7, 8, 9, 10]. Nonlinear Compton scattering, (1), can be understood in terms of the interaction of an electron with a classical plane wave of frequency  $\omega$ . In general, such an electron will exhibit oscillatory motion with a frequency  $\omega$ , and will, in turn, radiate. If the frequency  $\omega^*$  as observed in the rest frame of the electron obeys  $\hbar\omega^* \ll mc^2$ , where  $m$  is the mass of the electron and  $c$  is the speed of light, this process is called Thomson scattering, the classical limit of Compton scattering.

In the weak-field case, the maximum (transverse) velocity reached by an electron at rest prior to the arrival of the wave of peak electric field  $E$  will be

$$v_{\max} = \frac{eE}{m\omega}, \quad (3)$$

where  $e$  is the magnitude of the electron's charge, and the resulting radiation is well described by the dipole approximation. In stronger fields,  $v_{\max}$  approaches  $c$ , and higher multipole radiation becomes significant. The radiated intensity is then a nonlinear function of the intensity of the incident wave. In quantum theory, this can be interpreted as simultaneous absorption by an electron of multiple photons from the field, leading to the emission of a single photon (that is distinguishable from the initial photons).

Thus, nonlinear effects become significant in Compton (and Thomson) scattering when the dimensionless parameter,

$$\eta = \frac{eE_{\text{rms}}}{\omega mc}, \quad (4)$$

approaches or exceeds unity. Here, we have used the rms (root-mean-square), rather than peak, electric field as this provides the most unified description of different wave polarizations. When considered in a different reference frame,  $E_{\text{rms}}$  and  $\omega$  transform in a similar manner, leaving the value of  $\eta$  the same. That is,  $\eta$  can be expressed as a Lorentz invariant, namely

$$\eta^2 \equiv \frac{e^2 |\langle A_\mu A^\mu \rangle|}{m^2}, \quad (5)$$

where the average is taken over one period. In this, the 4-vector potential  $A_\mu$  of the wave must satisfy the Lorentz gauge condition ( $\partial_\mu A^\mu = 0$ ), and have no overall constant term ( $\langle A^\mu \rangle = 0$ ).

For example, in a circularly polarized wave the magnitude of the electric field is constant. A free electron in this wave undergoes circular motion with angular frequency  $\omega$  in the plane transverse to the direction of propagation of the field. The electron's transverse momentum  $P_\perp$  is

$$\frac{P_\perp}{mc} = \frac{eE}{\omega mc} = \eta. \quad (6)$$

Therefore, the total energy  $\mathcal{E}$  of the electron is related by

$$\begin{aligned} \mathcal{E}^2 &= (mc^2)^2 + (P_\parallel c)^2 + (P_\perp c)^2 \\ &= (1 + \eta^2)(mc^2)^2 + (P_\parallel c)^2, \end{aligned} \quad (7)$$

where  $P_\parallel$  is the component of the electron's momentum parallel to the direction of propagation of the wave. Heuristically, one can say that quantum interactions average over the transverse motion, so that the electron behaves as if it had an effective mass [11]

$$\overline{m}^2 = m^2(1 + \eta^2). \quad (8)$$

This behavior is identifiable by a shift in the kinematic edge for Compton scattering, discussed further in sec. 2.2.

### 1.3 Breit-Wheeler Pair Production

Another measure of field strength besides  $\eta$  is relevant to Breit-Wheeler pair production, (2); namely, one that compares the field to the so-called QED critical field.

The concept of a QED critical field was first introduced [12] in connection with Klein's paradox [13], and has since been interpreted in the context of pair creation due to vacuum polarization by a static field [14, 15]. If virtual  $e^+e^-$  pairs in the vacuum acquire enough energy from the field, they may become real, resulting in a “breakdown of the vacuum”. The characteristic separation of the electron and positron of a virtual pair is the Compton wavelength  $\lambda_C \equiv \hbar/mc$ , so a critical field  $E_{\text{crit}}$  is defined by the condition  $eE_{\text{crit}}\lambda_C = mc^2$ . Hence,

$$E_{\text{crit}} = \frac{mc^2}{e\lambda_C} = \frac{m^2c^3}{e\hbar} = 1.3 \times 10^{16} \text{ V/cm}. \quad (9)$$

In the case of a plane-wave field by itself, the invariant  $E^2 - B^2$  vanishes, and spontaneous pair creation cannot occur for any value of the field strength. Nonetheless, if such a field is probed by a particle, pair creation can occur, and the critical field (9) is pertinent to the physical description of the process. The latter circumstance is made plausible by the inverse of the usual Weizsäcker-Williams approximation. That is, some aspects of the interaction of a wave field with a probe particle are similar to those of an equivalent static field in a relevant frame.

In particular, the effect of vacuum polarization on the interaction of an electron or photon of 4-momentum  $p_\mu$  with an electromagnetic wave with 4-tensor  $F_{\mu\nu}$  can be characterized in terms of the dimensionless invariant

$$\Upsilon = \frac{e\hbar}{m^3c^5} \sqrt{\langle (F_{\mu\nu}p^\nu)^2 \rangle}. \quad (10)$$

The invariant  $\Upsilon$  can also be written in terms of the invariant  $\eta$  and the 4-momentum  $k_\mu$  of a photon of the (plane) wave field as

$$\Upsilon = \eta \frac{p \cdot k}{m^2c^4}. \quad (11)$$

Thus, while the invariants  $\eta$  and  $\Upsilon$  can, in general, be varied independently, their ratio is fixed for a particular choice of the 4-momentum  $k$  and  $p$ .

For an electron, the invariant (10) can be evaluated as

$$\Upsilon_e = \frac{E_{\text{rms}}^*}{E_{\text{crit}}}, \quad (12)$$

where  $E^*$  is the electric field strength of the wave in the electron's rest frame.

In process (2), a photon of 4-momentum  $k'_\mu$  interacts with an intense laser pulse. We label the corresponding invariant as

$$\Upsilon_\gamma = \frac{e\hbar}{m^3c^5} \sqrt{\langle (F_{\mu\nu}k'^\nu)^2 \rangle}. \quad (13)$$

In any frame in which the photon and the wave collide head on,  $\Upsilon_\gamma$  can be written in terms of the photon's energy  $\mathcal{E}_\gamma = k'_0$  as

$$\Upsilon_\gamma = \frac{2\mathcal{E}_\gamma}{mc^2} \frac{E_{\text{rms}}}{E_{\text{crit}}}. \quad (14)$$

If  $\mathcal{E}_\gamma \gg mc^2$ , the value of  $\Upsilon_\gamma$  is the same as that of  $\Upsilon_e$  for a wave probed head-on by an electron of energy  $\mathcal{E}_\gamma$ .

The above interpretations are supported by detailed analyses [4, 7, 8] which show that the pair production rate becomes large when  $\Upsilon_\gamma$  approaches unity. Further, if  $\eta \gg 1$ , the pair creation rate has the same functional dependence on  $\Upsilon_\gamma$  as does the “breakdown of the vacuum” by a static electric field on the ratio  $\Upsilon_{\text{static}} = E_{\text{static}}/E_{\text{crit}}$ . See secs. 2.4 and 6.2 for further discussion.

## 1.4 This experiment

In this experiment, we studied the interactions of 527 nm (green) and 1053 nm (infrared = IR) laser pulses with a 46.6 GeV electron beam. We also present some data taken with a 49.1 GeV electron beam.

Since the photon energy in the electron rest frame was comparable to the electron rest mass, recoil effects in reaction (1) were pronounced, and we describe that process as Compton rather than Thomson scattering. The recoil effect in Compton scattering made possible the identification of the (minimum) number of photons absorbed from the laser beam by measurement of the scattered electron energy, as discussed further in sec. 2.2.

Electron-photon scattering in which the initial electron kinetic energy is larger than the initial photon energy, as in our experiment, is called inverse Compton scattering in the astrophysical community. In labelling reaction (1) as Compton scattering, we adopt the view that processes whose descriptions differ only by a Lorentz transformation are fundamentally the same.

The peak values of parameter  $\eta$  were 0.4 for IR pulses, and 0.3 for green pulses, corresponding to  $E_{\text{rms}} \approx 10^{10}$  V/cm. In this regime, nonlinear effects are expected to be prominent, and proved to be so.

For 46.6 GeV electrons, the maximum photon energy from Compton scattering by a single green photon was 29 GeV, and the pair production studies were performed with photons of energy close to this. Single IR photons yielded backscattered photons of energy about 21 GeV, which was unfavorable for pair production in this experiment. For the green laser,  $\Upsilon_e = 0.82\eta$ , and  $\Upsilon_\gamma = 0.51\eta$ , according to (11), giving the peak values listed in Table 1. The peak electric field of the laser in the rest frame of the electron beam was  $\approx 5 \times 10^{15}$  V/cm.

## 1.5 Related Studies

The first experimental study of nonlinear Thomson scattering [16] reported a weak signal of  $n = 2$  scattering of a laser by keV electrons. Recent studies of second and third-harmonic radiation produced in a laser-plasma interaction [17] have been interpreted as nonlinear Thomson scattering.

Table 1: Peak values of the invariant measures of laser field strength.

	$\lambda$ (nm)	
	1053	527
$\eta$	0.4	0.32
$\Upsilon_e$	0.17	0.27
$\Upsilon_\gamma$	0.08	0.16

Neither those works, nor the present experiment provide decisive evidence for the mass shift (8), although we include the mass shift in our simulations of the experiment.

In the nonrelativistic limit, the energy (7) of the electron in a wave is  $\mathcal{E} \cong mc^2 + P_{\parallel}^2/2m + \eta^2 mc^2/2$ ; the last term is often referred to as the “ponderomotive potential” [11]. The corresponding ponderomotive force is  $\mathbf{F} = -(mc^2/2)\nabla\eta^2 \propto -\nabla E^2$ . Charged particles can scatter off a spatially varying ponderomotive potential. In a quantum view, the charged particle absorbs laser photons and emits photons back into the laser field. A spatially varying field contains a spectrum of photon momenta, so its interaction with the charged particle can result in a change of that particle’s momentum, even though no photon is scattered out of the laser field. In the classical view, the ponderomotive force also can be said to arise from the interference between the laser field and the radiation field of the charge [18].

Ponderomotive scattering of low-energy electrons in an intense laser field has recently been observed [19], and effects of the mass shift on scattered electrons have also been reported [20]. Note that laser trapping of atoms can be considered as a manifestation of the ponderomotive force; an atom with polarizability  $\alpha$  in a nonuniform electric field experiences a force on its induced dipole moment  $\mathbf{p} = \alpha\mathbf{E}$  given by  $\mathbf{F} = \nabla(\mathbf{p} \cdot \mathbf{E}) = \alpha\nabla E^2$ .

If  $\eta$  varies rapidly in time, it is possible for an electron to gain energy from the wave via absorption and emission of laser photons of slightly different energies (without Compton scattering), a process sometimes called vacuum laser acceleration [21, 22]. Vacuum acceleration of electrons has been reported with eV energy gain in a weak laser [23], and MeV gain in a laser with  $\eta = 2$  [24].

The first suggestion that the QED critical field (9) could be subject to experimental study noted that the Earth’s magnetic field appears critical to a cosmic-ray electron of high enough energy [25]. Indeed, the critical magnetic field is

$$B_{\text{crit}} = \frac{m^2 c^3}{e\hbar} = 4.3 \times 10^{13} \text{ gauss}, \quad (15)$$

so a 1-gauss field appears critical to an electron with Lorentz factor  $\gamma \approx 10^{13}$ , *i.e.*, for energy of order  $10^{19}$  eV.

The critical magnetic field appears in the discussion of synchrotron radiation [26], as the field in which an electron would radiate away all of its energy in a single characteristic photon:

$$\gamma mc^2 = \hbar\omega_{\text{crit}} = \gamma^3 \hbar\omega_0 = \gamma^3 \hbar \frac{eB}{\gamma mc}. \quad (16)$$

Hence, this occurs when the field  $B^* = \gamma B$  seen in the electron's rest frame is the critical field (15).

Neutron stars have long been thought to have surface magnetic fields of order  $B_{\text{crit}}$ , and evidence has been reported recently of a “magnetar”, a young pulsar with surface field approximately  $20B_{\text{crit}}$  [27]. A static magnetic field cannot spontaneously create electron positron pairs, since the field invariant  $E^2 - B^2$  is negative. However, electrons and photons of kinetic energies 1 MeV and above readily induce pair creation when in a magnetic field larger than  $B_{\text{crit}}$  [28].

The critical field is also encountered in atomic theory where the field seen by an electron in the lowest orbit of a nucleus of charge  $Z = 1/\alpha = 137$  has the critical value. Highly relativistic electrons channeling through a crystal lattice experience near-critical fields [29] in their rest frame. Critical fields can be produced briefly during heavy ion collisions, although the observed positron production in such conditions does not have a clear interpretation as a critical-field effect [30].

Electrons and positrons at the interaction point of a next-generation linear collider may experience near-critical fields [31, 32, 33, 34, 35, 36]. Here, the essentially static electric field of one bunch appears to have  $\Upsilon \sim 1$  in the rest frame of the other colliding bunch.

## 2 Expected Rates

The nonlinear QED processes (1) and (2) are related by crossing symmetry, and share a common theory [3, 4, 5, 6, 7, 8, 9, 10] based on the Volkov solutions [37] to the Dirac equation for electrons in a classical wave field. The interaction with the high-energy photon is calculated in the Born approximation (perturbatively) using Volkov states of the electron. Although the incident electromagnetic wave (laser beam) is not quantized, the resulting formalism only contains transitions between Volkov states that obey energy and momentum conservation exactly as if the wave had been quantized.

The concept of a cross section is not well defined for initial states involving multiple laser photons. Instead, we consider the differential interaction rates. For example, we write  $dW_n(\omega')/d\omega'$  as the differential probability per unit volume and time that an electron interacts with  $n$  laser photons and emits a single photon with frequency  $\omega'$ . Then, the number of interactions within a given volume element  $dV$ , time interval  $dt$ , and energy bin  $d\omega'$  is

$$N(dV, dt, d\omega') = \frac{dW_n}{d\omega'} \cdot dV \cdot c \, dt \cdot d\omega' \cdot \frac{1}{\hbar c}. \quad (17)$$

Our expectations for the experimental rates of processes (1) and (2) are based on the formalism given in [7, 8].

### 2.1 General Relations

The following list defines the symbols used in our discussion:

$e, m$             electron charge and mass



$c$	speed of light
$p_\mu, p'_\mu$	4-momentum of electron or positron, initial or final state
$\mathcal{E}_-, \mathcal{E}_+$	electron, positron energy
$\gamma_-, \gamma_+$	electron, positron Lorentz factor
$\beta_-, \beta_+$	electron, positron velocity, <i>i.e.</i> $\beta_\pm = \sqrt{1 - 1/\gamma_\pm^2}$
$\rho_e$	number density of beam electrons
$k_\mu, \omega, \rho_\omega$	4-momentum, frequency, and number density of laser photons
$k'_\mu, \omega', \rho_{\omega'}$	4-momentum, frequency, and number density of high-energy photons
$\alpha$	crossing angle between laser pulse and electron or photon beam, <i>e.g.</i> , $\alpha = 0$ for a head-on collision
$n$	number of participating laser photons (order of multiphoton process)
$\eta$	field strength parameter
$\overline{m}$	effective mass of electron

The natural system of units is used, where  $\hbar = c = 1$ . The metric is such that the 4-momentum of an electron obeys  $p^2 = m^2$ .

The dimensionless invariant  $\eta$  introduced in (5) is written as

$$\eta = \frac{eE_{\text{rms}}}{m\omega} = \frac{e}{m} \sqrt{\frac{\rho_\omega}{\omega}}, \quad (18)$$

where  $E_{\text{rms}}$  is the root-mean-square electric field of the laser. The 4-momentum of a charged particle inside an electromagnetic wave is altered due to continuous absorption and emission of photons. For a charged particle with 4-momentum  $p_\mu$  outside the field, the effective 4-momentum (quasimomentum)  $q_\mu$  inside the field is

$$q_\mu = p_\mu + \frac{\eta^2 m^2}{2(k \cdot p)} k_\mu, \quad (19)$$

where  $k_\mu$  is the wave (laser) photon 4-momentum. The effective mass  $\overline{m}$  of the charged particle inside the field then obeys:

$$\overline{m}^2 = q_\mu q^\mu = m^2(1 + \eta^2), \quad (20)$$

as anticipated in (8). The coefficient  $\eta^2 m^2 / 2(k \cdot p)$  in (19) need not be an integer; it represents the time-averaged difference between the large numbers of wave photons that are absorbed and emitted by the electron per cycle of the wave.

## 2.2 Nonlinear Compton Scattering

### 2.2.1 Kinematics

Energy-momentum conservation for the nonlinear Compton scattering process (1) is given in terms of the relevant 4-momenta as

$$q_\mu + nk_\mu = q'_\mu + k'_\mu, \quad (21)$$

where  $n$  is the number of absorbed laser photons. For electrons inside a wave field, the quasimomenta  $q$  rather than the ordinary momenta  $p$  obey the conservation law (21).

The geometry of the experiment is shown in Fig. 1, where the laser beam crosses the electron beam at angle  $\alpha = 17^\circ$ , and the (back)scattered photon angle  $\theta$  is measured from the electron direction. Under our experimental conditions,

$$\gamma = \frac{\mathcal{E}}{m} \gg 1, \quad \theta \sim 1/\gamma \ll \alpha, \quad \text{and} \quad \eta \ll \gamma, \quad (22)$$

where  $\mathcal{E}$  is the energy of a beam electron. The laboratory energy of the scattered photon is obtained from (21) and (22) as

$$\omega' \simeq \frac{2n(k \cdot p)\mathcal{E}}{\bar{m}^2 + 2n(k \cdot p) + \mathcal{E}^2\theta^2}, \quad (23)$$

where  $(k \cdot p) \simeq \mathcal{E}\omega(1 + \cos \alpha)$ . The photon energy  $\omega'$  depends on the laser field strength parameter  $\eta$  through the term  $\bar{m}^2 = m^2(1 + \eta^2)$ .

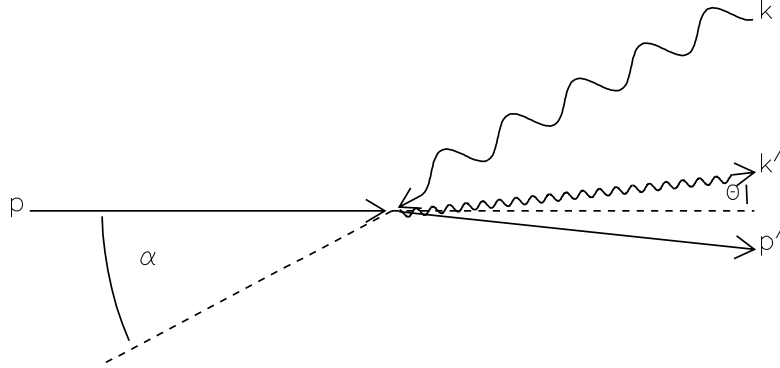


Figure 1: The geometry for the study of nonlinear Compton scattering.

The maximum energy of the scattered photons occurs for  $\theta = 0$ , and the corresponding minimum energy (kinematic edge) for scattered electrons is

$$\mathcal{E}'_{\min}(n, \eta) = \frac{\mathcal{E}}{1 + 2n(k \cdot p)/\bar{m}^2}, \quad (24)$$

which depends on the number of absorbed laser photons, as well as on the laser field strength. The fact that the kinematic edge decreases with increasing  $n$ , as indicated in Table 2, makes it possible to distinguish electrons scattered via nonlinear processes with  $n > 1$  from “ordinary”  $n = 1$  Compton scattering.

Table 2: The minimum energies for electrons scattered by IR and green lasers in the limit that  $\eta \rightarrow 0$ , for different numbers of absorbed photons  $n$ .

$\mathcal{E}'_{\min}(n, 0)$ [GeV]		
$n$	IR	Green
1	25.5	17.6
2	17.6	10.8
3	13.4	7.8
4	10.8	6.1

### 2.2.2 Circular Polarization

The differential reaction rate of photon emission by an unpolarized electron with absorption of  $n$  photons from a circularly polarized laser beam is given by

$$\begin{aligned} \frac{dW_n(\omega')}{d\omega'} &= \frac{\pi r_0^2 m^2 \rho_e \rho_\omega}{\eta^2 \omega \mathcal{E}^2} \left\{ -4J_n^2(z) + \eta^2 \left( 2 + \frac{u^2}{1+u} \right) \cdot \right. \\ &\quad \left. \cdot \left( J_{n-1}^2(z) + J_{n+1}^2(z) - 2J_n^2(z) \right) \right\}, \end{aligned} \quad (25)$$

where

$$z = \frac{2\eta}{u_1} \sqrt{\frac{u(u_n - u)}{1 + \eta^2}}, \quad (26)$$

$$u_1 = \frac{2(k \cdot p)}{\bar{m}^2} \simeq \frac{2\omega \mathcal{E}(1 + \beta \cos \alpha)}{m^2(1 + \eta^2)}, \quad (27)$$

$$u = \frac{(k \cdot k')}{(k \cdot p')} \simeq \frac{\omega'}{\mathcal{E}'}, \quad (28)$$

$$u_n = nu_1, \quad (29)$$

and  $r_0 = e^2/m$  is the classical electron radius.

An expansion of (25) for small values of  $\eta$  shows that the contributions from the  $n^{\text{th}}$  order nonlinear process scale as  $\eta^{2n} \propto (v_\perp/c)^{2n}$ , as expected in the classical limit for  $n^{\text{th}}$ -order multipole radiation. For weak fields ( $\eta \ll 1$ ), the total scattering rate via absorption of one laser photon becomes

$$W_1 = \frac{\pi r_0^2 m^2 \rho_e \rho_\omega}{\omega \mathcal{E}} \left\{ \left( 1 - \frac{4}{u_1} - \frac{8}{u_1^2} \right) \ln(1 + u_1) + \right.$$

$$\left. + \frac{1}{2} + \frac{8}{u_1} - \frac{1}{2(1+u_1)^2} \right\}. \quad (30)$$

This rate can be identified with the ordinary Compton scattering cross section  $\sigma_C$  [38] by noting that  $W_1 = \rho_e \rho_\omega (1 + \beta \cos \alpha) \sigma_C$ , so that  $\sigma_C = 2\omega \mathcal{E} W_1 / m^2 \rho_e \rho_\omega u_1$ .

The kinematic edges of the spectra of scattered electrons and photons are influenced by the mass-shift effect, (20). As  $\eta$  increases, the electron is effectively more massive, and recoils less during the scattering. Therefore, the minimum energy of the scattered electron (the kinematic edge) is higher, as illustrated in Fig. 2.

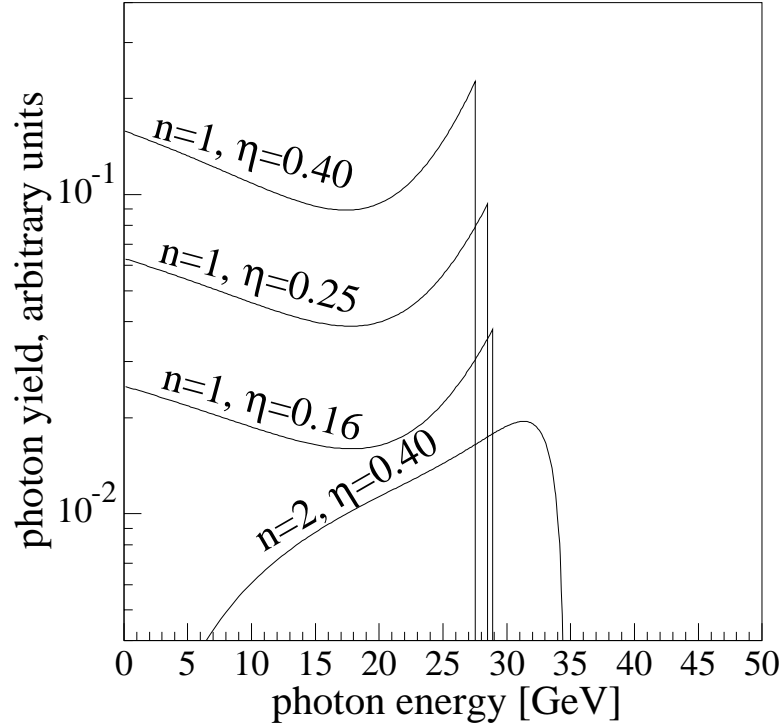


Figure 2: The calculated rate for nonlinear Compton scattering of 46.6 GeV electrons and 527 nm photons for several values of the field strength parameter  $\eta$ , as a function of the energy of the scattered photon.

To use (25), which was derived for a plane wave of frequency  $\omega$ , for comparison to experiments that use a focused laser pulse, we make the adiabatic approximation that (25) holds for the instantaneous value of  $\eta$  at each spacetime point. Details of the numerical calculations of the expected event rates are presented in appendix A.

Figures 3 and 4 show results from a simulation of nonlinear Compton scattering for parameters similar to those of the present experiment: a circularly polarized infrared laser pulse of 1 J energy,  $50 \mu\text{m}^2$  focal-spot area, and 1.88 ps length, corresponding to  $\eta = 0.6$  at the focus;  $5 \times 10^9$  incident electrons are assumed in a Gaussian pulse with  $\sigma_x = \sigma_y = 60 \mu\text{m}$  and  $\sigma_z = 870 \mu\text{m}$ . Photons scattered to energies higher than the kinematic edge of order  $n$  can

only be due to nonlinear Compton scattering, (1), of order higher than  $n$ . However, electrons can be scattered to energies lower than the kinematic edge of order  $n$  by an additional process that we call plural Compton scattering, as discussed in sec. 2.3 below. The solid curve in Fig. 4 is the overall spectrum of scattered electrons, including all orders of  $n$ , as well as the plural scattering effect. The dashed curve shows the contribution of single photon scattering, including plural  $n = 1$  scattering. The curves labeled  $n = 2, 3$ , and 4 show the contribution of nonlinear and plural scatters of the respective order.

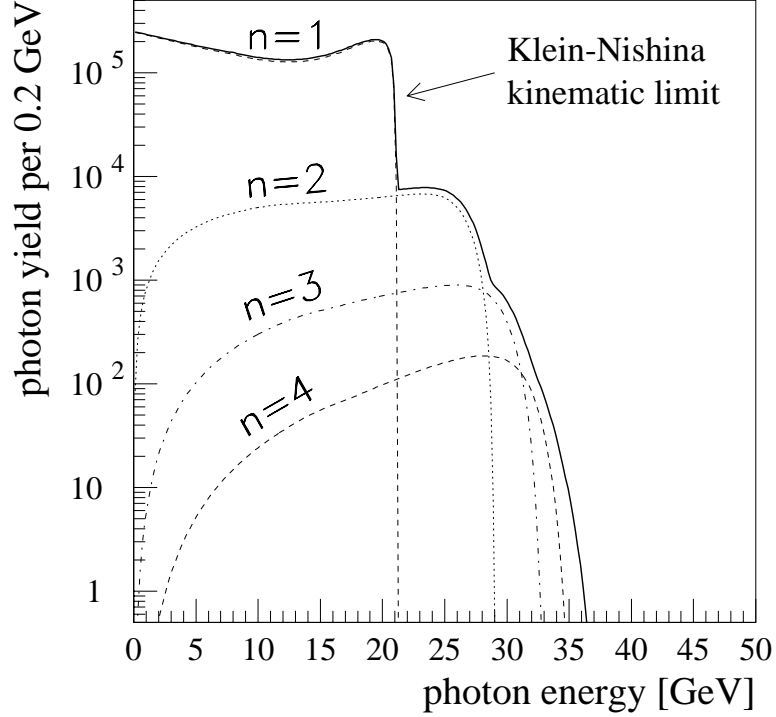


Figure 3: The calculated rate of scattered photons for nonlinear Compton scattering for the infrared laser and electron beam parameters given in the text. The dashed curves show the rates for  $n = 1, 2, 3$ , and 4 nonlinear Compton scattering. The solid curve is the sum of all orders.

As the order  $n$  increases, the scattered photon (electron) can reach higher (lower) energy and the yield decreases (for  $\eta \lesssim 1$ ), as can be seen in Fig. 4. The  $n = 1$  kinematic edge is not as abrupt as for weak-field Compton scattering, because a significant fraction of the scatters occur where  $\eta$  is large, so the larger effective mass  $\overline{m}$  of the electron results in a smaller loss of energy. The kinematic edges between different orders become less distinguishable as  $n$  increases.

The kinematic edges will also be smeared by the effect of detector resolution. Because the spectrum is steeply falling, the observed data on, say, electron energies will appear to extend to lower energies than nominal, and the inflection where the rate of order  $n$  meets that of order  $n + 1$  can be shifted by 0.5-1 GeV in our experiment.

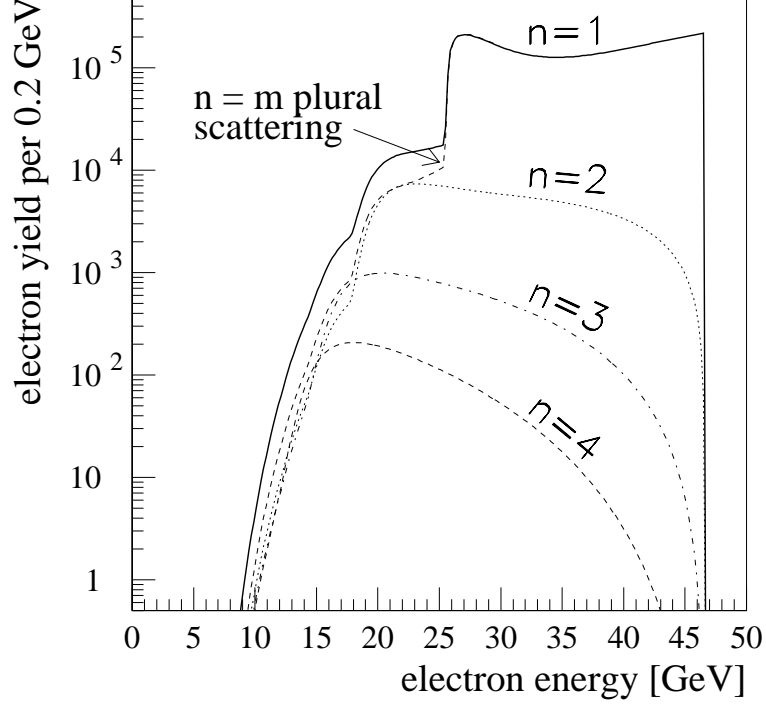


Figure 4: The calculated rate of scattered electrons for linear, nonlinear and plural Compton scattering for the infrared laser and electron beam parameters given in the text. The solid line is the sum of all possible processes. The rates for  $n = 2, 3$ , and  $4$  nonlinear Compton scattering are shown separately as well.

### 2.2.3 Linear Polarization

The differential interaction rate for  $n$  linearly polarized laser photons and an unpolarized electron is:

$$\frac{dW_n(\omega')}{d\omega'} = \frac{8r_0^2 m^2 \rho_e \rho_\omega}{\eta^2 \omega \mathcal{E}^2} \int_0^{\pi/2} d\phi \left\{ -A_0^2 + \right. \\ \left. + \eta^2 \left( 2 + \frac{u^2}{1+u} \right) (A_1^2 - A_0 A_2) \right\}, \quad (31)$$

where the real functions  $A_i$ ,  $i = 0, 1, 2$ , are defined by

$$A_i(n, a, b) \equiv \frac{1}{\pi} \int_0^\pi d\nu \cos^i \nu \cdot \\ \cdot \cos[(a + 2b \cos \nu) \sin \nu - n\nu], \quad (32)$$

and the parameters  $a$  and  $b$  are given by

$$a \equiv \sqrt{2} m \eta \left( \frac{(\varepsilon \cdot p)}{(k \cdot p)} - \frac{(\varepsilon \cdot p')}{(k \cdot p')} \right), \quad (33)$$

$$b \equiv \frac{m^2 \eta^2}{4} \left( \frac{1}{(k \cdot p)} - \frac{1}{(k \cdot p')} \right), \quad (34)$$

where  $\varepsilon_\mu = (\varepsilon_0, \varepsilon)$  is the polarization 4-vector of the laser photons, which obeys  $\varepsilon^2 = -1$ .

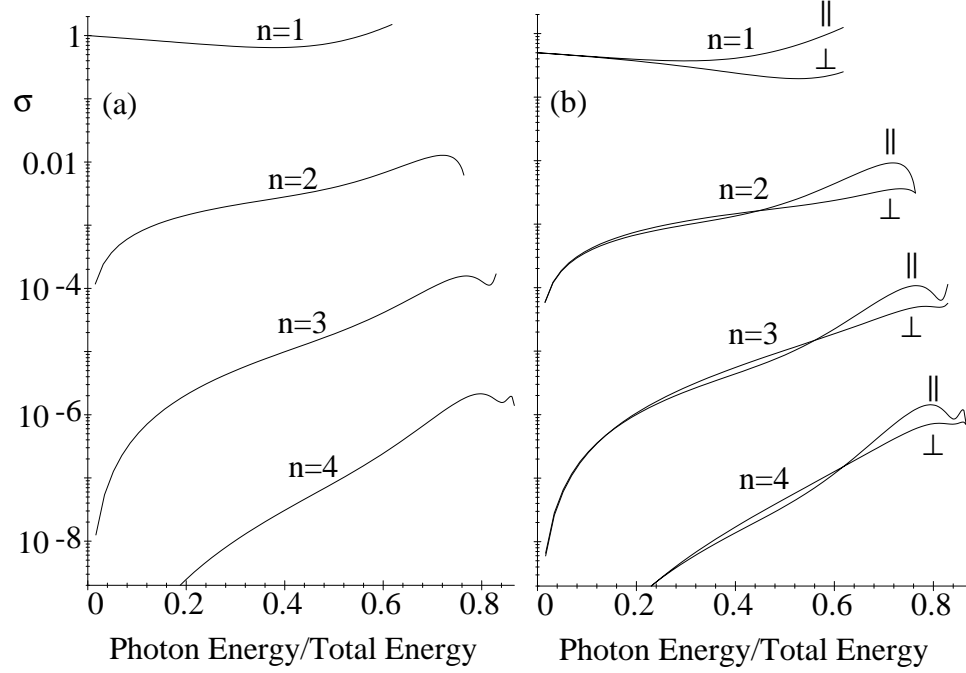


Figure 5: Calculated spectra,  $\sigma \equiv (\omega \mathcal{E} / \pi r_0^2 m^2) (dW_n / d\omega')$ , of backscattered photons produced in the interaction of a 46.6 GeV electron with  $n = 1, 2, 3$ , and  $4$  photons from a linearly polarized 527 nm plane wave with  $\eta = 0.1$ , as a function of the ratio  $\omega'/\mathcal{E}$  of the energy of the backscattered photon to that of the beam electron. (a) Spectra summed over the polarization of the backscattered photon. (b) Spectra for polarization of the backscattered photon parallel and perpendicular to that of the incident wave.

The polarization of the emitted photon becomes important when considering the pair production reaction (2). The differential interaction rates for the interaction of linearly polarized laser photons with unpolarized electrons, resulting in the emission of a linearly polarized high-energy photon, are [39]

$$\begin{aligned} \frac{dW_n^{\parallel}(\omega')}{d\omega'} &= \frac{8r_0^2 m^2 \rho_e \rho_\omega}{\eta^2 \omega \mathcal{E}^2} \int_0^{\pi/2} d\phi \left\{ 2\eta^2 \xi A_0^2 + \right. \\ &\quad \left. + \eta^2 \left( 2 + \frac{u^2}{2(1+u)} \right) (A_1^2 - A_0 A_2) \right\}, \end{aligned} \quad (35)$$

$$\frac{dW_n^{\perp}(\omega')}{d\omega'} = \frac{8r_0^2 m^2 \rho_e \rho_\omega}{\eta^2 \omega \mathcal{E}^2} \int_0^{\pi/2} d\phi \left\{ -(1 + 2\eta^2 \xi) A_0^2 + \right.$$

$$+\eta^2 \frac{u^2}{2(1+u)} (A_1^2 - A_0 A_2) \Big\}, \quad (36)$$

where

$$\xi = \left[ \frac{1}{2} + \frac{n}{4b} + \left( \frac{a}{8b} \right)^2 \right], \quad (37)$$

and  $\parallel, \perp$  indicate high-energy photons produced with polarizations parallel or perpendicular to that of the interacting laser photons, respectively.

Figure 5 illustrates the rates (31) and (35-36) for parameters relevant to the present experiment. Note that when the backscattered photon has energy near its maximum, its polarization is much more probable to be parallel than perpendicular to that of the laser [40].

### 2.3 Plural Compton Scattering

Since the final state of nonlinear Compton scattering contains only one emitted photon and one electron (see Fig. 6), in principle it suffices to measure either one of the two. Because high-energy electrons can be separated according to momentum using a magnetic field, it is most convenient to measure the electron spectrum. However, at the high fields (photon densities) of the present experiment, plural Compton scattering in the laser focus gives an additional contribution to the electron spectrum. By plural scattering, we refer to the process,

$$e + n\omega \rightarrow e' + m\omega', \quad m > 1, \quad n \geq m, \quad (38)$$

where an electron undergoes  $m > 1$  consecutive scatters within the laser focus, accompanied by the emission of  $m$  photons (of  $m$  different energies), and by the absorption of  $n \geq m$  laser photons, as sketched in Fig. 7. This process is distinct from  $n^{th}$ -order nonlinear Compton scattering, (1), since two or more photons are emitted in plural scattering. Both of these processes are distinct from the case where one photon is absorbed and two emitted; this latter process is a radiative correction to ordinary Compton scattering, and has been called double Compton scattering.

That plural scattering is probable can be seen as follows. The photon number density at the laser focus for  $I = 10^{18}$  W/cm<sup>2</sup> in the infrared is  $\rho_\omega = I/(\hbar\omega c) = 2 \times 10^{26}$ /cm<sup>3</sup>. The total Compton cross section is  $\sigma_C = 1.9 \times 10^{-25}$  cm<sup>2</sup>, and the electron pathlength through the laser focus is of order  $\ell \simeq 50$   $\mu$ m. Hence, the interaction probability is  $\rho_\omega \ell \sigma_C \approx 0.2$ , so 20% of the interacting electrons will undergo two scatters, *etc.*

The minimum energy (lower kinematic edge) of the scattered electron is the same for all processes having the same total number of photons absorbed from the field, regardless of the total number of photons emitted. Therefore, the minimum number of laser photons involved in the interaction with a particular electron can be inferred from measurement of the final electron energy.

However, the determination that scattering occurred by multiple photon absorption in a single interaction, *i.e.*, by process (1), rather than only by  $n = m$  plural scattering, requires a comparison of observed and calculated recoil electron spectra (if the photons



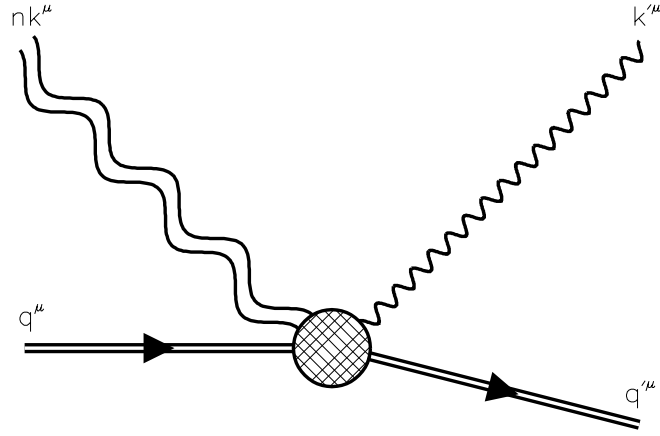


Figure 6: Representation of nonlinear Compton scattering, (1). An electron with quasimomentum  $q$  in a strong field (indicated by a double line) absorbs  $n$  photons (indicated by double sinusoids), emits a high-energy photon  $k'$ , and recoils with momentum  $q'$ .

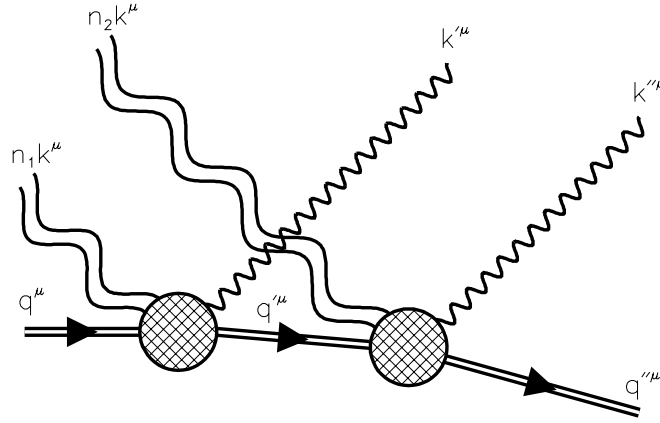


Figure 7: Plural Compton scattering, (38), of an electron in the laser field with  $n = n_1 + n_2$  and  $m = 2$ . The electron with initial momentum  $q$  scatters from  $n_1$  laser photons, emitting a photon with momentum  $k'$ , and recoiling with momentum  $q'$ ; then the electron scatters again from the laser field, absorbing  $n_2$  laser photons, emitting another photon  $k''$ , and recoiling with momentum  $q''$ .

are not observed). For example, Fig. 4 includes a calculation of  $n = m$  plural scattering and indicates that this process is expected to be much smaller than nonlinear Compton scattering, (1), only for scattered electron energies below 15 GeV.

The spectrum of high-energy photons beyond the  $n = 1$  kinematic edge is free from  $n = m$  plural scattering, since only multiphoton absorption in a single interaction can yield photon energies beyond that kinematic edge. On the other hand, it was difficult to measure the spectrum of the forward photons because of the high flux (up to  $10^7$  scatters in 2 ps), and the small angular spread (of order of  $1/\gamma$ ). By placing a thin foil in the beamline at  $0^\circ$  from the interaction region, it was possible to convert a fraction of the forward photons, and to measure the converted electrons (or positrons) in a magnetic spectrometer, as discussed in sec. 3.4.

Just as the scattered electron can undergo further scattering in the laser focus, a high-energy backscattered photon can give rise to pair production via reaction (2), as discussed in the following section.

## 2.4 Multiphoton Pair Production

The differential rate for  $e^+e^-$  pair production in the interaction of a circularly polarized laser beam of frequency  $\omega$  with an unpolarized high-energy photon of frequency  $\omega'$ , process (2), is

$$\begin{aligned} \frac{dW_n(\mathcal{E}_\pm)}{d\mathcal{E}_\pm} &= \frac{2\pi r_0^2 m^2 \rho_\omega \rho_{\omega'}}{\eta^2 \omega \omega'^2} \left\{ 2J_n^2(z) + \eta^2(2u - 1) \cdot \right. \\ &\quad \left. \cdot (J_{n-1}^2(z) + J_{n+1}^2(z) - 2J_n^2(z)) \right\}, \end{aligned} \quad (39)$$

where

$$z = \frac{2\eta}{u_1} \sqrt{\frac{u(u_n - u)}{1 + \eta^2}}, \quad (40)$$

$$u_1 = \frac{(k \cdot k')}{2\overline{m}^2} \simeq \frac{\omega\omega'(1 + \beta \cos \alpha)}{2m^2(1 + \eta^2)}, \quad (41)$$

$$u = \frac{(k \cdot k')^2}{4(k \cdot p)(k \cdot p')} \simeq \frac{\omega'^2}{4\mathcal{E}_\pm(\omega' - \mathcal{E}_\pm)}, \quad (42)$$

$$u_n = nu_1. \quad (43)$$

The electron (or positron) energy  $\mathcal{E}_\pm$  is a double-valued function of the invariant  $u$ . The index  $n$  must be at least the minimum number  $n_0$  of photons needed to produce one pair:

$$n_0 = \frac{(2\overline{m})^2}{2(k \cdot k')} = \frac{2m^2(1 + \eta^2)}{\omega\omega'(1 + \beta \cos \alpha)}, \quad (44)$$

according to energy conservation. Note that the effective mass  $\overline{m}$  enters this threshold condition. Further, even though the ratio  $eE/m\omega c$ , and hence the transverse momentum, can vary over the classical trajectory of an electron or positron, only the rms quantity  $\eta$  enters in the quantum condition (44).

For the weak-field case, pair creation by light was first calculated by Breit and Wheeler [41], whose result for a head-on collision can be obtained from (39) on setting  $n = 1$ , letting  $\eta \rightarrow 0$ , and integrating over  $\mathcal{E}_\pm$ :

$$\begin{aligned} W_1 &= 2\rho_\omega\rho'_\omega\sigma_{\text{BW}} \\ &= 2\pi r_0^2 \frac{m^2}{\omega\omega'} \rho_\omega\rho_{\omega'} \left\{ \left( 2 + \frac{2m^2}{\omega\omega'} - \frac{m^4}{\omega^2\omega'^2} \right) \right. \\ &\quad \cdot \left. \tanh^{-1} \sqrt{1 - \frac{m^2}{\omega\omega'}} - \sqrt{1 - \frac{m^2}{\omega\omega'}} \left( 1 + \frac{m^2}{\omega\omega'} \right) \right\}. \end{aligned} \quad (45)$$

For  $\eta \ll 1$ , the higher-order rate  $W_n$  varies as  $\eta^{2n}$ .

To observe positron production, we used linearly polarized green laser light ( $\lambda = 527$  nm), so that for 46.6 GeV incident electrons the endpoint of the  $n = 1$  photon spectrum from reaction (1) is at  $\mathcal{E}_\gamma = 29.1$  GeV. Thus,  $n_0 = 5$  according to (44); any positrons produced are the result of a highly nonlinear interaction. Photons arising from  $n = 2$  Compton scattering can have energies greater than 29.1 GeV, and can produce pairs with only  $n_0 = 4$  laser photons in reaction (2).

In all cases, pair creation is most likely from photons backscattered with maximal energy, for which the Compton scattering process with unpolarized electrons results in the high-energy photon having the same polarization as the laser photons, as shown in Fig. 5. The differential rates for pair production by linearly polarized laser photons interacting with a linearly polarized high-energy photon are

$$\begin{aligned} \frac{dW_n^\parallel(\mathcal{E}_\pm)}{d\mathcal{E}_\pm} &= \frac{16\pi^2 r_0^2 m^2 \rho_\omega \rho_{\omega'}}{\eta^2 \omega \omega'^2} \int_0^{\pi/2} d\phi \left\{ -2\eta^2 \xi A_0^2 + \right. \\ &\quad \left. + 2\eta^2 (u - 1) (A_1^2 - A_0 A_2) \right\}, \end{aligned} \quad (46)$$

$$\begin{aligned} \frac{dW_n^\perp(\mathcal{E}_\pm)}{d\mathcal{E}_\pm} &= \frac{16\pi^2 r_0^2 m^2 \rho_\omega \rho_{\omega'}}{\eta^2 \omega \omega'^2} \int_0^{\pi/2} d\phi \left\{ (1 + 2\eta^2 \xi) A_0^2 + \right. \\ &\quad \left. + 2\eta^2 u (A_1^2 - A_0 A_2) \right\}, \end{aligned} \quad (47)$$

where again  $n \geq n_0$ ,  $A_i$ ,  $i = 0, 1, 2$ ,  $a$  and  $b$  are defined by (32-34),  $\xi$  is defined in eq. (37), and  $\parallel$  and  $\perp$  indicate the polarization of the high-energy photon as parallel and perpendicular to that of the laser beam, respectively.

Figure 8 illustrates a calculation based on (46-47) for a 30 GeV photon and laser parameters similar to those in the present experiment. The pair production rate is higher for the case that the laser and the high-energy photons have perpendicular polarization; however, parallel polarization is simpler to arrange in the laboratory. The conditions of the experiment also imply a yield of about  $10^6$  backscattered photons per laser pulse between 27 and 30 GeV, and hence the results shown in Fig. 8 indicate a production rate of about  $10^{-2}$  positrons per laser pulse; see also, Fig. 10. Therefore, background from beam scraping upstream of the interaction region (as well as from trident pair production off residual gas molecules in the beam vacuum) had to be strictly controlled.

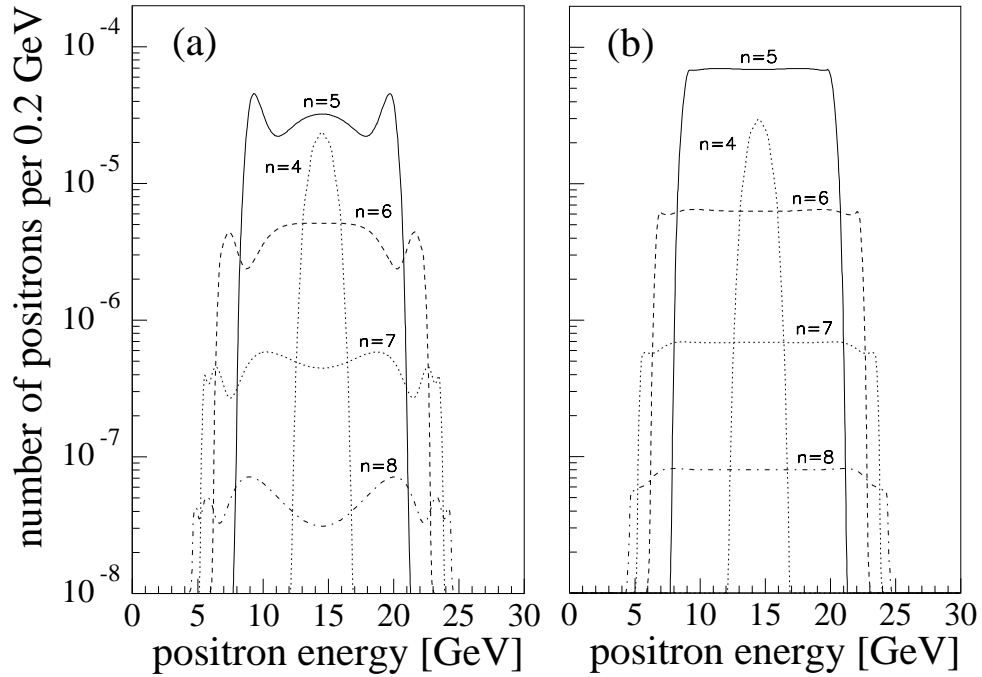


Figure 8: Calculated energy spectra of positrons produced in the interaction of a 30 GeV photon with a 527 nm laser beam. (a) Parallel polarization. (b) Perpendicular polarization. The curves are labelled by the number of laser photons involved.

The rates (39) and (46-47) have simpler forms in the limit that  $\eta \gg 1$ , but  $\Upsilon_\gamma \lesssim 1$  [4, 7]:

$$W^\perp = 2W^\parallel \propto e^{-8/3\sqrt{2}\Upsilon_\gamma}. \quad (48)$$

These forms are very similar to that of spontaneous pair creation in a strong static electric field [12, 14, 15]:

$$W = \frac{\alpha E^2}{\pi^2} e^{-\pi/\Upsilon}, \quad (49)$$

where  $\Upsilon = E/E_{\text{crit}}$  is the ratio of the electric field strength to the QED critical field strength (9). That is, for  $\eta \gg 1$  in a strong laser beam probed by an external photon, large numbers of laser photons participate in the pair creation process in a manner somewhat equivalent to pair creation in a static field of comparable strength. In this view, pair creation is the realization of a virtual electron-positron pair in a strong electric field (breakdown of the vacuum). In the case of a strong wave field, the external photon acts as a kind of catalyst for pair creation, which is otherwise forbidden in a field where the invariant  $E^2 - B^2$  vanishes.

The close relation between pair creation by a laser beam to that in a static electric field is further illustrated by consideration of the intermediate case of a standing electric wave of frequency  $\omega$  and peak field strength  $E$  (with no magnetic field) [42]. Here, the probability

of pair creation per unit volume–unit time is given by

$$P = \frac{\alpha E^2}{2\pi} \frac{e^{-\pi g(\eta)/\Upsilon}}{g(\eta) - \frac{1}{2}\eta g'(\eta)}, \quad (50)$$

where  $g(\eta)$  is the monotonic function defined by

$$g(\eta) = \frac{4}{\pi} \int_0^1 dx \left( \frac{1-x^2}{1+x^2/\eta^2} \right)^{1/2}, \quad (51)$$

with  $\eta = eE/m\omega$ , and  $\Upsilon = E/E_{\text{crit}}$ . At large  $\eta$ , the function  $g$  approaches unity, as shown in Fig. 9.

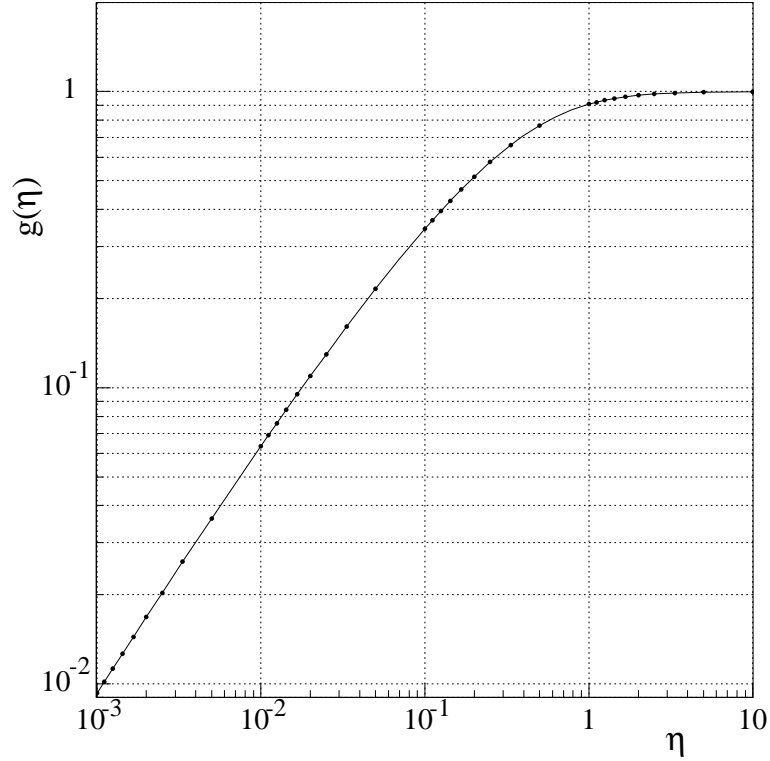


Figure 9: The function  $g(\eta)$  defined by eq. (51).

For  $\eta \gtrsim 1$ , the rate (50) becomes identical (within a factor of  $\pi/2$ ) to that in a static electric field, (49), while for  $\eta \ll 1$  the rate obeys

$$W = \frac{\alpha E^2}{8} \left( \frac{\eta}{\sqrt{2}} \right)^{2n}, \quad (52)$$

where  $n = 2m/\omega$  is the minimum number of “photons” of frequency  $\omega$  that must be absorbed from the standing wave field to create a pair. Equation (52) is also a good approximation to the total rate of multiphoton Breit-Wheeler pair creation, (2), for small  $\eta$ .

## 2.5 The Multiphoton Trident Process

In a region where both high-energy electrons and photons can interact with the laser beam, there is an additional process by which an  $e^+e^-$  pair can be produced:

$$e + n\omega \rightarrow e'e^+e^-, \quad (53)$$

which we call the multiphoton trident process. The minimum number  $n_0$  of laser photons required to produce a pair is

$$n_0 = \frac{(3^2 - 1)\overline{m}^2}{2(k \cdot p)} = \frac{4m^2(1 + \eta^2)}{\omega\mathcal{E}(1 + \beta \cos \alpha)}, \quad (54)$$

since the final state of (53) contains 3 electrons in the wave. For a 46.6 GeV electron and 527 nm laser photons,  $n_0 = 5$  at  $\eta = 0$ .

There exists no formal theory of the trident process in strong fields, so we have estimated its rate assuming it to be equivalent to a two-step process during which the beam electron emits a virtual photon ( $\omega'$ ) according to the Weizsäcker-Williams approximation, and then the virtual photon combines with  $n$  laser photons to form a pair according to the multiphoton Breit-Wheeler pair production process [43, 44]. That is, we consider reaction (53) as equivalent to

$$e \rightarrow e' + (\omega'), \quad (55)$$

$$(\omega') + n\omega \rightarrow e^+e^-. \quad (56)$$

The differential reaction rate for the trident process, assuming the two-step model (55-56), is [43]

$$\begin{aligned} \frac{dW^{(\text{trident})}(\mathcal{E}_\pm)}{d\mathcal{E}_\pm} &= \frac{2\alpha_{\text{EM}}}{\pi} \sum_{n \geq n_0} \int_{s'_{\min}}^{s'_{\max}} \frac{ds'}{s'} \ln \left( \frac{s'_{\max}}{s'} \right) \cdot \\ &\quad \cdot \frac{dW_n^{(\text{MPBW})}(\mathcal{E}_\pm)}{d\mathcal{E}_\pm}, \end{aligned} \quad (57)$$

where MPBW denotes the multiphoton Breit-Wheeler pair production process,  $\alpha_{\text{EM}}$  is the fine-structure constant,  $s = (q + nk)^2 = \overline{m}^2 + 2n(k \cdot p)$  is the square of the center-of-mass energy of process (53), and  $s'$  corresponds to the subprocess (56), *i.e.*,  $s' = (k + nk')^2 = 2n(k \cdot k')$ . The remaining factors in (57) represent the spectrum of the virtual photons. The limits of integration follow from energy conservation:

$$s'_{\min} = (2\overline{m})^2 = 4m^2(1 + \eta^2), \quad (58)$$

$$s'_{\max} = (\sqrt{s} - \overline{m})^2. \quad (59)$$

A calculation comparing the rate of positron production from the trident process according to (57) and the rate from the two step process (1) followed by (2) is shown in Fig. 10. Since a minimum of 5 laser photons are required, the rates vary roughly as the  $5^{\text{th}}$  power of the laser intensity, and hence as the  $10^{\text{th}}$  power of the laser field strength. We estimate that the rate for trident pair production is less than 1% that from the multiphoton Breit-Wheeler process.

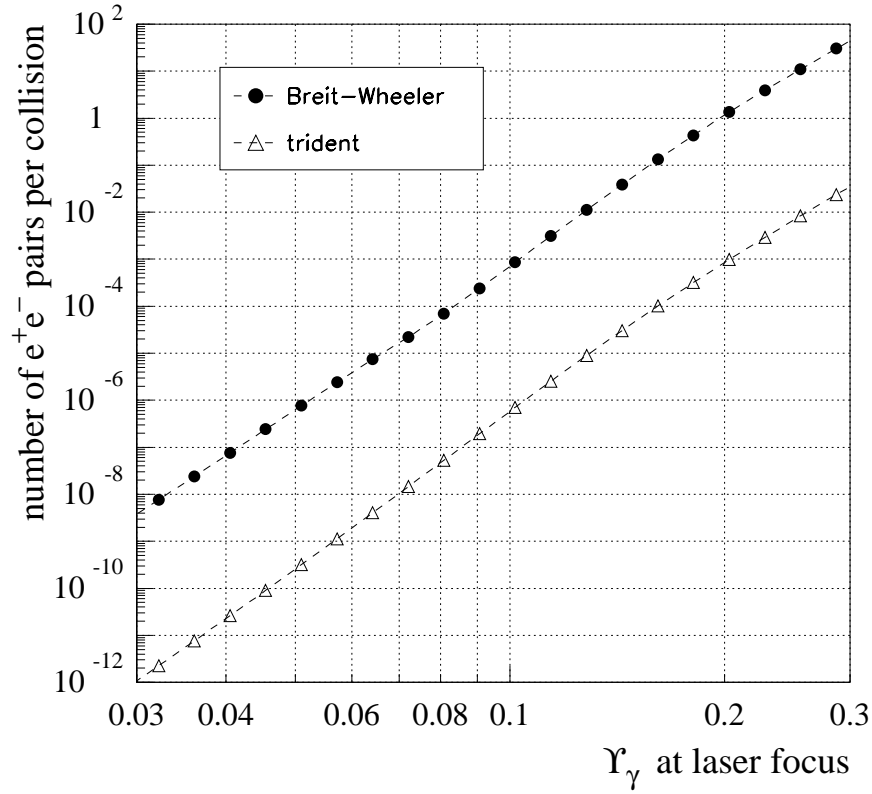


Figure 10: The calculated rates for pair production from the multiphoton Breit-Wheeler process (2) and from trident production (53) as a function of  $\Upsilon_\gamma$  at the laser focus. In the present experiment, the maximum value of  $\Upsilon_\gamma$  was about 0.16.

### 3 Experimental Arrangement

The experiment was carried out in the Final Focus Test Beam (FFTB) [45]. The electrons collided with the tightly focused terawatt laser [46, 47, 48, 49] at an interaction point (IP1) immediately upstream of the magnets which directed the primary electron beam to the dump, as shown in Fig. 11. These same magnets dispersed the scattered electrons and positrons according to their momentum into two Si-W calorimeters, called ECAL and PCAL, respectively. Scattered electrons with  $\mathcal{E}_e < 28$  GeV and positrons with  $\mathcal{E}_e < 20$  GeV were deflected out of the vacuum pipe and could reach the detector. The high-energy photons created in the collision proceeded in the forward direction to suitable monitors, but could also be converted and detected in the pair spectrometer.

#### 3.1 Laser System

The laser was a 0.5-Hz-repetition-rate, tabletop terawatt ( $T^3$ ) laser, that operated at 1053 nm wavelength (IR), or at 527 nm (green) after efficient ( $\sim 45\%$ ) frequency doubling. The laser was based on the technique of chirped pulse amplification [50], and it consisted of a mode-

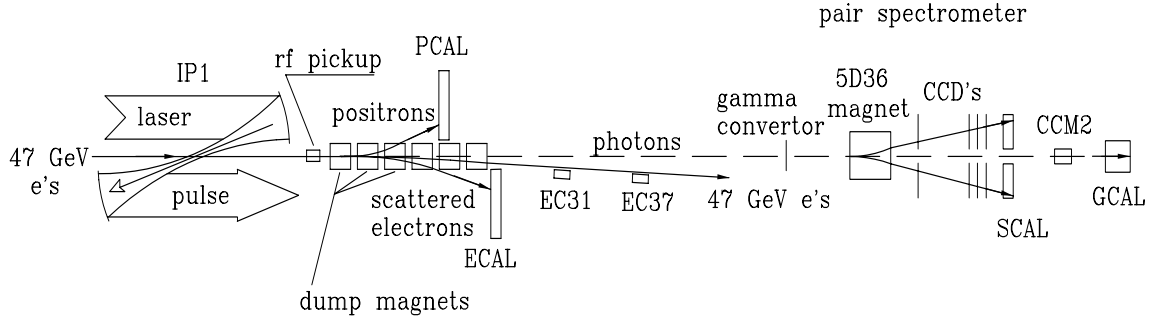


Figure 11: Schematic of the experimental setup: The laser pulses crossed through the electron beam at the interaction point, IP1. The scattered electrons were deflected by the dump magnets into the electron calorimeter (ECAL). Positrons were deflected into the positron calorimeter (PCAL). The scattered photons were detected in a Čerenkov counter (not shown), or converted to  $e^+e^-$  pairs which could be detected by the pair spectrometer.

locked Nd:YLF oscillator, Nd:glass regenerative amplifier, a two-pass Nd:glass rod amplifier and a flashlamp-pumped Nd:glass slab amplifier, as shown schematically in Fig. 12.

The laser system delivered up to 2.4 J in the IR at the interaction point, but typically it was operated only up to 800 mJ of IR and 500 mJ of green. The laser has been focused to better than 2 times the diffraction-limited area. The shortest pulsewidth achieved during the running period was 1.5 ps FWHM ( $\sigma_{\text{laser}} \approx 0.6$  ps). Intensities above  $10^{18}$  W/cm<sup>2</sup> at the laser focus have been produced.

The relatively high repetition rate of 0.5 Hz was achieved via the use of a slab amplifier [51], which had highly efficient cooling as compared to large-diameter rod amplifiers. Small-signal gain of 600 was achieved with three passes at 6 kJ of flashlamp energy. The elliptical beam size in the slab was 1 cm  $\times$  4 cm. After recircularization, spatial filtering, and further expansion, the beam was directed to the compression stage, which consisted of two 1760-lines/mm, gold-coated, 160 mm  $\times$  220 mm holographic gratings used in the near-Littrow, double-pass configuration with a separation distance of 164 cm [52].

After compression, the frequency of the laser pulse could be doubled by using 4-mm- or 8-mm-thick Type II KDP crystals [53], the thicker crystal being used at lower intensities ( $I < 30$  GW/cm<sup>2</sup>). Efficiencies of 45% were obtained, compared to the theoretically predicted value of 50%. After frequency doubling, the laser pulse was circularly polarized using a liquid crystal polarizer.

The laser beam was transported in vacuum to the interaction point and focused onto the electron bunch by an off-axis paraboloid mirror (OAP) [54], and then recollimated by a second OAP for return to the laser room. These optics were located in the IP vacuum box, which is shown in Fig. 13. Since the laser path was fixed with respect to the IP vacuum box, alignment with respect to the electron beam was accomplished by moving the entire box. Three motions were possible: transverse horizontal ( $x$ ), vertical ( $y$ ), and rotation about the beam ( $z$ ) axis, via motors interfaced into the SLAC Control Program [55, 56].

The laser pulse was returned to the laser room in order to measure its energy, pulsewidth



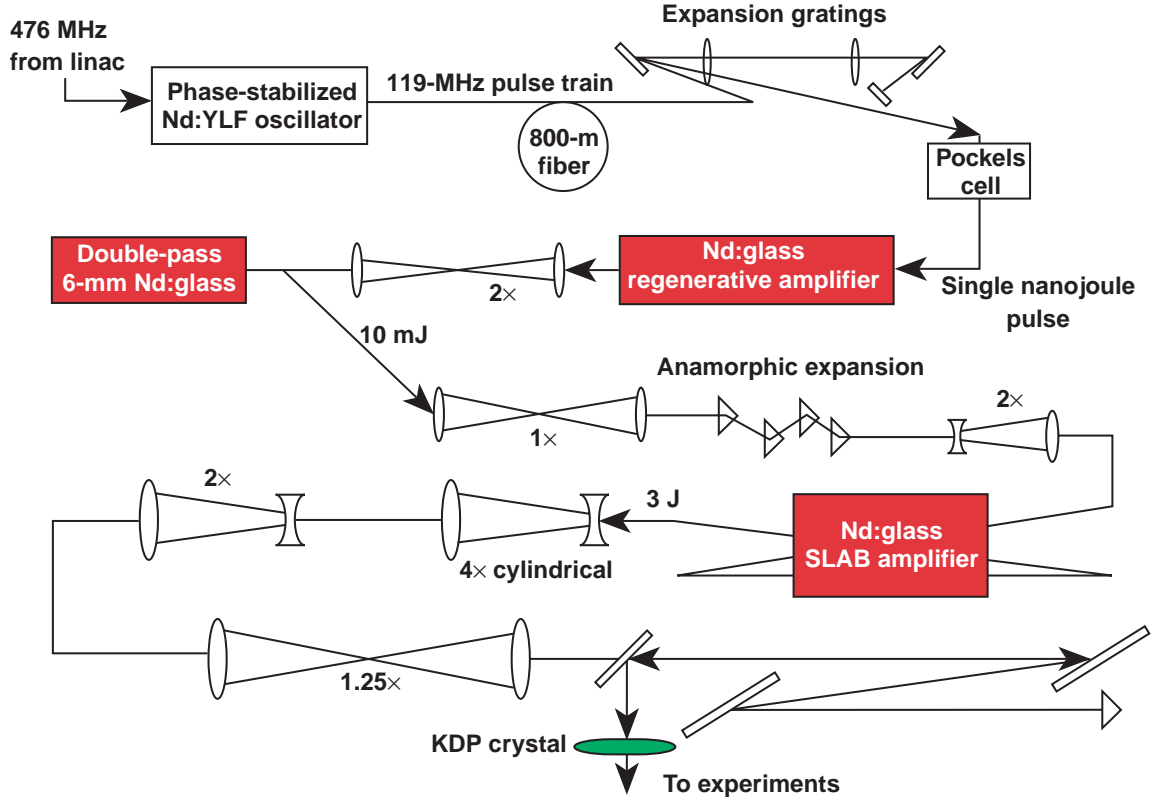


Figure 12: Schematic of the laser system.

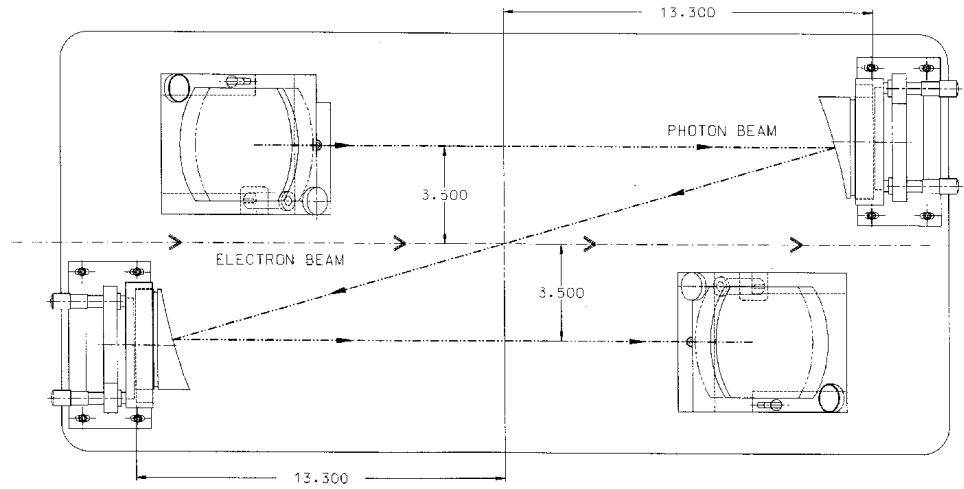


Figure 13: The optical elements in the interaction point enclosure (IP vacuum box). Dimensions are in inches.

and focal area, and to allow accurate alignment of the transport and focusing optics. Good wavefront quality of the beam returning to the laser room was an indication that the alignment of the OAP pair was correct, and that the pointing of the beam incident on the first OAP coincided with the OAP axis. To aid in alignment, we used a copropagating, continuous-wave, frequency-stabilized He-Ne beam with a large diameter ( $\simeq 7.5$  cm) and co-injected it into the transport; after its return from the IP, it interfered with the original beam in a Mach-Zehnder interferometer configuration. The laser transport line was  $\approx 12$  m long and was under vacuum; entrance and exit windows were 1-inch-thick BK7 glass, which contributed some wavefront distortion [57].

The laser energy was measured by leakage monitors behind one of the mirrors before the transport line and behind a flat in the diagnostic line after the transport. The IR pulsed width was measured with a single-shot autocorrelator in the diagnostic line, while the width of the green pulses occasionally was measured with a Hamamatsu streak camera, and with a single-shot autocorrelator. The focal spot at the interaction point was measured indirectly by the equivalent-target-plane technique after the return of the laser beam into the laser room. For this purpose the beam was refocused after the transport with a 4 m focal length lens, reflected off four flats which attenuated the beam energy by  $10^6$ , and further attenuated by neutral-density filters. The focus was imaged with a  $5\times$  microscope objective onto a CCD camera.

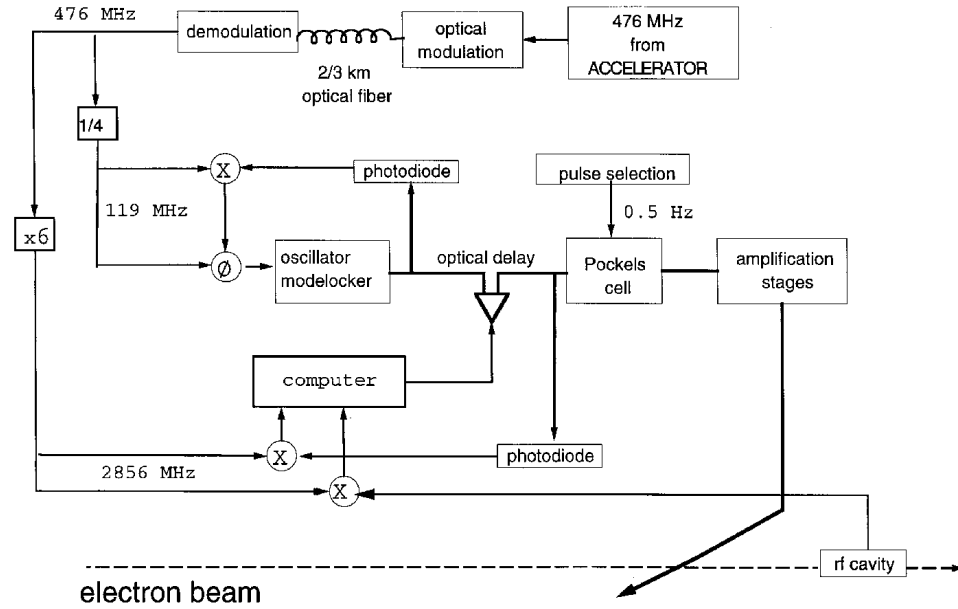


Figure 14: Diagram of the timing system for the synchronization of the laser pulses with the electron beam.

The diffraction limit for the radius  $w$  of the focal spot is given by

$$w_{\text{dif}} = \frac{\sqrt{2}f_{\#}}{\pi}\lambda, \quad (60)$$

and we define the diffraction-limited focal area as

$$A_{\text{dif}} = \pi w_{\text{dif}}^2. \quad (61)$$

We used  $f_{\#} \simeq 6$ , so that  $A_{\text{dif}} = 25 \mu\text{m}^2$  for IR and  $6 \mu\text{m}^2$  for the green. The actual spot sizes attained were larger, approximately twice diffraction-limited for the infrared laser, and approximately five times diffraction-limited for the green laser.

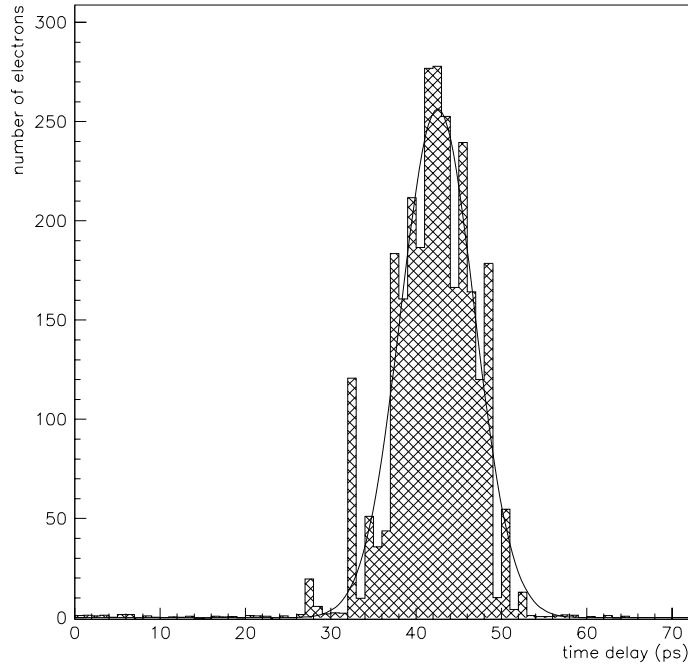


Figure 15: A “timing curve” showing the number of electrons scattered into the top row of the electron calorimeter as a function of delay of the optical pulse. The standard deviation is  $\sigma = 4.3$  ps.

The synchronization of the laser pulse with the electron beam was achieved by using the 119-MHz subharmonic of the accelerator master oscillator frequency to drive the mode locker in the laser oscillator [47], as shown schematically in Fig. 14. The accelerator master oscillator, located in the injector area 3 km from the laser room, provided radio-frequency (RF) power at 476 MHz. This signal was transmitted via the Main Drive Line, a rigid coax cable that runs the length of SLAC’s klystron gallery, and was then transported by optical fiber [58] to the laser room. Here, it was demodulated by a fiducial output module, which

delivered the 4<sup>th</sup> subharmonic at 119 MHz; this signal was sent to the timing stabilizer [59] which controlled the mode-locker. The laser pulse train was viewed by a 20-GHz-bandwidth photodiode whose output was compared in the timing stabilizer with the phase of the reference RF to keep the two signals locked.

Every two seconds, one pulse was selected from the laser oscillator pulse train for further amplification and delivery to the interaction region. This was accomplished by using Pockels cells triggered by software-defined triggers which were synchronized with the master accelerator clock. The fine timing of this pulse was set by adjusting an optical delay line with subpicosecond resolution. A ringing cavity in the electron beam line provided a reference signal which was used to compare the phase of the laser signal to that of the electron bunch. Final timing was established by observing the  $e$ -laser scattering rate as a function of optical delay. A typical “timing curve” is shown in Fig. 15, with (standard deviation)  $\sigma = 4.3$  ps; this is the convolution of the pulsewidths of the two beams,  $\sigma_e \simeq 3$  ps,  $\sigma_{\text{laser}} \simeq 0.6$  ps, and of the time jitter  $\sigma_j$  between their centroids. A detailed analysis of the fluctuations in the collision rate [47] showed that the timing jitter between the laser pulses and the arrival of the electron bunch was typically of order  $\sigma_j \simeq 2$ -3 ps.

### 3.2 Electron Beam

Nominal values for the electron beam energy, charge, and pulse-to-pulse charge variation were 46.6 GeV,  $5 \times 10^9$  electrons per bunch, and  $\pm 0.3\%$ , respectively. Although the repetition rate of the electron beam could be set as high as 30 Hz, the experiment was limited by the laser repetition rate, which was 0.5 Hz in normal operating conditions. However, it was desirable to collect some electron beam background data when the laser was not firing. For this reason, the electron beam was operated at 10 Hz. The Final Focus Test Beam (FFTB) energy and launch feedbacks, although best optimized for 30-Hz repetition rates, performed reliably in this lower-frequency regime. During parasitic detector calibration runs [60], the beam rate was 120 Hz. To calibrate the CCD spectrometer, some data were taken with pulses of as few as  $10^7$  electrons transmitted at 1 Hz for 9 seconds, alternating with 30 Hz pulses of  $5 \times 10^9$  electrons for 1 second.

The laser-electron interaction point (IP1) was located at a secondary focus 12 m downstream from the primary focus of the FFTB. After passing through IP1, the electron beam and essentially all scattered particles continued in the forward direction to six permanent dipole magnets. In addition to bending the primary electron beam down into the beam dump, these magnets were used as this experiment’s electron and positron spectrometer, as described in the next section.

The electron beam parameters recorded for each event in a typical run were the charge, the energy offset of the beam relative to the central energy, and the transverse position and angle of the beam as measured by beam position monitors located close to the IP.

At IP1, it was possible to tune the beam to a transverse size of  $\sigma_x \simeq \sigma_y \simeq 60$   $\mu\text{m}$ ; longitudinally, the electron pulse could be adjusted to  $\sigma_z$  between 0.5 and 1 mm. The horizontal and vertical dimensions were measured by scanning the electron beam over 20- $\mu\text{m}$ -thick Al wires and observing the rate of the resulting bremsstrahlung photons. The

scanning of the electron beam was done using dipole steering magnets in the FFTB line upstream of the IP. The whole procedure was integrated into the SLC Control Program.

The longitudinal dimension of the bunch could be tuned by varying the bunch compressor voltage settings [61]. The effect of timing jitter on the synchronization of the 1.5 ps laser pulses with the electron bunches was less for longer electron bunches. For this reason, the electron bunches were kept longer than is usual for FFTB running, around 3.6 ps (rms).

The FFTB gets its beam directly from the SLAC two-mile linac. Unlike a recirculating collider, the constant production and extraction of bunches in a single-pass system means that the beam halo is repopulated on each bunch, and this requires a vigorous collimation system to eliminate particles at large excursions in position, angle and energy. The FFTB's primary collimation system is the SLAC linac collimators, which comprise a set of movable jaws in the last three sectors of the linac, and which serve as the primary collimation for SLC as well. The first set of these collimators does the primary collimation, while the second set is used to remove particles that were scattered of the first set. The linac collimators do not eliminate large-energy oscillations, nor are they adequate for regions with enormous betatron functions such as the FFTB. For this reason, the FFTB itself has a set of movable collimators, located in the first section of the FFTB line. The collimation was set up in such a way that neither too much beam was allowed to pass through (causing backgrounds by scraping on tight magnet apertures or the beam pipe itself), nor too much beam was cut away (causing off-energy repopulation and worse backgrounds). A measure of the success of the collimation system is the result that only one background positron was detected per  $10^3$  beam pulses of  $5 \times 10^9$  electrons each.

### 3.3 Primary Spectrometer and Calorimeters

The primary spectrometer consisted of six permanent magnets with mean fields of 0.5 T across a 2 inch by 36 inch poleface, providing a transverse kick of 816 MeV/c in the vertical plane to the primary electron beam. Because of the short height of the poleface, the magnets were positioned to maintain full field along the trajectory of the beam electrons, as shown in Fig. 16; trajectories of electrons and positrons for typical momenta are indicated as well.

On both sides of the IP were located soft bends of 0.06 and 0.5 mrad to reduce synchrotron radiation in the direction of the forward photons. Recoil electrons and positrons exited the vacuum chamber through 1/4-inch-thick stainless steel windows and were detected by sampling calorimeters, positioned as shown in Fig. 16. The electron calorimeter could be moved in the vertical direction, so that it only would detect electrons below a given momentum.

The electron calorimeter, referred to as ECAL, was made of alternating layers of silicon and tungsten; each layer of tungsten was one radiation length thick, and each silicon layer was 300  $\mu\text{m}$  thick, resulting in a sampling fraction of 1.1%. Each of the layers in ECAL was divided into 12 rows and 4 columns of  $1.6 \times 1.6 \text{ cm}^2$  active area pads, and the longitudinal layers for each tower are ganged into 4 segments [62], as shown in Fig. 17. The positron calorimeter, referred to as PCAL, was of identical construction, except that PCAL had an additional 4 rows. Electrons and positrons produced at the IP could only reach the two

central (inner) columns of the calorimeters; thus the outer pads could be used to measure backgrounds.

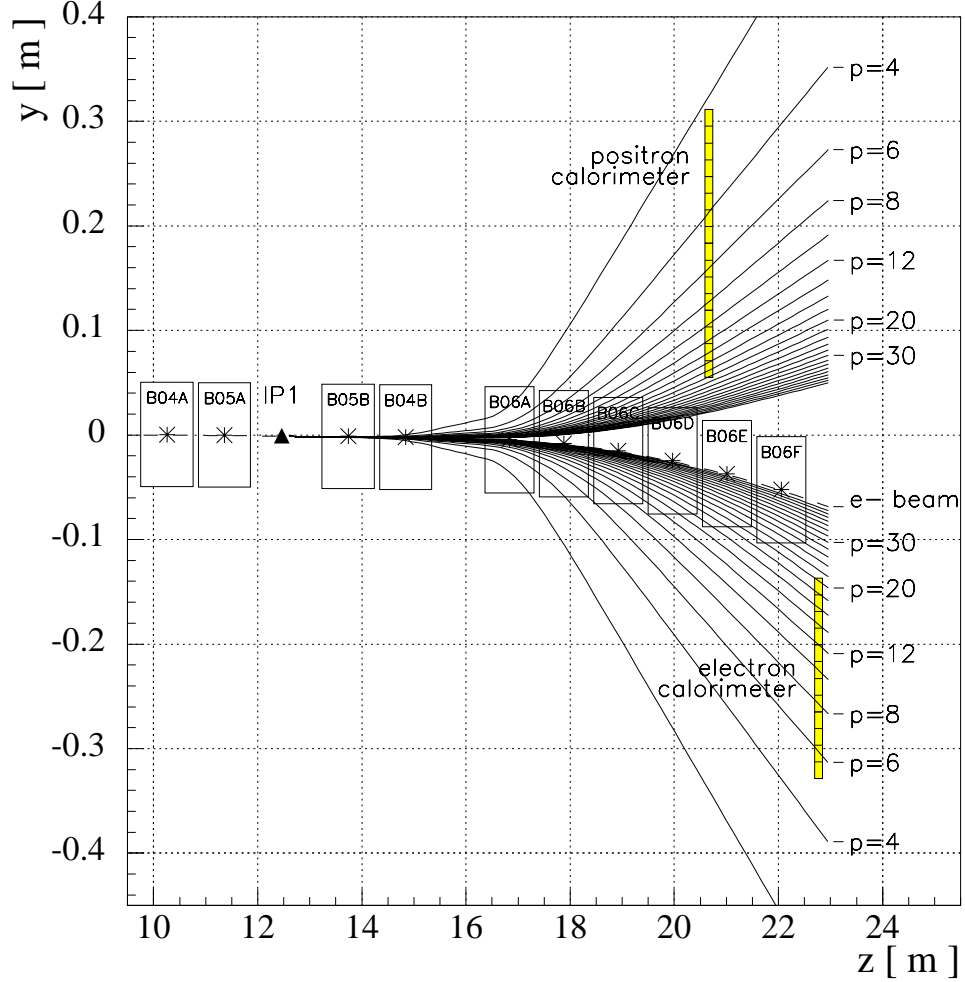


Figure 16: Calculated trajectories of electrons and positrons of different momenta through the magnetic spectrometer. The location of two calorimeters is shown as well.

The calorimeters were read out with modules built for a liquid argon calorimeter used in Fermilab experiment E-706 [63]. The calorimeters were calibrated in the FFTB line using low flux at variable momentum. The results of a calibration run for 13-GeV electrons are shown in Fig. 18. The resolution was found to be

$$\sigma_{\mathcal{E}}^2 = (0.19)^2 \mathcal{E} + (0.4)^2 + (0.05)^2 \mathcal{E}^2, \quad (62)$$

where  $\mathcal{E}$  is the electron energy in GeV. The transverse profile of the shower resulted in less than 6% leakage from the inner to the outer pads. The gain was set so that a single 10 GeV electron could be recorded, whereas the readout was saturated at a total energy of 10 TeV in a single tower.

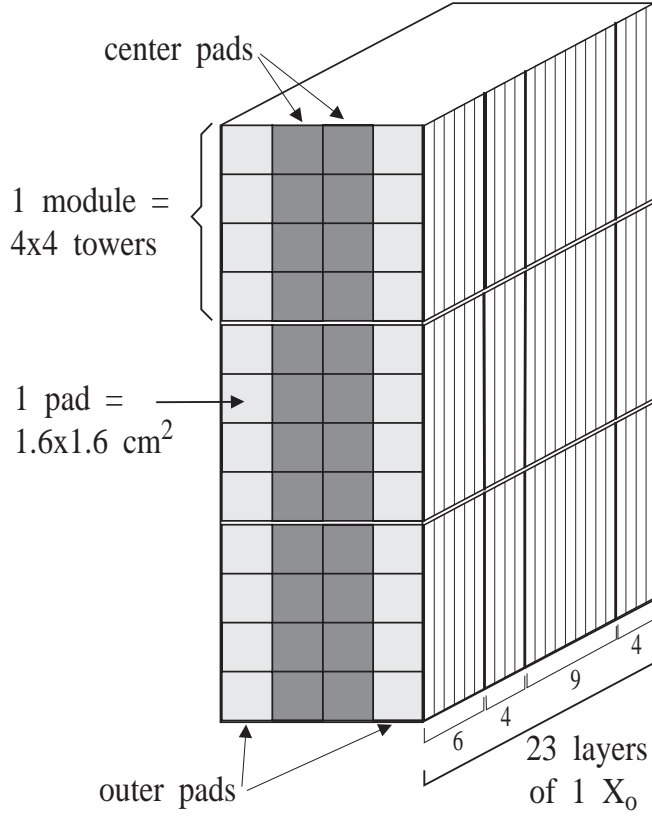


Figure 17: The electron calorimeter (ECAL).

For the data presented in sec. 5.2, the beam pipe on top of ECAL and vacuum chamber in front of ECAL were modified to reduce the rescattered-electron backgrounds, as modelled in GEANT v3.21 and EGS4 [64] Monte Carlo simulations. The modifications included the following:

- (a) An increase in the vertical size of the beam pipe on top of ECAL from 4.5 to 8.0 inches to contain not only the original 46.6 GeV electron beam, but also the  $n = 1$  spectrum of scattered electrons.
- (b) The thickness of the beam pipe on top of ECAL was reduced to 1/16 inches along the line where the  $n = 2$  electrons cross the beam pipe.
- (c) The thickness of the vacuum chamber in front of ECAL was reduced to 1/8 inches.
- (d) The vacuum flanges behind ECAL were moved 20 inches downstream.

As a result of the above modifications, backgrounds in ECAL were reduced by more than an order of magnitude. Backgrounds in later runs represented only a small fraction of the  $n = 3$  and 4 signal in ECAL, and they were easily dealt with by reconstruction procedure described in sec. 4.3. However, after the increase of the diameter of the beam pipe, part of the

$n = 2$  electron spectrum was also contained within the vacuum pipe, making it impossible to make further measurements with ECAL of the  $n = 1$  and  $n = 2$  portions of the Compton spectrum.

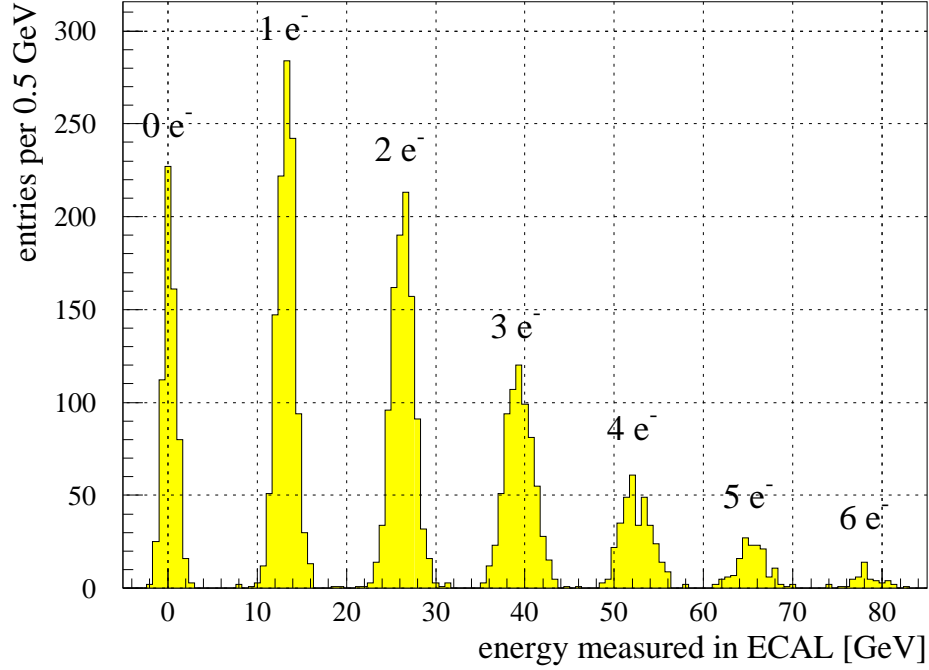


Figure 18: The response of the ECAL to 13-GeV incident electrons. The peaks due to the simultaneous arrival of up to six electrons are clearly distinguished.

### 3.4 Forward Photon Spectrometer

After the charged particles were deflected by the primary spectrometer magnets, the forward-going photons produced at IP1 passed into a separate beamline, the  $0^\circ$  line (Fig. 11). Two collimators cleaned the photon beam of synchrotron radiation and beam-scraping backgrounds. The photons either continued to a thin target in which a small fraction would convert into electron-positron pairs, or a movable Čerenkov counter (CCM1) was inserted into this beamline to monitor the total rate as described in the following section. In the former case, the electrons/positrons entered a momentum spectrometer consisting of a dipole magnet which provided a horizontal kick of 100 to 250 MeV/c, and 4 CCD planes to measure the particle tracks, as shown in Fig. 19. The forward photon spectrum could be inferred from electron/positron momentum spectrum.

Each CCD plane consisted of a pair of large-area CCD image sensors (EEV model CCD05-20, pixel size  $22.5 \times 22.5 \mu\text{m}^2$ ) and associated support electronics. The planes were mounted on remotely-controlled motion stages inside an evacuated chamber. Bulk cooling was provided by circulating chilled ethylene glycol in copper pipes brazed onto a copper backplane surrounding the CCD sensor; thermo-electric coolers further lowered the temperature of the



sensors to below 0°C, which significantly reduced leakage current. The CCD's were read out by frame-grabbers (Dipix model P360F) with built-in digital signal processing (DSP) capability. The on-board DSP chip acquired pedestal frames, calculated line-by-line DC-offset corrections, and converted signal level information into a stream of hit coordinates.

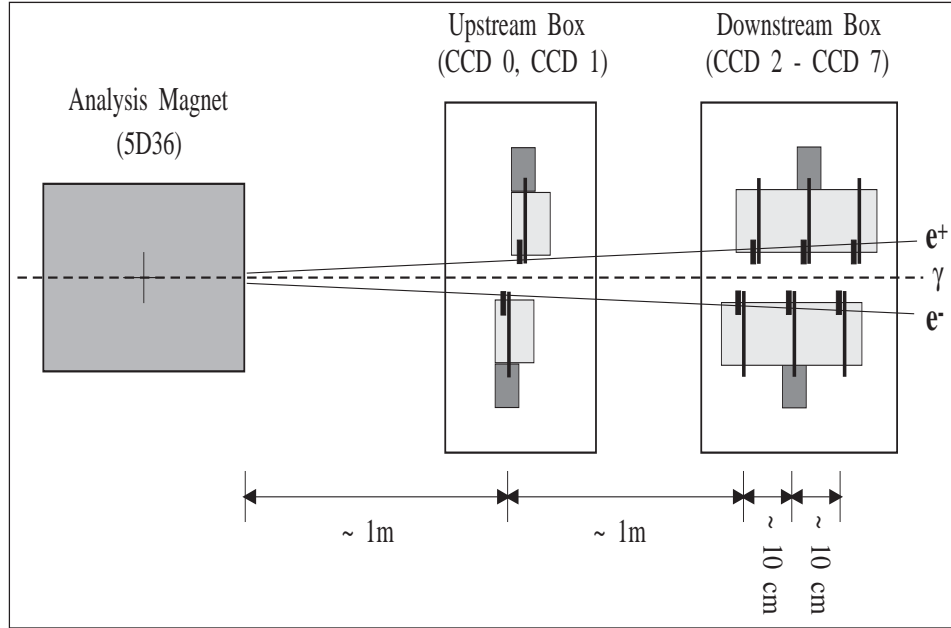


Figure 19: Schematic of the CCD pair spectrometer.

Proper steering of the high-energy photon beam through the collimators was required to minimize synchrotron backgrounds and undesirable beam-clipping effects. To accomplish this, a foil was inserted at the interaction point, which created an intense beam of high-energy photons with the same geometry as that due to laser backscattering. The electron beam trajectory was adjusted to maximize transmission of photons to the end of the 0° line, while minimizing the signal on four scintillators monitoring loss around the beamline downstream of the CCD's. Once this setting was established, the foil was removed and a computer-controlled feedback maintained the optimal beam steering.

When the foil at the interaction point was removed and the CCD stages were sent to their “home” position directly in the photon beamline, the CCD's were able to image the synchrotron light from the electron beam. The electron beam was then aligned such that the collimators blocked the synchrotron light from the 0.5-mrad bending magnets on either side of the interaction region. The weak synchrotron radiation from the 0.06-mrad bends remained, and a signal of “edge radiation” from electrons passing through the fringe fields just upstream and downstream of the IP1 identified the Compton backscattered beam position.

After beam steering, the positions of the photon converter and of the CCD's were determined to within 0.3 mm using the synchrotron light. The thicker photon-conversion targets blocked the synchrotron light when inserted in the beam, and so their boundaries could be located precisely relative to the CCD's in their “home” position. For analysis of the con-

verted photons, the CCD's were moved away from “home” by distances sufficient that no synchrotron radiation struck them.

For the data presented in this paper, the CCD spectrometer was used in “single-arm” mode, in which no attempt was made to reconstruct pairs by matching electrons with their positron partners. In this mode of operation, events of 100 tracks were easily accommodated. No attempt was made to use the CCD's in the front plane of the spectrometer in this mode, since the high number of hits led to significant ambiguity in the projection from the back planes to the front. As a consequence of using the spectrometer in “single-arm” mode, the photon spectrum is convolved with the Bethe-Heitler pair production spectrum. Nevertheless, the resulting spectrum is easily predicted, and the kinematic limits and relative scales of the  $n = 1$  and  $n = 2$  processes were clearly observed.

### 3.5 Forward Photon and $n = 1, 2, 3$ Electron Detectors

The forward-going photons served as the primary monitor of the interaction rate during much of the nonlinear Compton scattering study. These high-energy photons were detected by an air-Čerenkov counter (CCM1) [65] placed in the  $0^\circ$  line. We used a detector based on Čerenkov radiation, as this was less sensitive to major sources of background radiation such as bremsstrahlung or beam scraping. Figure 20 is a schematic of the CCM1 detector, which used 0.2 radiation lengths of aluminum as a converter and 2.5 cm of air as a radiator. The acceptance and efficiency of the Čerenkov volume and the transport to the photomultiplier were calibrated by inserting a thin foil in the electron beam at the IP. The photomultiplier gain-*vs.*-voltage curve and analog-to-digital converter response were carefully measured using known signal sources prior to data-taking. By adjusting the photomultiplier gain, the dynamic range of the counter could be varied over six orders of magnitude.

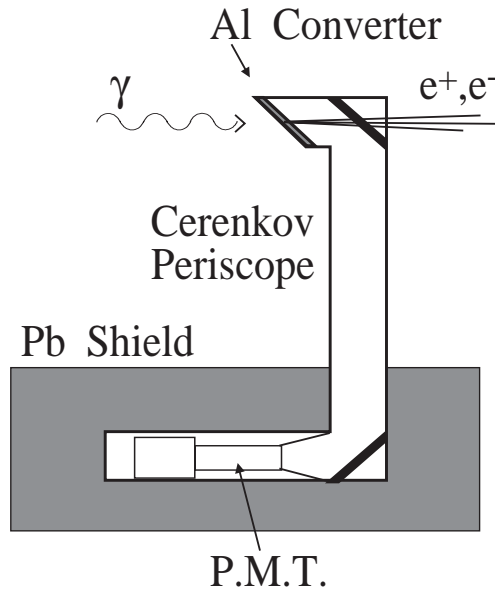


Figure 20: The forward photon monitor CCM1.

Similar Čerenkov counters were placed to intercept scattered electrons of 37, 31, 12.6, and 8.8 GeV/ $c$  momentum. These detectors were named EC37, EC31, N2MO, and N3MO, respectively; the last two names reflect the fact that for green laser light, the electron spectrum at 12.6 GeV/ $c$  is dominated by  $n = 2$  scattering, while  $n = 3$  scattering is the principal contributor to the spectrum at 8.8 GeV/ $c$  (see Table 2). The EC37 and EC31 detectors were cross-calibrated with CCM1 using data from the foil inserted into the primary electron beam as described above; they served as alternate measures of the  $n = 1$  interaction rate when CCM1 was removed to allow photons to proceed to the pair spectrometer. After careful characterization of the gain-*vs.*-voltage curves of the photomultipliers used in N2MO and N3MO, their acceptances and efficiencies were calibrated at high gain, *in situ*, using a low-rate, variable-momentum test beam. The measured acceptances of these counters as a function of electron momentum are shown in Fig. 21. A Si-W calorimeter at the end of the  $0^\circ$  line provided a redundant photon monitor.

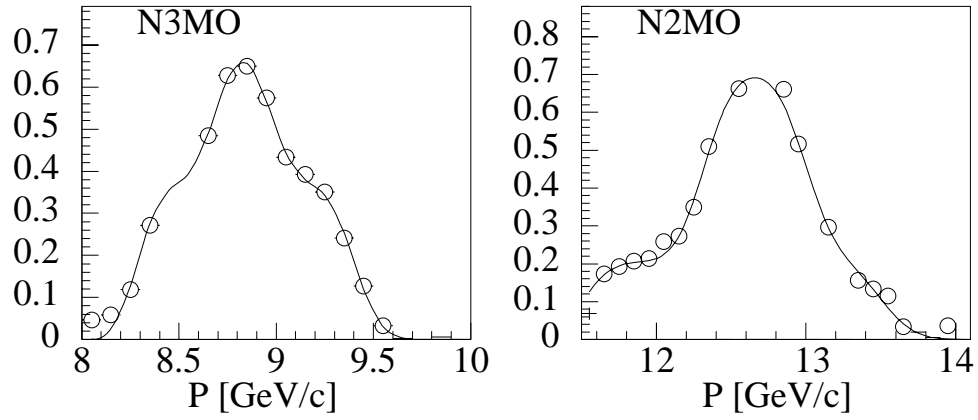


Figure 21: Measured acceptances of electron detectors N2MO and N3MO *vs.* electron momentum.

### 3.6 Data Acquisition System

The data acquisition system (DAQ) collected data from the detectors as well as information on the laser system and the electron beam. Although the accelerator provided electrons at 10 or 30 Hz, the DAQ recorded data less frequently. Every beam crossing when the laser fired, at 0.5 Hz repetition rate, constituted an event to be recorded in this experiment. In addition, data were collected from the electron beam pulses 400 msec and 200 msec prior to each laser shot, to measure electron-beam-related backgrounds in the detectors. A third set of events, obtained by dumping the electron beam far upstream in the linac, was used to measure the pedestal mean value and noise in the detectors and readout electronics during data-taking. These events occurred at a rate of 0.05 Hz, and one third of them coincided with laser shots.

The moderate event rate and data volume of the experiment allowed a low-cost solution for the data acquisition system, which is shown schematically in Fig. 22. The system was

based on IBM compatible personal computers connected by a local Ethernet. The communication between the computers was established using the standard TCP/IP and UDP protocols.

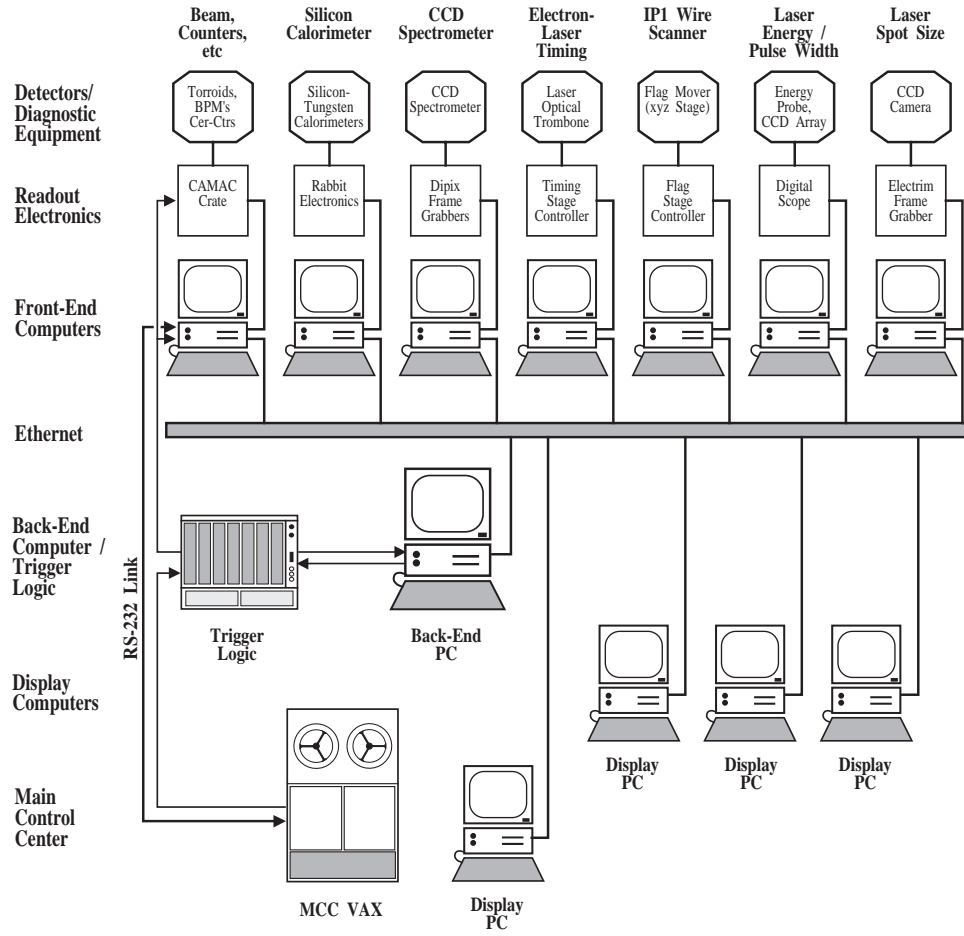


Figure 22: Components of the data acquisition system.

The main part of the DAQ system consisted of one back-end computer and several front-end computers. The back-end computer controlled and synchronized the DAQ system and provided the interface to the user, while the front-end computers collected data from the detectors and diagnostic equipment and responded to command messages received from the back-end computer. A standard interface between the programs running on the back-end computer and the front-end computers allowed for a modular and very flexible DAQ. The third type of computer shown in Fig. 22, the display computers, provided detailed online monitoring of the collected data.

The readout cycles were controlled by the trigger logic, which received triggers from the SLAC control system and distributed them to the readout electronics and/or front-end computers. Once a trigger signal passed through the logic, any further triggers were blocked until the logic was reset by a 'READY' signal from the back-end computer. Upon receiving a

trigger signal, each front-end computer collected its assigned set of data and sent it over the Ethernet link to the back-end computer, where the data were assembled, analyzed and stored to disk. When the back-end computer finished processing an event, it reset the trigger logic and broadcast the full event information to the display computers. The display computers, running unsynchronized to the readout cycle, allowed online monitoring of the experiment or individual front-end equipments, as well as CPU-intensive data processing. One display computer was set up in the accelerator control room to aid in tuning the electron beam for low background in the detectors.

An RS-232 link between one of the front-end computers and the master computer of the SLAC control system made it possible to bring additional experimental parameters into the data stream, as well as to perform special runs during which the position of the IP box and/or the ECAL were varied.

## 4 Data Collection and Analysis

### 4.1 Data Collection Strategy

To study the dependence of the nonlinear scattering process on laser intensity, data were taken at several different laser energies between 10 mJ and 800 mJ. Both IR ( $\lambda = 1053$  nm) and green ( $\lambda = 527$  nm) laser pulses were used, with circular and linear polarization. At the highest intensity, there were over  $10^7$  photons/event emitted in the forward direction. To avoid saturation, the ECAL was moved well below the kinematic edge for  $n = 1$  scattered electrons. However, the dynamic range of the ECAL limited the measurement to about two orders of magnitude of the nonlinear scattering rate at any particular position of the ECAL. Figure 23 shows the region accessible to the ECAL for different recoil electron momenta and laser energies for IR pulses, according to the rate calculations summarized in Fig. 4. The momentum acceptance of the ECAL pads is also indicated.

The data reported in sec. 5.1 were taken with the ECAL kept at fixed position for runs of at least 1000 laser-on events. These runs were taken for different laser intensities, and the position of the ECAL was chosen accordingly to avoid saturation. Keeping the calorimeter position fixed simplified real-time monitoring of the beam overlap quality and background subtraction.

In contrast, the data reported in sec. 5.2 were obtained with the ECAL position scanned in steps of  $1/4$  or  $1/2$  of a pad height, providing improved spectral resolution, and (nominally) constant laser intensity. For these data, the laser intensity was obtained from the nonlinear monitors N2MO and N3MO rather than directly from the measurement of the laser parameters.

To align the electron and laser beams in the transverse plane, a fluorescent flag was lowered into the path of the beam and viewed remotely. By moving the IP vacuum box, which held the focusing mirrors, it was possible to bring the electron beam and the He-Ne alignment laser images into overlap. Final adjustment was made by monitoring the forward-photon rate as a function of transverse ( $x$ - $y$ ) position of the IP box. While the vertical overlap ( $y$ ) was unambiguous, the overlap in the horizontal plane ( $x$ ) depended on

the relative timing of the two beams, as indicated in Fig. 24(a).

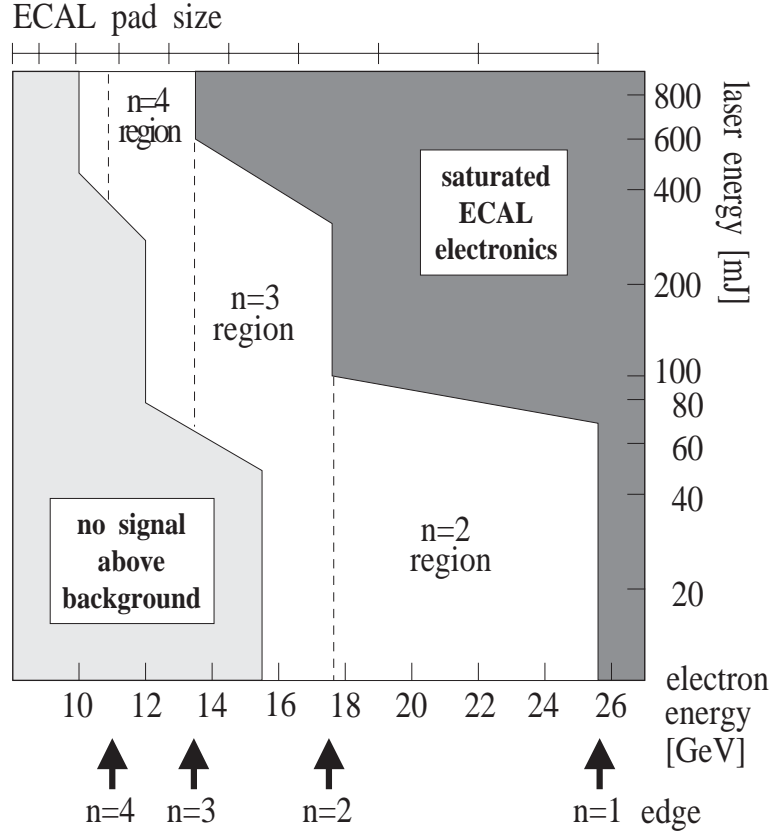


Figure 23: Portion of recoil electron spectrum accessible to the ECAL for different particle energies and laser energies for IR pulses. The acceptance of a single ECAL tower is shown at the top.

Thus, it was necessary to carry out a raster scan in both the  $x$ -position of the IP box and in timing delay. This is shown in Fig. 24(b), where the linear Compton scattering rate observed in the CCM1 detector is plotted as a function of  $\Delta x$  and  $\Delta t$ . The correlation between the two offsets,

$$\Delta x \left( \frac{1}{\sin \alpha} + \frac{1}{\tan \alpha} \right) = c\Delta t, \quad (63)$$

is clearly evident. In Fig. 24(c), the nonlinear rate observed in ECAL at a position corresponding to  $n = 2$  is plotted for the same raster scan. A large  $n = 2$  signal was obtained only when the electrons crossed through the peak field region of the laser beam, which identifies the optimal space-time alignment of the two beams more precisely than does the  $n = 1$  scan.

The  $x$ - $t$  scan data were also used to characterize backgrounds from linear ( $n = 1$ ) processes that contaminated the desired  $n > 1$  signal, using regions of the  $x$ - $t$  plane in which  $n = 1$  scattering was still large, but  $n > 1$  scattering was suppressed. Such  $x$ - $t$  scans were performed frequently during the run to assure correct spatial and temporal overlap. Each

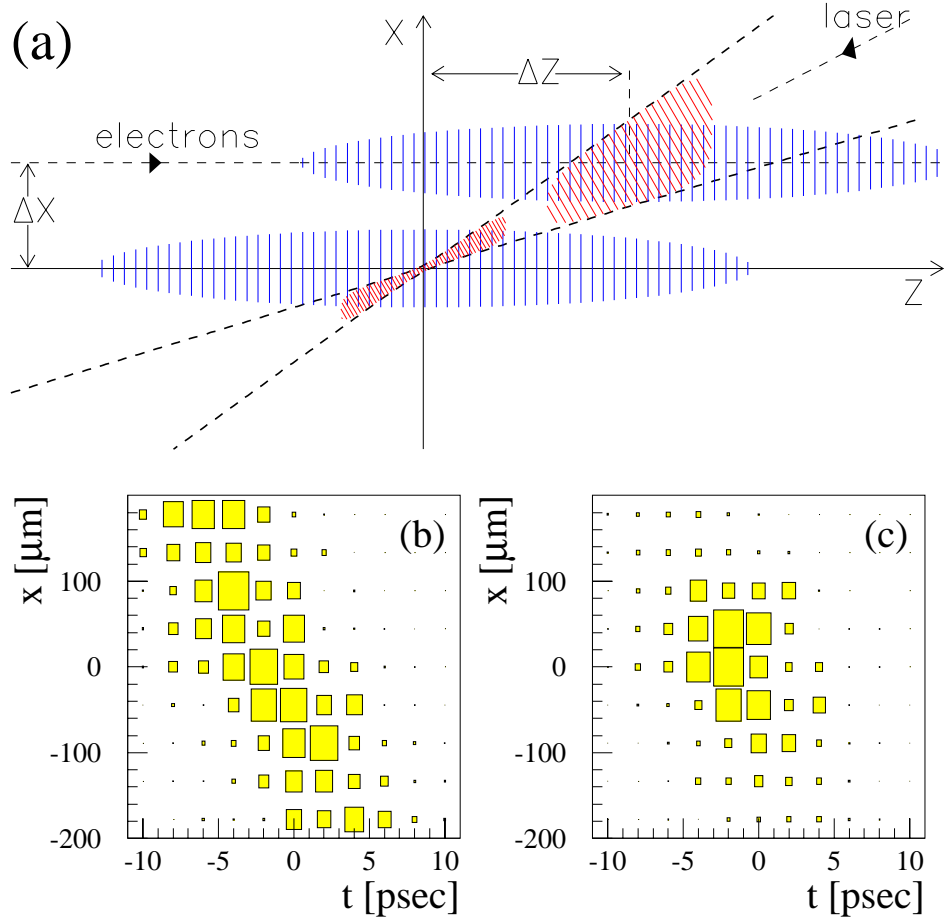


Figure 24: (a) The crossing of the laser pulse and electron beam in the  $x$ - $t$  plane; two possible collisions are shown, each giving approximately the same linear Compton scattering rate but drastically different non-linear Compton rates. (b) Linear Compton event rate as a function of transverse beam displacement and relative timing. (c) As above, but for the  $n = 2$  scattering rate.

$x$ - $t$  scan was preceded by a  $y$  scan to ensure that the electrons and photons were in the same plane, and by a  $t$  scan to verify the scan range and  $n = 1$  collision stability.

## 4.2 Determination of the Laser Intensity

The scattering rate depends strongly on the peak intensity,  $I$ , at the laser focus, so  $I$  must be known on an event-by-event basis for an accurate comparison between data and theory. We measured the value of the intensity by two different methods.

### 4.2.1 Direct Measurement

Measurements of the laser parameters, as discussed in sec. 3.1 were used to determine  $I$  as follows. The laser power  $P$  was fitted to a Gaussian shape as a function of time, yielding the standard deviation  $\sigma_t$ , and pulse length  $\tau = \sqrt{2\pi}\sigma_t$ . An image of the focal spot was fitted to Gaussians in the horizontal and vertical projections, and the effective area was defined by  $A = 2\pi\sigma_x\sigma_y$ . Together with a measurement of the pulse energy  $U$ , the peak intensity is given by

$$I = \frac{U}{A\tau}. \quad (64)$$

The intensity was varied over the range  $I = 10^{16}$  to  $2 \times 10^{18}$  W/cm<sup>2</sup>. The corresponding rms electric field is given by

$$E_{\text{rms}} = \sqrt{Z_0 I}, \quad (65)$$

where  $Z_0 = 377 \Omega$ , and  $E_{\text{rms}}$  is given in V/cm for  $I$  in W/cm<sup>2</sup>. From this, the parameter  $\eta$  was calculated according to (4).

For the infrared laser data all three quantities, laser energy, focal-spot area, and pulsewidth, were measured for every pulse, as summarized in Fig. 25. The uncertainty in the pulsewidth was 20% because of diffraction of the laser beam. Fluctuations in the probe calibration led to a 13% uncertainty in the energy measurement. Because of laser light scattering, filtering, and the non-Gaussian shape of the focal spot, the uncertainty in the area was 20%. The overall uncertainty in peak IR intensity was therefore 30%.

For the green laser data, the energy and focal area were measured for each pulse, but the pulsewidth is known only on average for each data set from streak-camera and autocorrelation measurements, and varied between  $\tau = 1.5$  to 2.5 ps. Thus, we assign an uncertainty of  $^{+50}_{-30}\%$  for the green laser data.

The above procedure was used to establish the dependence of nonlinear Compton scattering on the laser intensity (sec. 5.1). Once this dependence was found to be in agreement with the theoretical prediction, it was convenient to obtain the peak laser intensity for each event from the rates observed in the linear and nonlinear Compton scattering monitors, by the following indirect method.

### 4.2.2 Indirect Measurement

We designate by  $N_1$ ,  $N_2$ , and  $N_3$  the numbers of electrons intercepted by the gas Čerenkov counters EC37, N2MO and N3MO, of first-, second- and third-order Compton scattering, respectively. An overall effective intensity was extracted from ratios of these monitor rates, as the ratios are less sensitive to the effects of  $e$ -laser timing jitter and fluctuations in spatial overlap. For  $\eta^2 \lesssim 1$ , the field intensity is given to a good approximation by

$$\eta^2 = k_1 \cdot \frac{N_2}{N_1}, \quad \text{and} \quad \eta^2 = k_2 \cdot \frac{N_3}{N_2}. \quad (66)$$



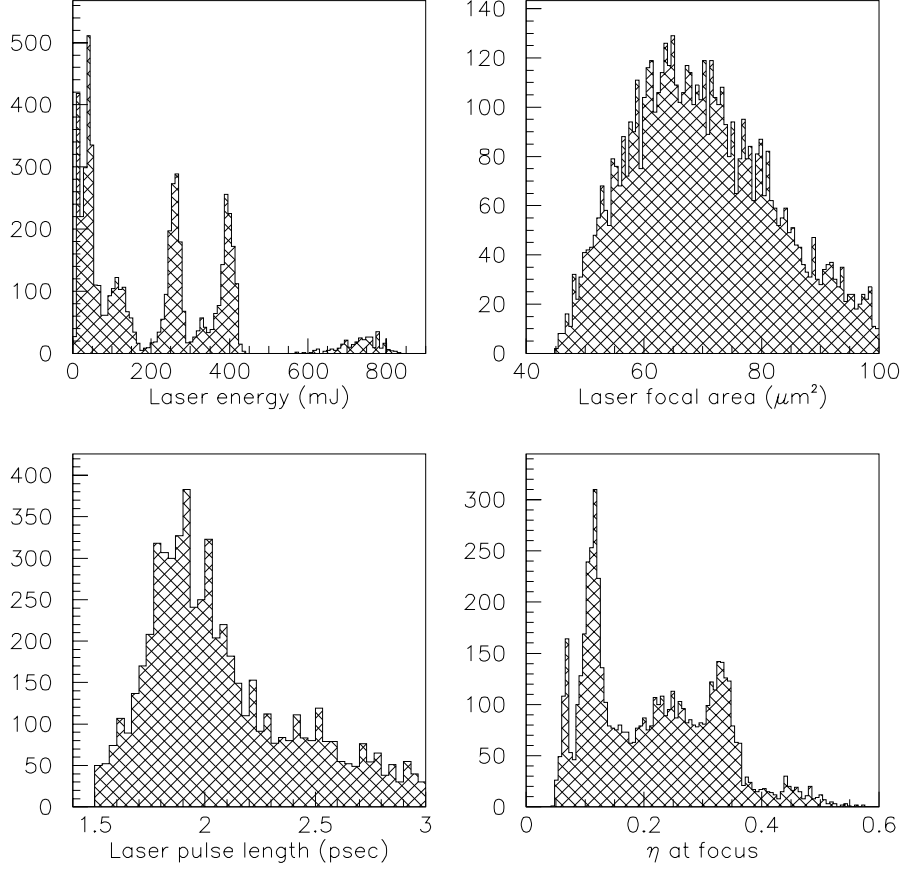


Figure 25: Laser parameters for all data taken with IR pulses. The value of  $\eta$  at the laser focus was calculated by the direct method described in the text.

The parameters  $k_1$  and  $k_2$  depend on the acceptances and efficiencies of the counters, as well as on the spectrum of scattered electrons, and must satisfy the constraint imposed by (66):

$$N_2^2 = \frac{k_2}{k_1} N_1 N_3. \quad (67)$$

An overall constrained fit was made to the measured values of  $N_i$  to extract  $(k_2/k_1)$ , and thus  $\eta^2$  for each event. The fit determined  $\eta$  with an average precision of 11%. Uncertainties in the acceptance, background levels, calibration and efficiency of the monitors caused a systematic error of  ${}^{+8}_{-13}\%$  in the absolute value of  $\eta$ . The intensity at the laser focus deduced by this method is in good agreement with the average value calculated from the measured laser parameters. For more details, see [66].

The indirect measurement of the laser intensity was used in the analysis of the  $e^+e^-$  pair production data (sec. 6.2), as well as for the ECAL scan data (sec. 5.2).

### 4.3 Electron Calorimeter Data

The total energy in a calorimeter tower (*i.e.*, all longitudinal segments of a given row and column, see Fig. 17) is a measure of the number of electrons scattered during the pulse into the momentum interval spanned by the tower. The energy distributions in the top six rows of the ECAL are shown in Fig. 26 for a particular run (for the initial configuration of the dump-magnet vacuum chamber). The rapid variation of the signal with momentum is obvious, as expected from the spectrum simulated in Fig. 4. Indeed, when the signal in ECAL row 1 approached saturation, rows 5 and 6 were generally compatible with zero signal, and only the first four rows for every calorimeter position have been included in the analysis.

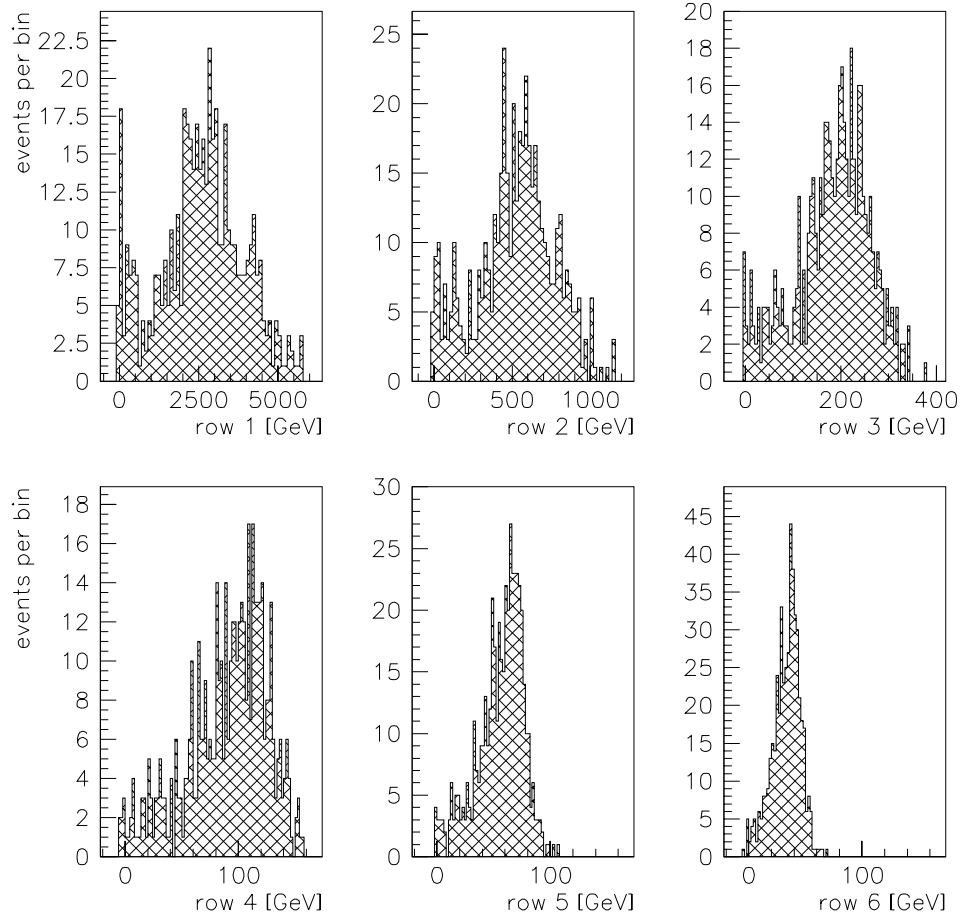


Figure 26: The ECAL signal for  $\sim 1600$  pulses of IR laser of 400 mJ, with the ECAL positioned to accept electrons with energies less than 15.5 GeV. The energy distribution obtained in the center pads for rows 1-6 is shown, with pedestals and electron-beam-only backgrounds subtracted, but without any other corrections.

The data in Fig. 26 have pedestals and electron beam background subtracted, but are not corrected for laser-on backgrounds or for shower spreading.

The principal laser-on background in the calorimeter is due to effects of electrons from  $n = 1$  Compton scattering. A significant fraction of these electrons passed through the vacuum pipe and/or struck obstacles downstream of the calorimeter, and created electromagnetic showers. Some portion of these showers reached the calorimeter and gave rise to a position-dependent background. Measurements of this background were made using data from the  $x$ - $t$  scans described at the end of sec. 4.1. The background was initially substantial, and the vacuum chamber near the ECAL was modified to help suppress it in the later phases of the experiment, as discussed in sec. 3.3.

Another analysis issue is the effect of spreading of the electromagnetic showers of signal electrons in the calorimeter. Because of the rapid variation of deposited energy with ECAL row number, “feed-down” of energy from an upper row,  $i$ , to the one below it,  $i + 1$ , caused a significant distortion of the energy spectrum. Similarly, the top row, 1, suffered partial loss of shower energy that escaped out the top surface.

#### 4.3.1 Spectrum Reconstruction and Background Subtraction

The goal of the analysis of the electron calorimeter data is the spectrum of energy,  $F_i$ , incident on row  $i$  of the calorimeter due to nonlinear Compton scattering. This was obtained from the observed data,  $D_i$ , in the calorimeter via a reconstruction matrix  $R_{ij}$  such that

$$F_i = \sum_j R_{ij} D_j \quad (68)$$

The determination of the matrix  $R_{ij}$  was based on calibration data that we expressed as a response function  $X_i(y, E)$ , which gives the amount of energy deposited in row  $i$  by an electron of energy  $E$  incident at height  $y$  on the ECAL. This vector is normalized to  $\sum_i X_i(y) = 1$ .

We used two different methods to obtain the matrix  $R$ . The first method [39] is based on an iterative approach to the shape of the electron spectrum  $f(y)$ . At each iteration, the desired ECAL energy spectrum  $F$  was modelled as

$$F_i = \int_{y_i}^{y_{i+1}} f(y) dy, \quad (69)$$

while the observed data  $D$  were modelled as

$$D_i = \int dy f(y) X_i(y). \quad (70)$$

Since the detector response function  $X$  is known, we could construct a matrix  $M$  that predicts the observed data as

$$D_i = \sum_j M_{ij} F_j. \quad (71)$$

The reconstruction matrix  $R$  needed for (68) is just the inverse of  $M$ . The initial hypothesis for  $f(y)$  was a polyline fit to the observed data  $D_i$ . The procedure converged well after 2 iterations. The effects of rescattered  $n = 1$  electrons and feed-down from row to row were accommodated by extensions of the basic procedure.

The second method [67] is based on adjusting the matrix elements  $R_{ij}$  (by minimizing a relevant  $\chi^2$ -distribution), so that the calculated acceptance of each row approached its geometrical shape. Note that combining eqs. (68) and (70) implies

$$F_i = \int dy f(y) \sum_j R_{ij} X_j(y) = \int dy f(y) g_i(y), \quad (72)$$

where

$$g_i(y) = \sum_j R_{ij} X_j(y) \quad (73)$$

is called the aperture function for the reconstructed signal. We optimized the coefficients  $R_{ij}$  such that, as nearly as possible,  $g_i(y)$  is zero for  $y$  outside the aperture  $[y_i, y_{i+1}]$  of channel  $i$ , and is unity inside. For this, we did not need to assume a particular form for the incident electron spectrum  $f(y)$ .

The observed data include background energy, primarily from rescattered  $n = 1$  electrons, and the reconstruction procedure should remove this from the reported signal. The response of ECAL to this background was written as a set of coefficients  $B_i$ , that were found from fitting the  $x$ - $t$  scans away from the nonlinear signal, and that express the raw ECAL signal due to rescattered electrons divided by the total number of electrons scattered at IP1. The observed data in ECAL from an incident electron spectrum  $f(y)$  and  $N_S$  electrons scattered at IP1 is therefore given by a modification of (70):

$$D_i = N_S B_i + \int dy f(y) X_i(y). \quad (74)$$

Thus, when the data vector  $D$  is inserted in (68) to obtain the background-free reconstructed electron spectrum, the effect of matrix  $R$  on the background vector  $B$  must be that  $\sum R_{ij} B_j = 0$ . This provided additional constraints on the procedure for constructing the matrix  $R$ .

Both methods gave similar results, and are discussed in more detail in appendix B, which also includes information on the calibration data.

### 4.3.2 Event Cuts

Cuts were applied to eliminate events where the electron beam fluctuated in position, angle or intensity, or when there was poor  $e$ -laser overlap as determined by the ratio of the forward-photon monitor (CCM1) signal to that expected for the measured values of laser parameters for that event. About 2/3 of the events were thereby rejected.

### 4.3.3 Normalization and Error Analysis

From the reconstruction of the energy  $F_i$  incident on calorimeter row  $i$  corresponding to electron momentum  $P_i$ , we obtained  $dN/dP$ , the number of incident electrons per momentum interval for each event. The value of the Compton spectrum  $F_i$  used here was the average of the results of the two analysis methods described above.

The event-to-event spread in the energy observed in a calorimeter row was due to several factors, the dominant one being variations in the overlap of the electron beam and laser pulse

due to timing fluctuations. To a good approximation, these fluctuations are reflected in the number of forward photons per event,  $N_\gamma$ , which measures the total scattering rate. Thus, by normalizing the ECAL signals to  $N_\gamma$  on an event-by-event basis in subsequent analysis, a more stable distribution is obtained. Part of the spread was due to the variation in laser intensity for different pulses; this is accounted for by normalization to  $N_\gamma$ . Only a small contribution came from statistical fluctuations, since there were usually 10-100 electrons per event incident on the calorimeter.

Therefore, we report the yield

$$\frac{1}{N_\gamma} \frac{dN}{dP}, \quad (75)$$

where  $N_\gamma$  is the number of high-energy photons emitted from IP1 as measured in the forward-photon monitor. The scattered electron data presented in sec. 5.1 were binned according to laser intensity and recoil momentum independent of the particular run, calorimeter position, or calorimeter row from which they were acquired.

The measurement uncertainty in each reconstructed data point was the sum in quadrature of two effects:

- (a) The statistical uncertainty due to the number of observed electrons.
- (b) The uncertainty due to the reconstruction algorithm, taken to be the maximum of the error estimate of the second reconstruction algorithm, or the difference in the results of the two algorithms.

## 4.4 Forward Photon Spectrometer Data

Some data were collected with the forward-photon monitor removed from the  $0^\circ$  beamline, and a thin foil inserted to convert a small fraction of the forward photons to electron/positron pairs. These were deflected by 10-30 mrad into the CCD spectrometer by a 5D36 magnet, as shown in Fig. 11.

Electron/positron tracks were reconstructed using the three back planes of CCD's (see Fig. 19). All triplets of points from the back CCD planes of a given arm were tested to see if they fit a line intercepting a region near the center of the spectrometer magnet. For any candidate tracks that shared more than one hit, only the track with the lowest  $\chi^2$  goodness-of-fit was kept. This set of candidate tracks included many "fake" tracks from thermal noise, and combinatoric background of points from different particles.

To convert positions in CCD-relative coordinates into positions in a common coordinate system, a more precise alignment of the CCD planes with respect to each other was required than was possible using the synchrotron radiation image technique described earlier. This was accomplished using real track data, yielding relative spatial alignment of  $30 \mu\text{m}$ . Slight rotations, as well as offsets in the horizontal and vertical directions, were measured and corrected.

After all alignment and track reconstruction was completed, a slight variation with magnet setting was noted in the apparent momentum of the kinematic edges. This was interpreted as arising from either an error in the measurement of the magnet saturation curve,

or an overall systematic rotation of the CCD planes. It was corrected by increasing the magnitude of all track horizontal angles 0.36 mrad.

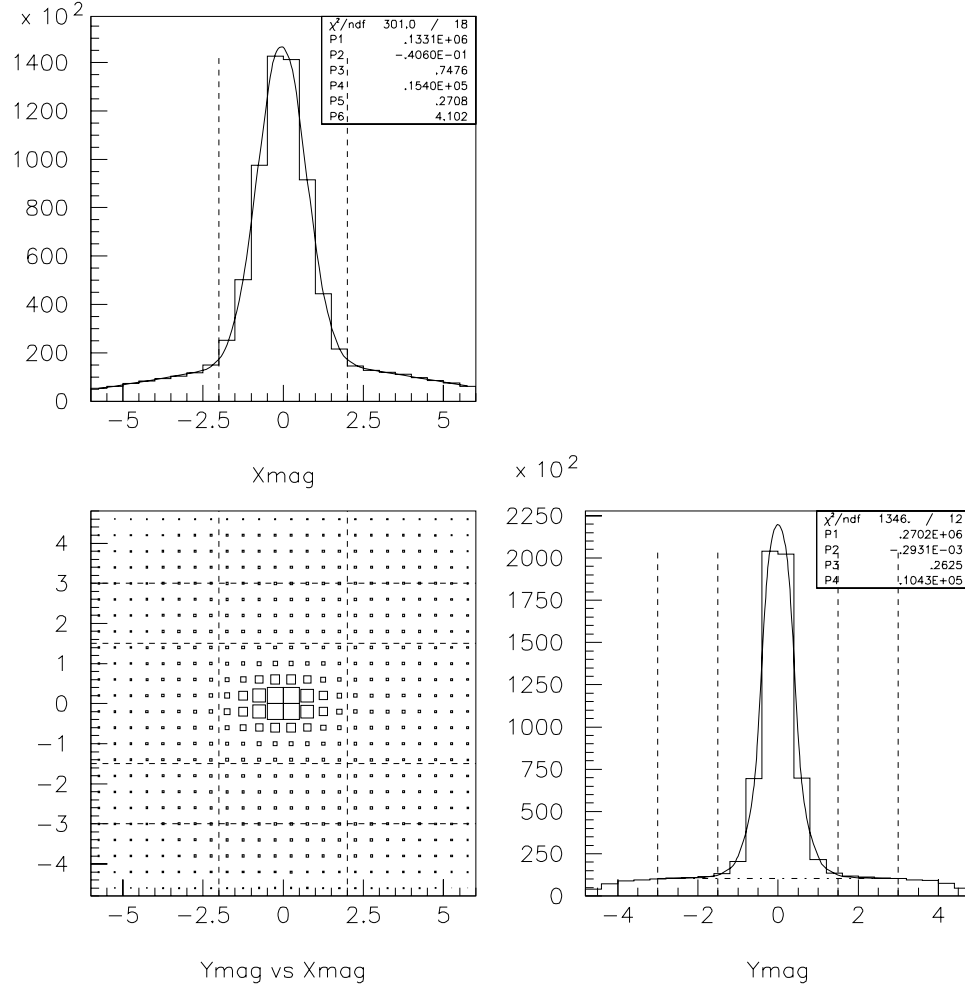


Figure 27: The two-dimensional distribution of the track positions at the center plane of the 5D36 magnet; the box size is proportional to number of tracks in the bin. Projections on the two transverse axes are also shown. Distances are in mm.

Figure 27 shows the observed distribution of the positions of tracks at the center plane of the magnet. This distribution is well described by a sum of two Gaussians: a narrow one with  $\sigma \approx 0.6$  mm, consistent with the expected track angle resolution of the system; and a wider one with  $\sigma \approx 6$  mm, consistent with the expected distribution of combinatoric backgrounds.

Figure 28 shows the distribution of magnet-plane intercept positions for tracks in the electron arm whose horizontal angle is smaller than that corresponding to the  $n = 1$  Compton kinematic edge. The distribution is well described by two Gaussians, but in this case, the combinatoric background is displaced away from the center position of the magnet, and is much higher than the signal. This occurred because the combinatoric backgrounds are

dominated by points on low momentum tracks, and these are farther from the  $0^\circ$  beamline. Low-angle combinatoric backgrounds from these tracks therefore tend to project back to a position away from the center of the magnet. An identical distribution is found for tracks in the positron arm.

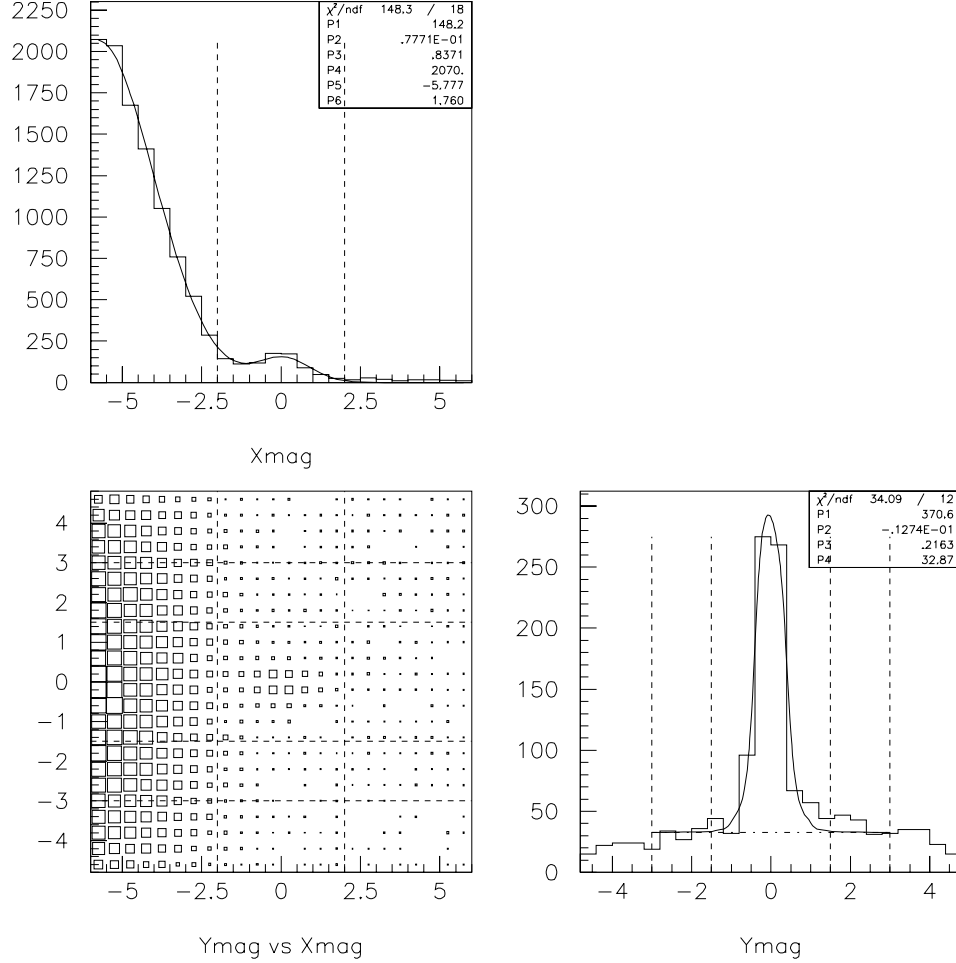


Figure 28: The distribution of the track positions at the center plane of the magnet, using only high momentum electron tracks. Distances are in mm.

To limit the number of “fake” tracks contaminating the signal, further analysis was confined to tracks whose horizontal position at the magnet center plane obeyed  $|x_{\text{mag}}| < 2$  mm. The signal region was defined as  $|y_{\text{mag}}| < 1.5$  mm, and the region  $1.5 < |y_{\text{mag}}| < 3$  mm was used for estimation of the background in the signal region.

Momentum spectra of signal and background tracks were accumulated for five ranges of  $\eta$  and fitted to theoretically-predicted spectra, as discussed in sec. 5.3. For more details, see [67].

## 4.5 Positron Identification

Positrons produced at IP1 were detected in the PCAL calorimeter, but it was not possible to identify their electron partners because of the high rate of Compton scattered electrons in the ECAL.

The response of PCAL to positrons originating at IP1 was studied by inserting a wire into the electron beam at IP1 to produce  $e^+e^-$  pairs by Bethe-Heitler conversion of bremsstrahlung photons. These data were used to develop an algorithm to group contiguous PCAL cells containing energy deposits into clusters representing positron candidates. The clusters were characterized by their positions in the horizontal and vertical directions, and by their total energy deposit  $E_{\text{clu}}$ . Using field maps of the magnets downstream of IP1, the vertical impact position was translated into the corresponding momentum  $P_{\text{clu}}$ . The efficiency of the cluster-finding algorithm was found to be  $93 \pm 1\%$  in a study where simulated clusters were added to laser-off data [66].

Fig. 29 shows the spectrum of calibration clusters found in row 7 of the PCAL as a function of the ratio  $E_{\text{clu}}/P_{\text{clu}}$ . The one-, two-, and three-positron peaks can be clearly distinguished.

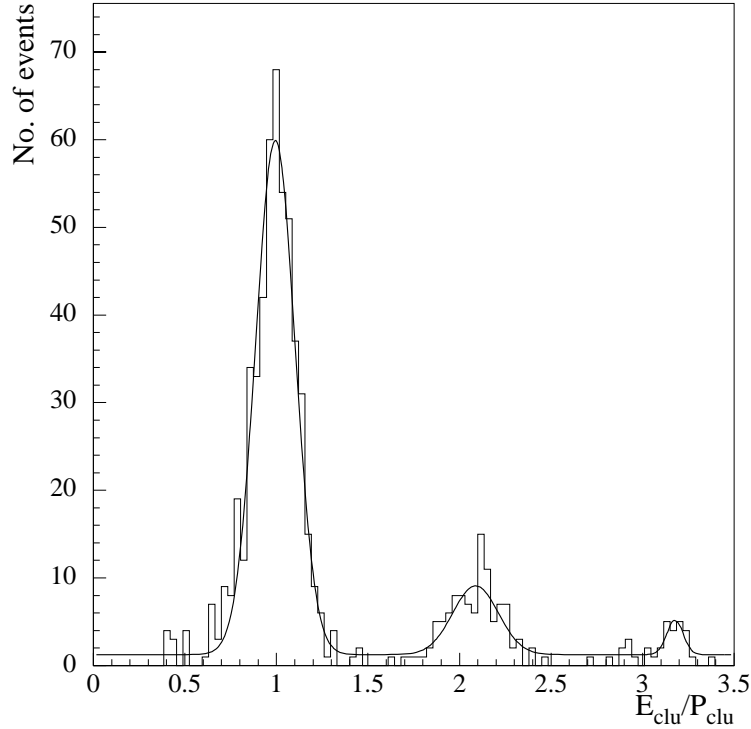


Figure 29: Distribution of the ratio  $E_{\text{clu}}/P_{\text{clu}}$  for calibration clusters in PCAL row 7, which spans momenta from 20.3 to 21.5 GeV.

Positrons were also produced in showers initiated by lost electrons upstream of the interaction region. This background could be severe, but was minimized by careful tuning of the beam. It was studied by accumulating data in the presence of the electron beam, but with the laser off.



## 5 Results on Nonlinear Compton Scattering

Nonlinear Compton scattering, (1), was studied by measuring the scattered electrons, as well as by observing the forward high-energy photons. In section 5.1, we discuss results where the ECAL detector was held at a fixed position and the laser intensity was varied. In section 5.2, we present results where the nominal laser intensity was held fixed and the ECAL detector was scanned to cover the momentum range of electrons from  $n = 3$  and  $n = 4$  scattering in an almost continuous fashion. Then in section 5.3, we present the results from the measurement of the electron/positron spectrum of converted forward photons.

As discussed in sec. 2, the presentation of the results of a nonlinear scattering process is best done in terms of rates, rather than cross sections, as the latter are not well defined for initial states involving multiple laser photons. In general, because of the continuous variation of the photon density across the laser focus and the nonlinear nature of the scattering, the data do not correspond to a rate for a single set of experimental parameters, but to an integral over a range of conditions. Therefore, the results given below are compared with those from a simulation of the experiment based on the theoretical model discussed in sec. 2.

Another important feature in the presentation of our results is that the observed nonlinear spectra, such as  $(1/N_\gamma)(dN/dP)$ , are normalized by the total number of scattered photons,  $N_\gamma$ , as discussed in sec. 4.3. This has the important advantage that fluctuations in the timing and spatial overlap are compensated for, in first order.

### 5.1 Scattered Electron Spectra *vs.* Laser Intensity

We present data for circularly polarized IR ( $\lambda = 1053$  nm) and green ( $\lambda = 527$  nm) light. The total number of events before and after cuts for the IR and green are shown in Table 3. The principal reason for rejecting events was poor  $e$ -laser overlap, as indicated by a low value of the ratio of observed to expected numbers of forward photons.

Table 3: Numbers of Events.

	IR	Green
Before cuts	18,344	16,322
After cuts	7,207	5,342

The variation of the laser parameters over the entire data set was shown in Fig. 25 for the IR runs. While the laser was operated with only six nominal pulse energies, fluctuations in the output energy, area, and pulse length were large enough that the laser intensity spectrum was essentially continuous.

Figures 30 and 31 show the differential yield,  $(1/N_\gamma)(dN/dP)$ , for electrons scattered from the IR and green lasers, respectively, at six different laser intensities. The observed yield is shown as a function of momentum by the solid circles; the horizontal error bars give the width of the corresponding momentum bin, and the vertical bars include systematic errors in reconstruction. The overall systematic uncertainty of  $\pm 30\%$  for the IR laser intensity and

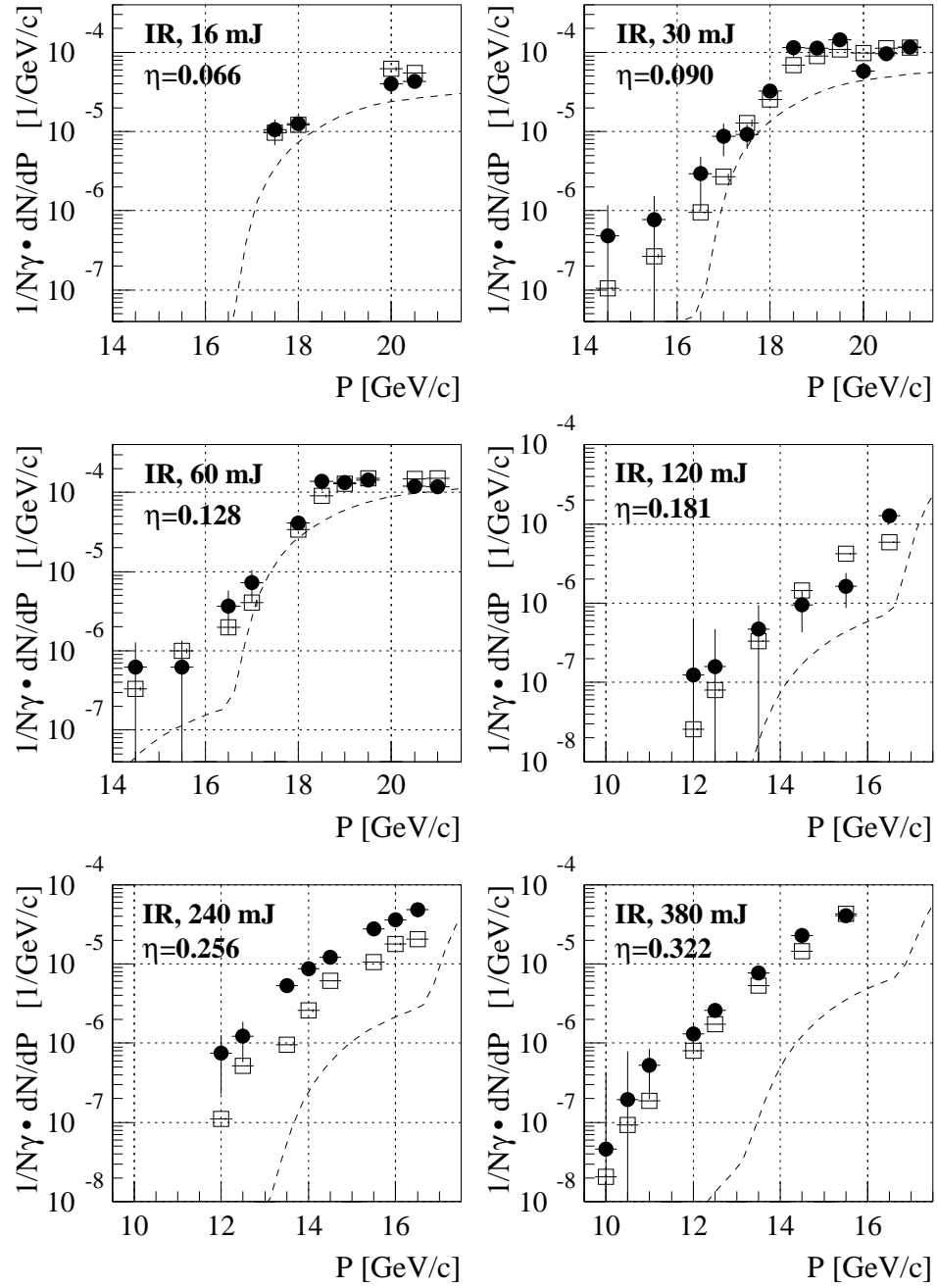


Figure 30: The yield of nonlinearly scattered electrons,  $(1/N_\gamma)(dN/dP)$  vs. momentum  $P$ , for six different circularly polarized IR laser energies. The data are the solid circles with vertical error bars corresponding to the statistical and reconstruction errors added in quadrature. The open boxes are the simulation, with error estimates indicated by the horizontal and vertical lines. The effect of systematic uncertainty in the laser intensity is not shown. The dashed line is the simulation of  $n = m$  plural scattering.

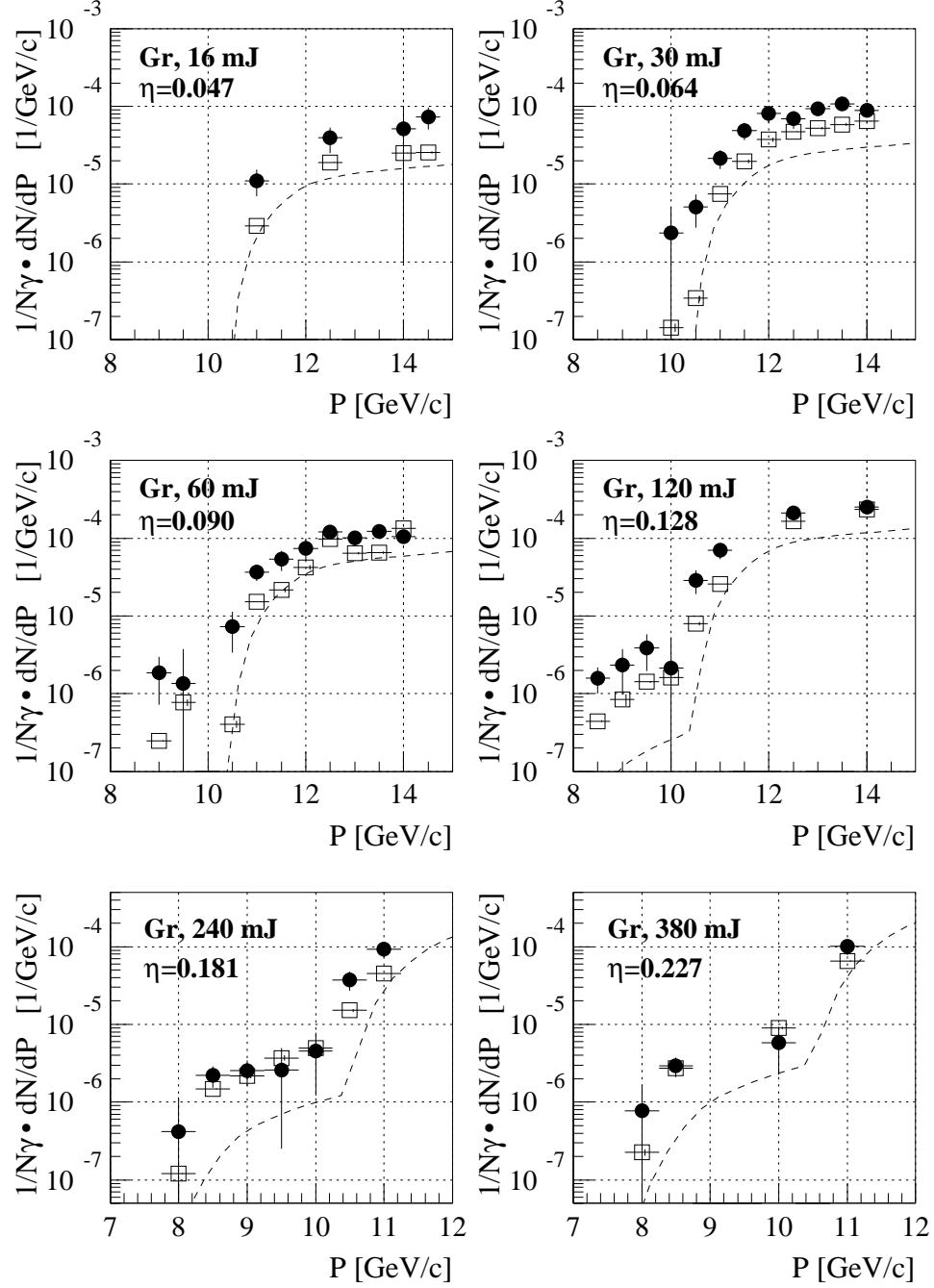


Figure 31: The yield of nonlinearly scattered electrons,  $(1/N_\gamma)(dN/dP)$  vs. momentum  $P$ , for six different circularly polarized green laser energies. The data are the solid circles with vertical error bars corresponding to the statistical and reconstruction errors added in quadrature. The open boxes are the simulation, with error estimates indicated by the horizontal and vertical lines. The effect of systematic uncertainty in the laser intensity is not shown. The dashed line is the simulation of  $n = m$  plural scattering.

$^{+50}_{-30}\%$  for the green laser intensity is not shown. The data and simulations are also given in Tables 5 and 6.

In general, each plot in figs. 30 and 31 covers three orders of magnitude in yield. The  $n = 2$  plateau and the dropoff to  $n = 3$  scattering (near the kinematic edge at 17.6 GeV for IR, 10.8 GeV for green) are evident at lower laser intensities. In the green laser data, one can also recognize the  $n = 3$  plateau, which extends from 10.8 to 7.8 GeV.

The simulation, including both nonlinear Compton scattering, (1), and plural Compton scattering, (38), is shown by the open boxes. For each event, the simulation incorporated the measured laser and electron beam parameters, including beam-beam timing and spatial overlap.

A simulation that ignores nonlinear Compton scattering, and thereby includes only  $n = m$  plural scattering, is shown by the dashed curve. The effect of detector resolution on shifting the position of the inflection between  $n = 2$  and  $n = 3$  scattering to lower momentum by 0.5-1 GeV/ $c$  is especially noticable in this case. The data at higher laser intensities cannot be accounted for by plural scattering only, and clearly indicate the presence of nonlinear Compton scattering.

While the data follow the simulation over three orders of magnitude there are significant disagreements between data and simulation if the systematic uncertainty in laser intensity is ignored. The overall  $\chi^2/\text{dof}$  (degrees of freedom) for comparison of data and simulation over the entire data set in Figs. 30 and 31 are then 488/49 and 188/41, respectively. If, however, the average laser intensity for each of the plots at a nominal laser pulse energy is adjusted to minimize the  $\chi^2$ , we find

$$\chi^2(\text{IR})/\text{dof} = 133/43, \quad \chi^2(\text{Green})/\text{dof} = 112/35.$$

The scale factors by which the nominal laser intensity would be multiplied to obtain the reduced  $\chi^2$  are given in Table 4. Since data at different laser intensities were taken under significantly differing experimental conditions and backgrounds, the spread of scale factors appears reasonable.

Table 4: Scale factors for laser intensities.

Energy (mJ)	16	30	60	120	240	380
IR	0.70	1.09	0.86	1.15	1.69	1.21
Green	2.80	1.70	1.14	1.35	1.24	1.05

To show explicitly the nonlinear behavior of Compton scattering in intense laser fields, we present the scattered electron yield  $(1/N_\gamma)(dN/dP)$  at several scattered electron momenta (for  $P$  within  $\pm 0.25$  GeV/ $c$  of the central value), as a function of laser intensity  $I$  in Figs. 32 and 33 for circularly polarized IR and green laser pulses, respectively. The data sets, also given in Tables 7 and 8, are labelled by the lowest allowed number of laser photons corresponding to each scattered electron momentum, recalling Table 2. The expected dependence

Table 5: Nonlinearly scattered electron yield for circularly polarized IR laser.

$P$ (GeV/c)	$(1/N_\gamma)(dN/dP) \times 10^5 \text{ (GeV/c)}^{-1}$												
	$U_L = 16 \text{ mJ}$		$U_L = 30 \text{ mJ}$		$U_L = 60 \text{ mJ}$		$U_L = 120 \text{ mJ}$		$U_L = 240 \text{ mJ}$		$U_L = 380 \text{ mJ}$		
	$\eta = 0.066$		$\eta = 0.090$		$\eta = 0.128$		$\eta = 0.181$		$\eta = 0.256$		$\eta = 0.322$		
	D <sup>(a)</sup>	S <sup>(a)</sup>	D	S	D	S	D	S	D	S	D	S	
10.0											0.005 ± 0.05	0.00	
10.5											0.02 ± 0.06	0.01	
11.0											0.05 ± 0.03	0.02	
12.0								0.01 ± 0.05	0.003	0.08 ± 0.05	0.01	0.13 ± 0.05	0.08
12.5								0.02 ± 0.03	0.01	0.12 ± 0.07	0.05	0.26 ± 0.05	0.17
13.5								0.05 ± 0.05	0.03	0.53 ± 0.05	0.10	0.77 ± 0.05	0.53
14.0										0.86 ± 0.08	0.26		
14.5			0.05 ± 0.07	0.01	0.06 ± 0.07	0.03	0.09 ± 0.05	0.14		1.21 ± 0.07	0.61	2.30 ± 0.22	1.45
15.5			0.08 ± 0.07	0.03	0.06 ± 0.07	0.10	0.16 ± 0.08	0.42		2.79 ± 0.21	1.06	4.08 ± 0.37	4.26
16.0										3.62 ± 0.22	1.80		
16.5			0.29 ± 0.19	0.09	0.37 ± 0.21	0.20	1.27 ± 0.11	0.59	4.88 ± 0.28	2.07			
17.0			0.88 ± 0.39	0.27	0.73 ± 0.32	0.41							
17.5	1.05 ± 0.38	0.96	0.92 ± 0.32	1.29									
18.0	1.26 ± 0.28	1.21	3.24 ± 0.62	2.53	4.11 ± 0.78	3.40							
18.5			11.4 ± 2.64	6.87	13.7 ± 3.09	9.01							
19.0			11.3 ± 2.02	9.02	13.3 ± 2.35	13.0							
19.5			14.4 ± 2.65	10.8	14.2 ± 2.51	15.2							
20.0	3.97 ± 0.89	6.16	5.75 ± 1.04	9.71									
20.5	4.28 ± 0.62	5.52	9.68 ± 1.38	11.2	12.1 ± 1.68	14.9							
21.0			11.7 ± 0.92	11.5	11.8 ± 0.89	15.1							

(a) D is the data including errors, S is the simulation.

Table 6: Nonlinearly scattered electron yield for circularly polarized green laser.

$P$ (GeV/c)	$(1/N_\gamma)(dN/dP) \times 10^5 \text{ (GeV/c)}^{-1}$									
	$U_L = 16 \text{ mJ}$		$U_L = 30 \text{ mJ}$		$U_L = 60 \text{ mJ}$		$U_L = 120 \text{ mJ}$		$U_L = 240 \text{ mJ}$	
	$\eta = 0.047$		$\eta = 0.064$		$\eta = 0.090$		$\eta = 0.128$		$\eta = 0.181$	
	D <sup>(a)</sup>	S <sup>(a)</sup>	D	S	D	S	D	S	D	S
8.0										
8.5							0.16 ± 0.06	0.04	0.04 ± 0.07	0.01
9.0					0.19 ± 0.11	0.03	0.24 ± 0.14	0.08	0.22 ± 0.07	0.15
9.5					0.14 ± 0.24	0.08	0.39 ± 0.19	0.14	0.25 ± 0.09	0.22
10.0			0.24 ± 0.27	0.01			0.21 ± 0.32	0.16	0.26 ± 0.23	0.37
10.5			0.51 ± 0.23	0.03	0.73 ± 0.40	0.04	2.87 ± 0.96	0.80	0.45 ± 0.33	0.50
11.0	1.11 ± 0.42	0.29	2.15 ± 0.57	0.75	3.68 ± 0.88	1.53	7.00 ± 1.66	2.57	3.74 ± 1.05	1.52
11.5			4.87 ± 1.22	1.96	5.36 ± 1.56	2.18			9.22 ± 2.02	4.52
12.0			8.13 ± 1.98	3.74	7.31 ± 2.21	4.19				
12.5	3.93 ± 1.41	1.90	6.89 ± 1.77	4.75	12.1 ± 2.37	9.71	20.9 ± 3.67	16.6		
13.0			9.28 ± 1.70	5.22	10.1 ± 2.17	6.44				
13.5			10.7 ± 1.74	5.83	12.3 ± 2.27	6.51				
14.0	5.18 ± 5.09	2.52	8.84 ± 1.37	6.43	10.5 ± 1.55	13.4	25.3 ± 3.55	23.5		
14.5	7.33 ± 2.29	2.54								

(a) D is the data including errors and S in the simulation.

on the laser intensity is

$$\frac{1}{N_\gamma} \frac{dN}{dP} \propto \eta^{2(n-1)} \propto I^{n-1}, \quad (76)$$

as indicated by the shaded bands in the figures, which are the predictions of the simulation including the uncertainty in the laser intensity. Note that while the rate as normalized by the factor  $1/N_\gamma$  would be independent of intensity for a linear process, the uncertainty in laser intensity still has a large effect on our expectations for higher-order processes.

Results of fits to the form (76) are presented in Table 9. The fits for  $n = 2$  are quite satisfactory, and acceptable for  $n = 3$  IR. For  $n = 4$  IR and  $n = 3$  green, the errors on the data preclude a meaningful fit. A more sensitive demonstration of the power-law dependence on the laser intensity is provided by the positron data (sec. 6), which is an  $n = 5$  process and is practically free of background at high values of  $\eta$ .

Table 7: Scattered electron yield *vs.* IR laser intensity.

$I \times 10^{-16}$ (W/cm <sup>2</sup> )	$(1/N_\gamma)(dN/dP) \times 10^5 \text{ (GeV/c)}^{-1}$			
	$P = 20.5 \text{ GeV/c}$	$P = 18.0 \text{ GeV/c}$	$P = 16.5 \text{ GeV/c}$	$P = 12.5 \text{ GeV/c}$
1.04	$3.92 \pm 0.57$	$1.12 \pm 0.26$		
1.29	$6.08 \pm 0.93$	$1.93 \pm 0.43$		
1.61	$7.81 \pm 1.16$	$2.58 \pm 0.52$		
2.00	$8.93 \pm 1.29$	$2.95 \pm 0.58$	$0.25 \pm 0.18$	
2.46	$11.80 \pm 1.72$	$3.77 \pm 0.75$	$0.32 \pm 0.19$	
3.00	$11.64 \pm 1.62$	$3.71 \pm 0.71$	$0.32 \pm 0.20$	
3.64	$14.89 \pm 2.11$	$5.37 \pm 1.13$	$0.40 \pm 0.21$	
4.43	$16.30 \pm 2.39$	$6.12 \pm 1.32$	$0.34 \pm 0.21$	
5.43		$6.80 \pm 1.46$	$0.59 \pm 0.12$	
6.71			$0.91 \pm 0.10$	
8.36			$1.36 \pm 0.12$	
10.36			$1.93 \pm 0.19$	
12.86			$4.06 \pm 0.34$	$0.06 \pm 0.05$
15.72			$4.79 \pm 0.30$	$0.10 \pm 0.07$
18.93			$4.94 \pm 0.29$	$0.12 \pm 0.06$
23.22			$5.27 \pm 0.73$	$0.20 \pm 0.05$
28.57				$0.28 \pm 0.05$

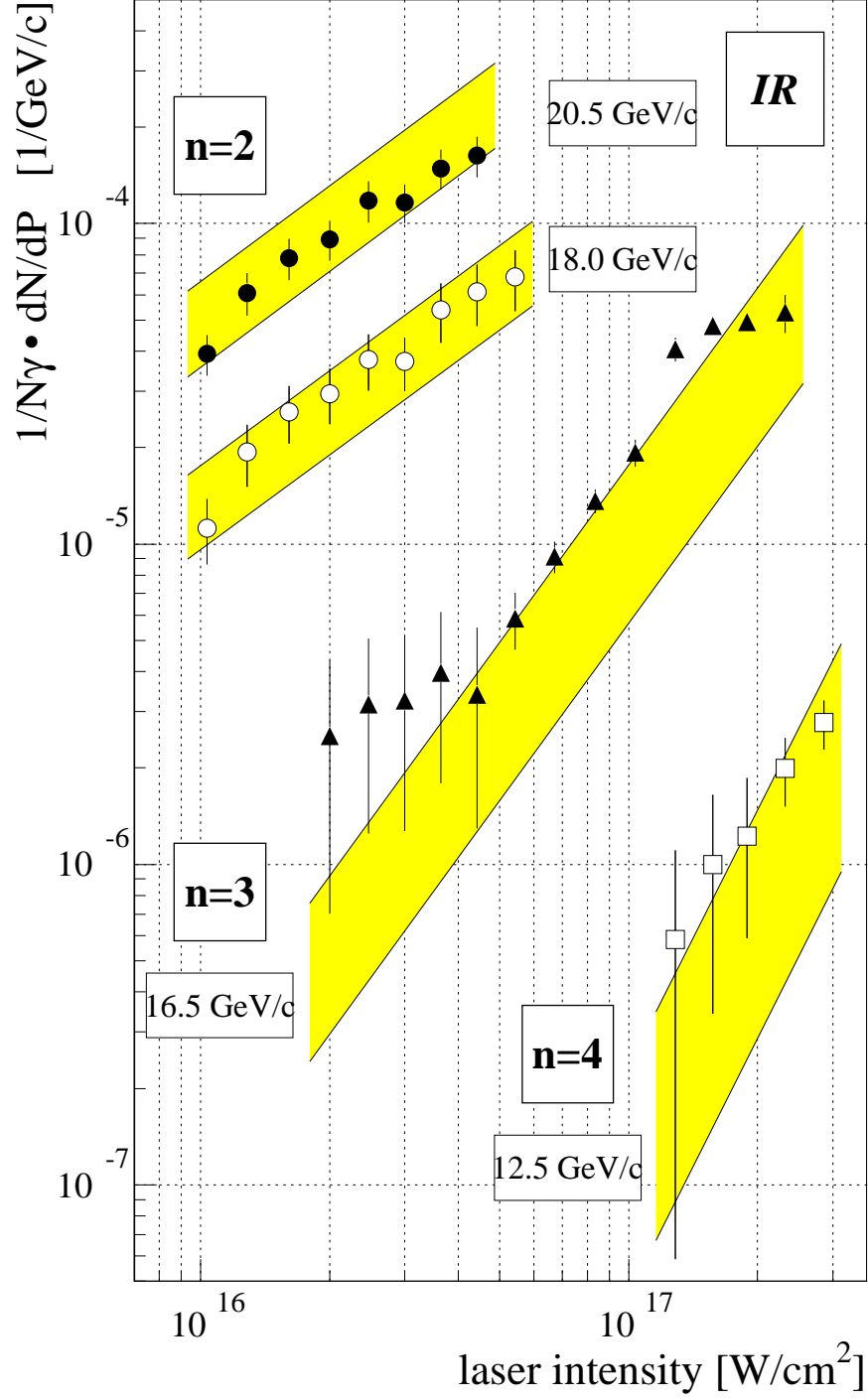


Figure 32: The scattered electron yield,  $(1/N_\gamma)(dN/dP)$ , vs. IR laser intensity for four representative electron momenta. The solid and open circles are data for momenta at which the  $n = 2$  Compton process dominate. The triangles and open squares are data for momenta at which the  $n = 3$  and  $n = 4$  processes dominate, respectively. The simulation for each data set is shown as bands representing the 30% uncertainty in the IR laser intensity. The slopes of the bands are characteristic of the order of the nonlinear process.

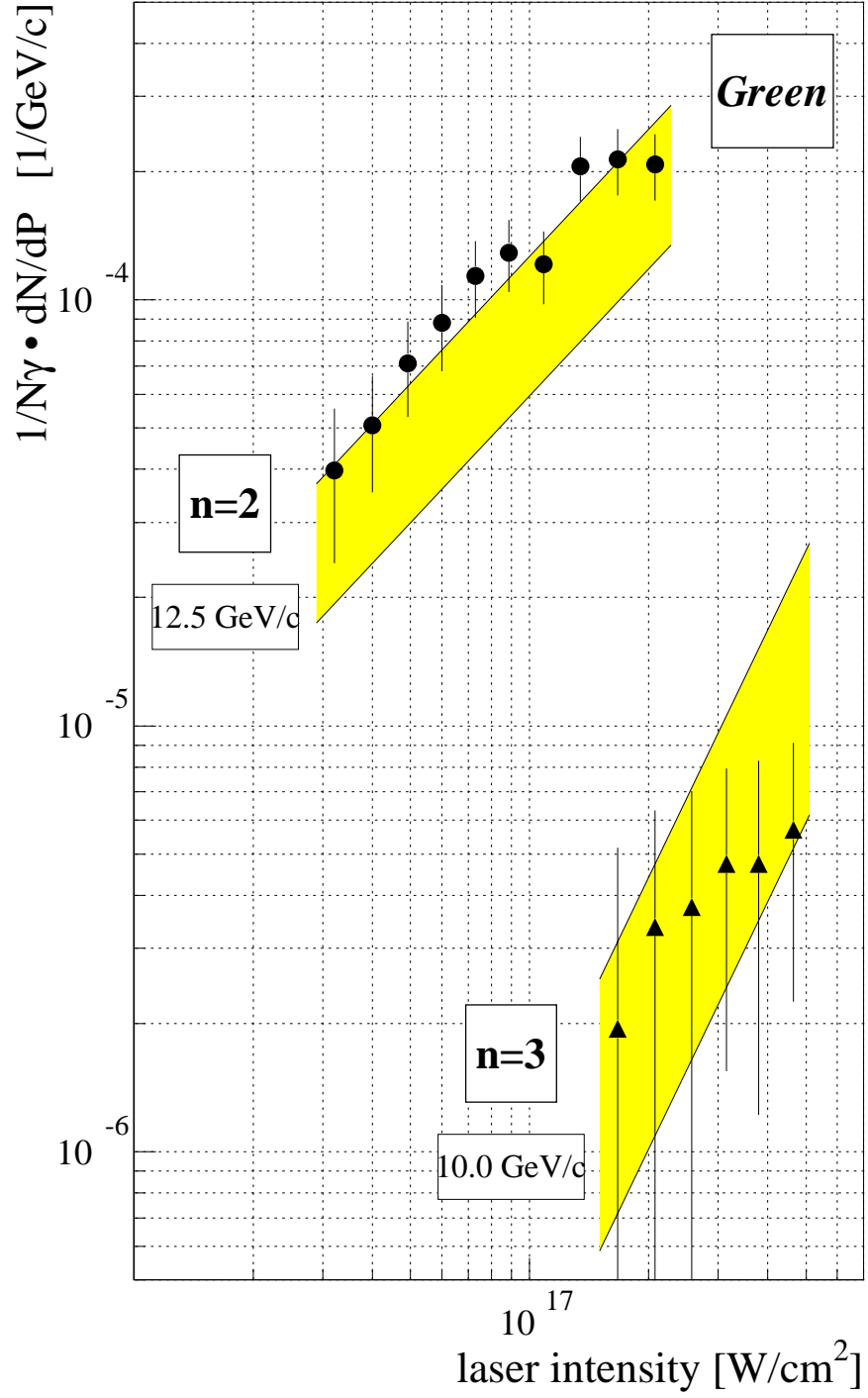


Figure 33: The scattered electron yield,  $(1/N_\gamma)(dN/dP)$ , vs. green laser intensity for two representative electron momenta. The solid circles and triangle are data for which the  $n = 2$  and  $n = 3$  nonlinear Compton processes dominate, respectively. The simulation for each data set is shown as bands, including the  $^{+50\%}_{-30\%}$  uncertainty in the laser intensity.



Table 8: Scattered electron yield *vs.* green laser intensity.

$I \times 10^{-16}$ (W/cm <sup>2</sup> )	$(1/N_\gamma)(dN/dP) \times 10^5$ (GeV/c) <sup>-1</sup>	
	$P = 12.5$ GeV/c	$P = 10.0$ GeV/c
3.22	$3.98 \pm 1.57$	
4.00	$5.07 \pm 1.53$	
4.93	$7.10 \pm 1.80$	
6.00	$8.82 \pm 2.02$	
7.29	$11.39 \pm 2.33$	
8.86	$12.91 \pm 2.49$	
10.86	$12.12 \pm 2.37$	
13.43	$20.57 \pm 3.55$	
16.72	$21.36 \pm 3.76$	$0.19 \pm 0.32$
20.72	$20.77 \pm 3.70$	$0.34 \pm 0.30$
25.72		$0.38 \pm 0.33$
31.44		$0.47 \pm 0.32$
37.87		$0.47 \pm 0.35$
46.44		$0.57 \pm 0.34$

Table 9: Power law fits,  $(1/N_\gamma)(dN/dP) \sim I^b$  for nonlinear Compton data. For order  $n$  scattering, the expectation is that  $b = n - 1$ .

$P$ (GeV/c)	$n$	$b$	$\chi^2/\text{dof}$
IR:			
20.5	2	$0.93 \pm 0.10$	0.62
18.0	2	$1.01 \pm 0.13$	0.43
16.5	3	$1.59 \pm 0.18$	3.09
12.5	4	$1.84 \pm 0.64$	0.03
Green:			
12.5	2	$0.86 \pm 0.15$	0.51
10.0	3	$0.81 \pm 1.45$	0.02

## 5.2 Scattered Electron Spectra from ECAL Scans

Scattered electron spectra were also collected with linearly polarized green light during positron production running. Only the top row of the ECAL was used in the analysis, to reduce systematic effects, and the spectra were obtained by scanning the detector position over the available momentum range. The shielding of the ECAL was modified as discussed in sec. 3.3, and resulted in a tenfold decrease in background. The laser intensity was measured indirectly by relying on the linear and nonlinear monitors, as discussed in sec. 4.2.2.

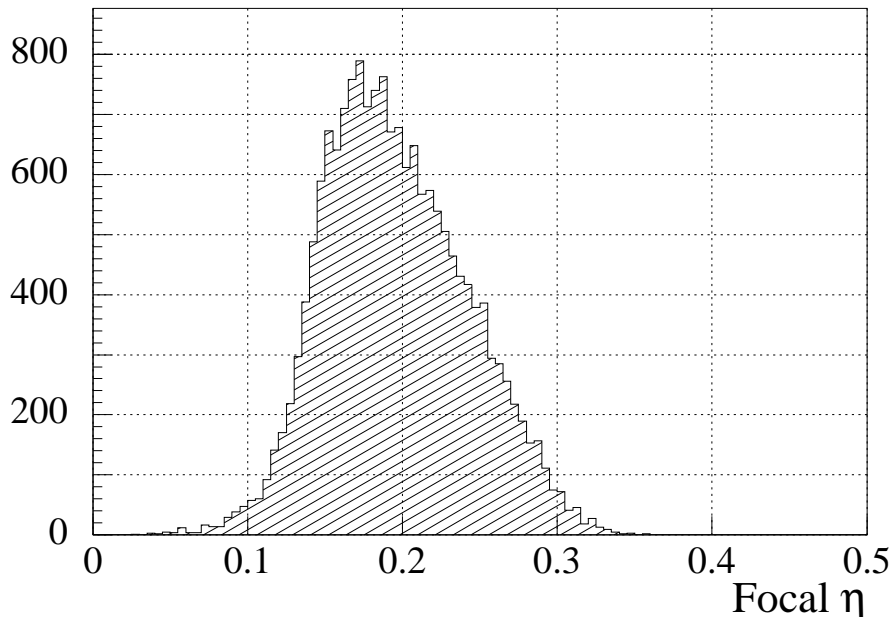


Figure 34: Distribution of the laser field-strength parameter  $\eta$  calculated using the constrained fit (67) for the 46.6 GeV data with linearly polarized green light.

The laser was operated at fixed nominal energy, resulting in the measured distribution of the field-strength parameter  $\eta$  as shown in Fig. 34. There was sufficient data to be binned in six intervals of  $\eta$  from 0.15 to 0.25, as shown in Fig. 35 with the data as the black dots and the simulation as the open circles. The modification to the beam pipe restricted the ECAL to observe electrons scattered by  $n = 3$  or more photons.

The data are in excellent agreement with the simulation except at the highest momentum, which is at the inflection between  $n = 2$  and  $n = 3$  scattering. The  $n = 3$  “shoulder” from 8 to 10 GeV/ $c$  can be seen for low values of  $\eta$ , at which it is expected to be more apparent. Furthermore, the good agreement between data and simulation is an indication that the values of  $\eta$  deduced by the indirect method from nonlinear monitors are reliable, within their uncertainty of  $\pm 10\%$ .

For more information on ECAL scan data, both at 46.6- and 49.1-GeV incident electron energy, see ref. [39].

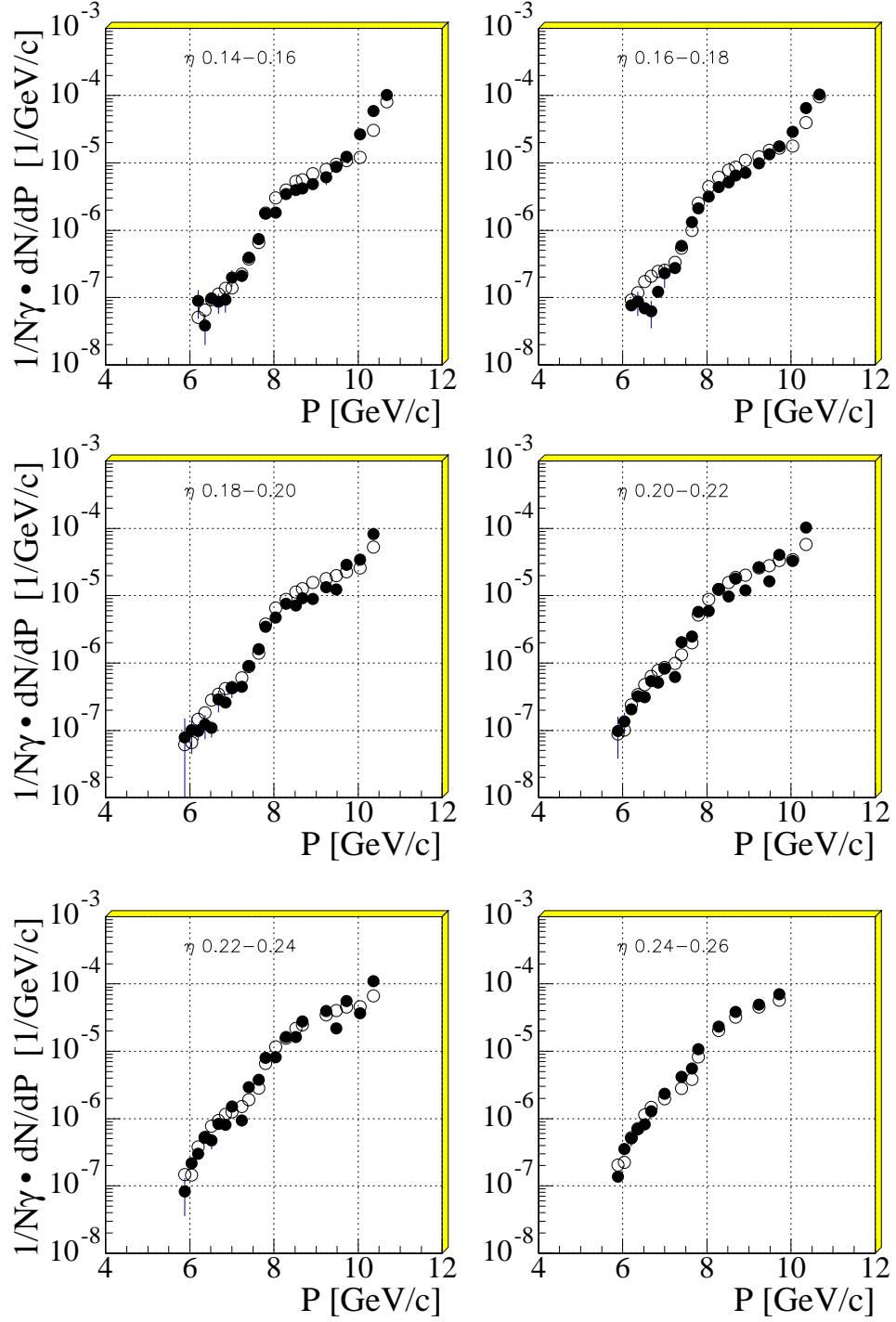


Figure 35: The scattered electron yield  $(1/N_\gamma)(dN/dP)$ , as a function of electron momentum, for 46.6-GeV incident electrons and linearly polarized green laser. The solid dots are the data, and the open circles are the prediction of the simulation. Data are shown for six intervals of the laser field-strength parameter  $\eta$ .

### 5.3 Forward Photons

An important part of the nonlinear Compton scattering study is the spectrum of forward photons, since the competing process of plural Compton scattering cannot yield photons with energies beyond the  $n = 1$  kinematic edge.

At high laser intensities, there were typically  $N_\gamma \sim 10^7$  photons scattered into the forward direction, with only  $\sim 1\%$  of these at momenta beyond the  $n = 1$  Compton edge. A  $50\text{-}\mu\text{m}$ -thick aluminum foil was used as a converter ( $5.6 \times 10^{-4}$  radiation length), so that  $\sim 5,000$  pairs entered the pair spectrometer (Fig. 19) in each laser pulse. This high number made proper identification of the positron partner of a given electron impossible. Therefore, we analyzed the data in the two arms of the spectrometer independently, and then combined the reconstructed single-particle momentum spectra for comparison to a model spectrum calculated by convolving the simulated photon spectrum with the Bethe-Heitler pair spectrum.

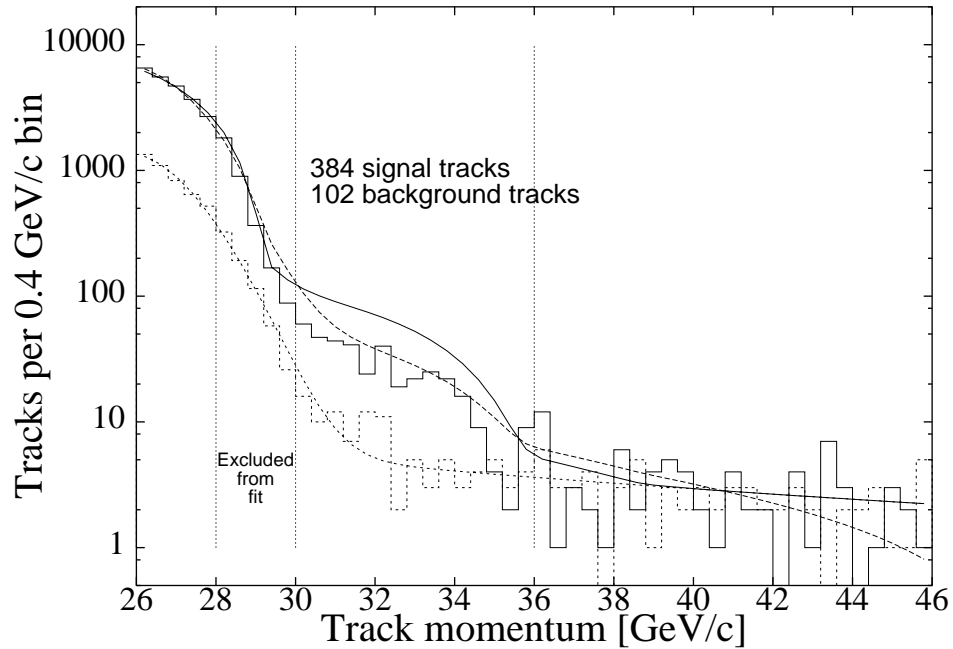


Figure 36: The momentum spectrum of electrons and positrons from conversion of forward photons into pairs (solid histogram), and the background as estimated from sidebands (dotted histogram). The dotted curve is a fit to the background. The solid and dashed curves are simulations, including the fitted background, in which the value of  $\eta$  is taken from the indirect method, or fit to the present data, respectively.

In Fig. 36 we show the spectrum for all tracks with momentum  $P > 26.0$  GeV/ $c$  in either arm, for  $\sim 2,300$  linearly polarized green laser pulses that collided with the 46.6 GeV electron beam. The solid histogram represents the candidate signal tracks, while the dotted histogram shows the level of background tracks deduced from sidebands, as discussed in sec. 4.4. The  $n = 1$  kinematic edge at 29 GeV/ $c$  is clearly observed. The  $n = 2$  kinematic

edge is at 36 GeV/ $c$  and, as predicted by the simulation, no tracks above background are observed beyond this momentum.

The solid curve is a simulation, including the fitted background (dotted curve), that is normalized to the number of tracks for  $P < 28$  GeV/ $c$  using the value of  $\eta_e$ , determined by the indirect method discussed in sec. 4.4. The dashed curve is a simulation, in which  $\eta$  has been adjusted for best fit to the forward photon data, yielding a value called  $\eta_\gamma$ .

For a more detailed study, we separated the data into five intervals of the laser field-strength parameter  $\eta_e$ , as shown in Fig. 37, where the solid and the dashed lines are fits to the signal and to the background, respectively. The number of (signal–background) tracks for  $26 < P < 29$  GeV/ $c$  (the  $n = 1$  region) and for  $P > 30$  GeV/ $c$  (the  $n = 2$  region) are presented in Table 10.

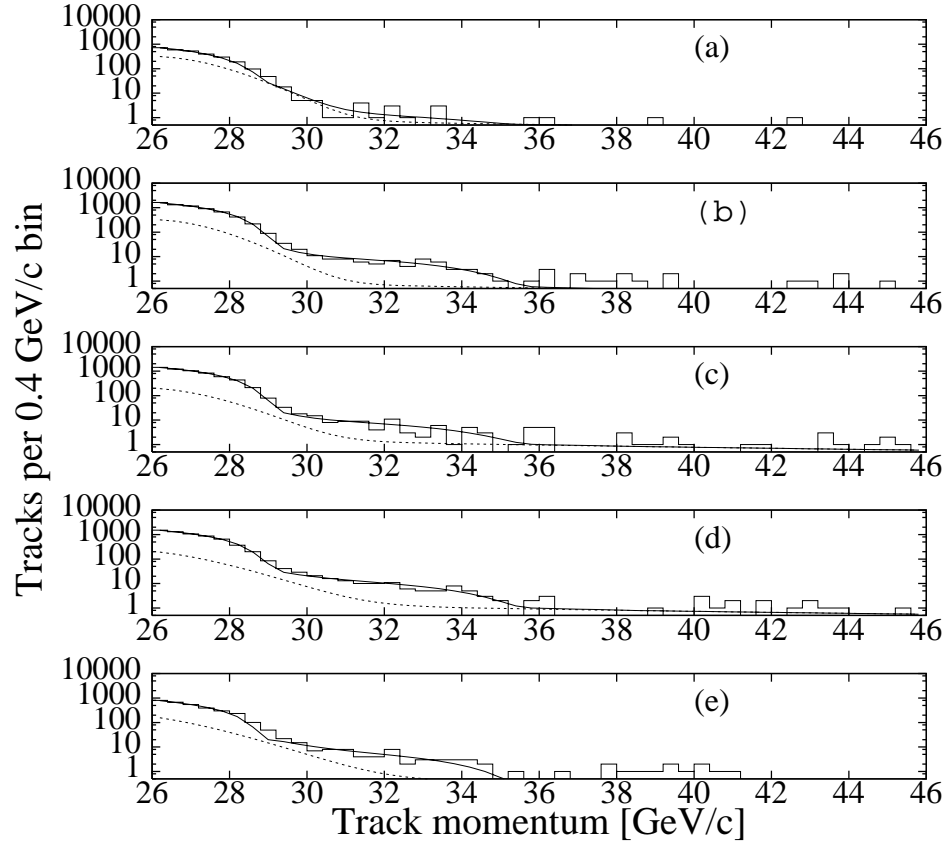


Figure 37: Single-particle momentum spectra from five subsets of the photon-conversion data.

From a fit to each data set, we extracted the values of  $\eta_\gamma$  given in Table 11. These values of  $\eta_\gamma$  are compared with the corresponding  $\eta_e$  in Fig. 38. For all data sets,  $\eta_\gamma$  is lower than  $\eta_e$ , and a linear fit gives  $\eta_\gamma = 0.74\eta_e$ , as compared to the expected value of one. Since the uncertainty in the laser intensity (sec. 4.2) is  $\pm 11\%$ (stat.) $^{+8}_{-13}\%$ (syst.), the apparent discrepancy is within one standard deviation of the overall (statistical plus systematic) error.

The good fit to the data shown in Fig. 37 supports the validity of the model of nonlinear

Table 10: Yields of tracks in the CCD pair spectrometer after background subtraction, for the five subsets shown in Fig. 37.

Subset	$\eta_e$	No. of Tracks	
		$n = 2$	$n = 1$
a	0.13 – 0.16	–3	1669
b	0.16 – 0.20	74	5612
c	0.20 – 0.235	70	5425
d	0.235 – 0.27	100	5752
e	0.27 – 0.31	49	2524

Compton scattering in sec. 2. The data clearly indicate the presence of forward photons with momenta beyond the  $n = 1$  kinematic edge, which is evidence for nonlinear Compton scattering, (1), independent of any plural scattering (38) in the laser focus.

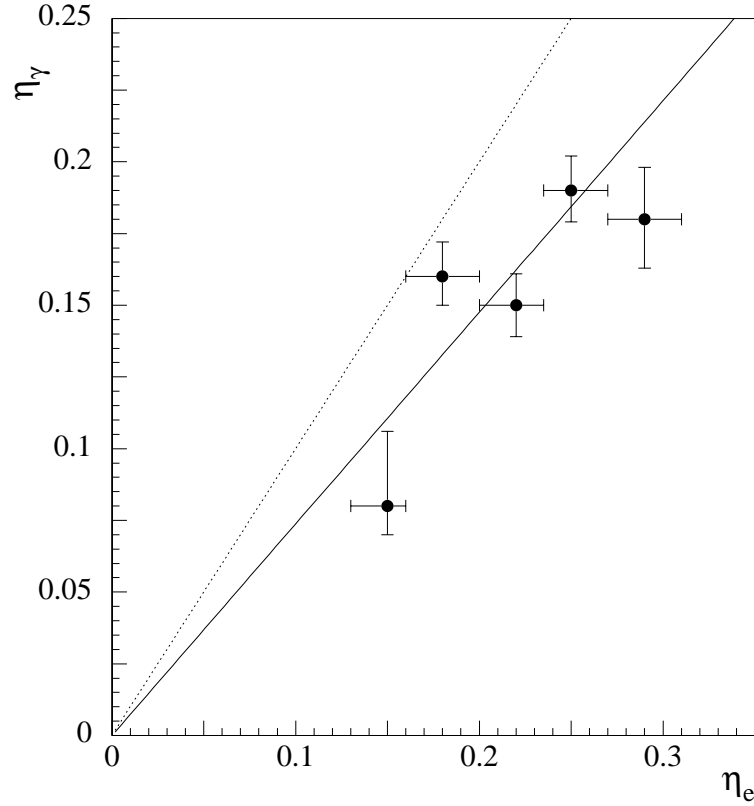


Figure 38: Photon-based  $\eta_\gamma$  vs. the mean value of the nonlinear-electron-based  $\eta_e$  for each of the five CCD data subsets. The vertical error bars are from the fit for  $\eta_\gamma$  using CCD data, and the horizontal error bars are the rms of the distribution of the monitor  $\eta_e$ .

Table 11: Fitted and Estimated Values of  $\eta$ .

$\eta_e$	$U_{\text{laser}}$ (mJ)	$\eta_\gamma$	$\chi^2/\text{dof}$
0.13 – 0.16	325	$0.08 \pm 0.02$	33/44
0.16 – 0.20	400	$0.16 \pm 0.01$	58/42
0.20 – 0.235	475	$0.15 \pm 0.01$	77/42
0.235 – 0.27	550	$0.19 \pm 0.01$	40/42
0.27 – 0.31	625	$0.18 \pm 0.02$	57/42

For more details on the forward photon data, see [67].

## 6 Results on Pair Production

### 6.1 Light-by-Light Scattering

Positron data were collected with linearly polarized green laser pulses of nominal energy of 500 mJ with 46.6-GeV incident electrons. A smaller sample of data was collected with 49.1-GeV electrons. Since pair production for our experiment involves at least five laser photons (one or more to produce a high-energy photon via reaction (1), and four or more to produce a pair via reaction (2)), it depends strongly on the peak laser intensities and on the beam overlap. Data from collisions with poor  $e$ -laser beam overlap were discarded when the signal in the EC37 monitor was less than 1/3 of the value expected for optimal overlap.

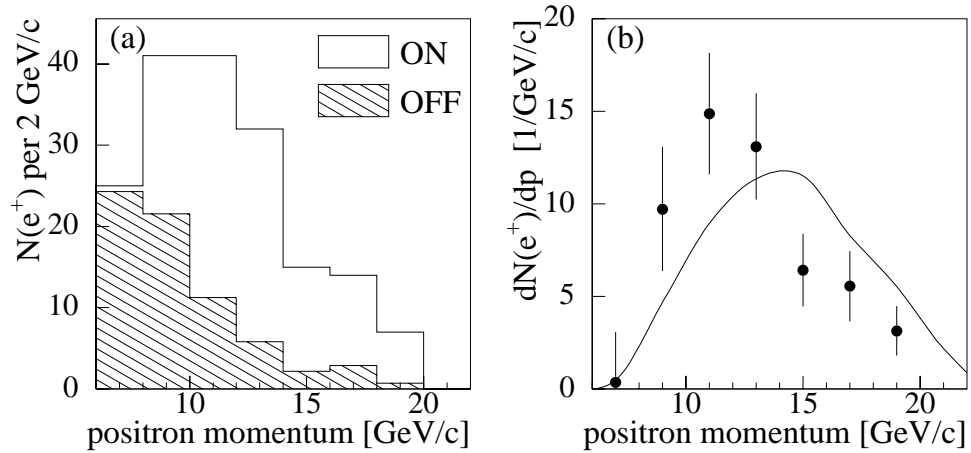


Figure 39: Number of positron candidates *vs.* momentum for laser-on (ON) and laser-off (OFF) electron pulses. (b) Spectrum of signal positrons obtained by subtracting the laser-off from the laser-on distribution. The curve shows the expected momentum spectrum from the model calculation.

Table 12: The 46.6 GeV positron events in 2 GeV/ $c$  bins, for  $\eta \geq 0$ . The number of laser-off positrons have been scaled by the ratio 0.17 of the number of laser-on to laser-off electron pulses.

$P$ (GeV/ $c$ )	$N_e^+$ (ON)	$N_e^+$ (OFF)	$dN/dP$ (GeV/ $c$ ) $^{-1}$
7	25	24.3	$0.4 \pm 2.7$
9	41	21.6	$9.7 \pm 3.3$
11	41	11.2	$14.9 \pm 3.3$
13	32	5.8	$13.1 \pm 2.9$
15	15	2.2	$6.4 \pm 2.0$
17	14	2.9	$5.6 \pm 1.9$
19	7	0.7	$3.1 \pm 1.3$

After cuts there were  $\sim 22,000$  laser-on electron pulses, in which 175 positrons were identified. The cluster momentum distribution for these events is shown in Fig. 39(a), and summarized in Table 12. We also took  $\sim 121,000$  laser-off electron pulses in which 379 positrons were identified. These were largely due to showers of lost beam electrons that struck beamline components. The momentum distribution of these background positrons, normalized by the ratio 0.17 of ON/OFF electron pulses, is shown by the shaded area in Fig. 39(a). By subtracting the two distributions, we obtained the momentum spectrum for the signal as shown in (b) of the figure; it contains  $106 \pm 14$  positrons. The solid curve is the prediction of the simulation described in appendix A and based on the theory reviewed in sec. 2.4.

Figure 40 and Table 13 show the yield  $R_{e^+}$  of positrons per laser shot as a function of the laser intensity parameter  $\eta$ , where the latter was measured by the indirect method described in sec. 4.2.2. The line is a power law fit to the data and gives  $R_{e^+} \propto \eta^{2n}$  with  $n = 5.1 \pm 0.2$  (stat.)  $^{+0.5}_{-0.8}$  (syst.), where the statistical error is from the fit and the systematic error includes the effects discussed previously, as well as the effect of the choice of bin size in  $\eta$ . Thus, the observed positron production rate is highly nonlinear, varying as the 5<sup>th</sup> power of the laser intensity (since  $I \propto \eta^2$ ). This is in good agreement with the fact that the rate of multiphoton reactions involving  $n$  laser photons is proportional to  $\eta^{2n}$  (for  $\eta^2 \ll 1$ ), and with the kinematic requirement that 5 laser photons are needed to produce a pair near threshold.

The detailed simulation indicates that on average 1.5 photons are absorbed from the laser field in reaction (1) and 4.7 in (2), but that the exponent  $n$  for the two-step process varies slightly with  $\eta$  and has an average value of 5.3. The calculated distribution of the number of photons absorbed from the field in the Breit-Wheeler process (2) for our experimental arrangement and  $\eta = 0.4$  at the laser focus is shown in Fig. 41. That value of  $\eta$  corresponds to  $\Upsilon_\gamma = 0.2$ , where the latter is the invariant ratio of the laser field strength to the QED critical field strength introduced in sec. 1.3.

The observed positron rate is shown in Fig. 42, after having been normalized to the



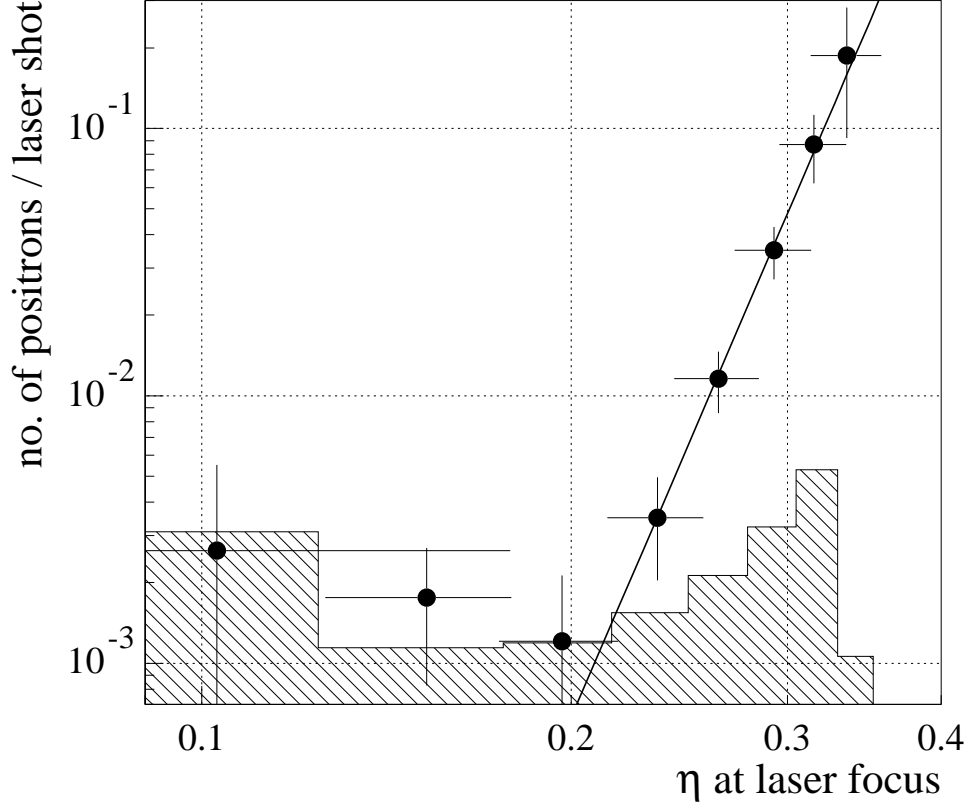


Figure 40: The dependence of the positron rate per laser shot on the laser field-strength parameter  $\eta$ . The line shows a power law fit to the data. The shaded distribution is the 95% confidence limit on the residual background from showers of lost beam particles after subtracting the laser-off positron rate.

Table 13: The 46.6 GeV positron yield *vs.*  $\eta$ .

$\eta$	$N_e^+/\text{shot} \times 10^{-3}$	$N_e^+/N_\gamma \times 10^{-10}$
$0.10 \pm 0.07$	$2.6 \pm 2.9$	$9.5 \pm 10.4$
$0.15 \pm 0.03$	$1.8 \pm 0.9$	$3.2 \pm 1.7$
$0.20 \pm 0.02$	$1.2 \pm 0.9$	$1.9 \pm 1.5$
$0.23 \pm 0.02$	$3.5 \pm 1.5$	$5.4 \pm 2.2$
$0.26 \pm 0.02$	$11.6 \pm 3.0$	$16.8 \pm 4.4$
$0.29 \pm 0.02$	$35 \pm 8$	$48 \pm 11$
$0.32 \pm 0.02$	$87 \pm 25$	$113 \pm 32$
$0.34 \pm 0.02$	$187 \pm 95$	$273 \pm 139$

number of Compton photons, where the latter was inferred from the rate in the EC37 monitor. This procedure minimized the effect of the uncertainty in the laser focal volume and in the  $e$ -laser overlap. The simulation indicates that the variation of the positron rate

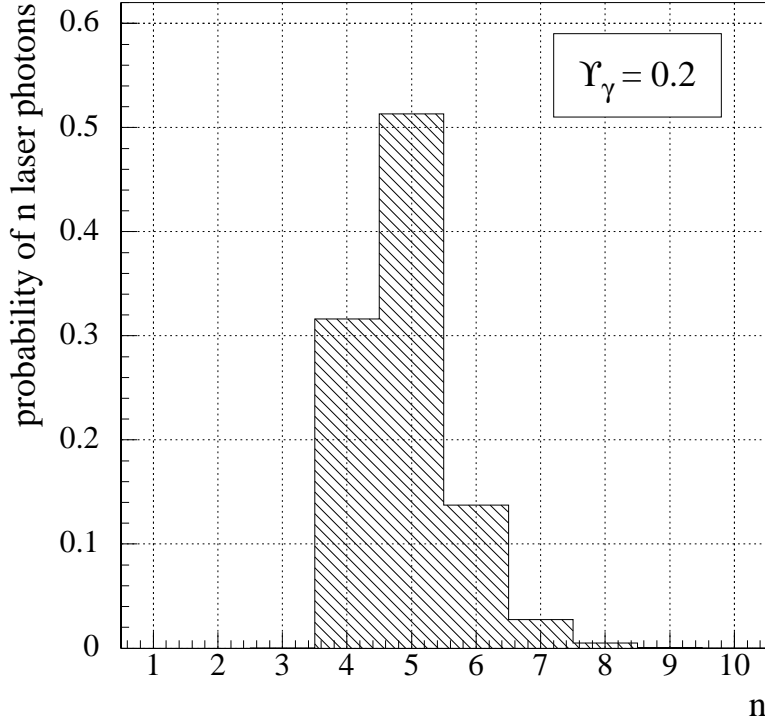


Figure 41: Calculated probability distribution of the number  $n$  of photons absorbed from the laser field in the second step of the two-step Breit-Wheeler pair creation process. Field intensity corresponding to  $\Upsilon_\gamma = 0.2$  ( $\eta = 0.4$ ) at the laser focus was used for the simulation.

over a spatial offset of  $\pm 25 \mu\text{m}$  or a temporal offset of  $\pm 5 \text{ ps}$  between the electron and laser beams is  $0.88 \pm 0.07$  of the variation in the Compton scattering rate, and we adopt this value as the correction factor for imperfect overlap. The solid curve in Fig. 42 shows the prediction per Compton photon based on the numerical integration of the two-step Breit-Wheeler process, (1) followed by (2), multiplied by the cluster-finding efficiency (0.93), and by the overlap correction factor (0.88). The data are in good agreement with the simulation, both in magnitude of the observed rate and in its dependence on  $\eta$ .

Several points at low values of  $\eta$  seen in Figs. 40 and 42, while statistically consistent with reactions (1) and (2), indicate a possible residual background of about  $2 \times 10^{-3}$  positrons/laser shot, likely due to fluctuations in the subtraction of positrons from showers of lost beam electrons. The residual background could also be due to positrons produced by the interaction of Compton photons with the residual gas in the beam line. We can estimate an upper limit to this effect from the rate of positrons with the laser off, ( $6 \times 10^{-3} e^+$  per beam electron), supposing they are all due to interactions of beam electrons with residual gas, rather than due to showers of lost beam electrons. This gives  $R_{e^+} < 10^{-10}$  per Compton photon, which is well below the observed rate shown in Fig. 42.

Positrons could also be produced through the emission and rescattering of a virtual photon as indicated by the trident process (53). To estimate the contribution of this process, we performed a simulation in which the beam electron emitted a virtual photon according to the

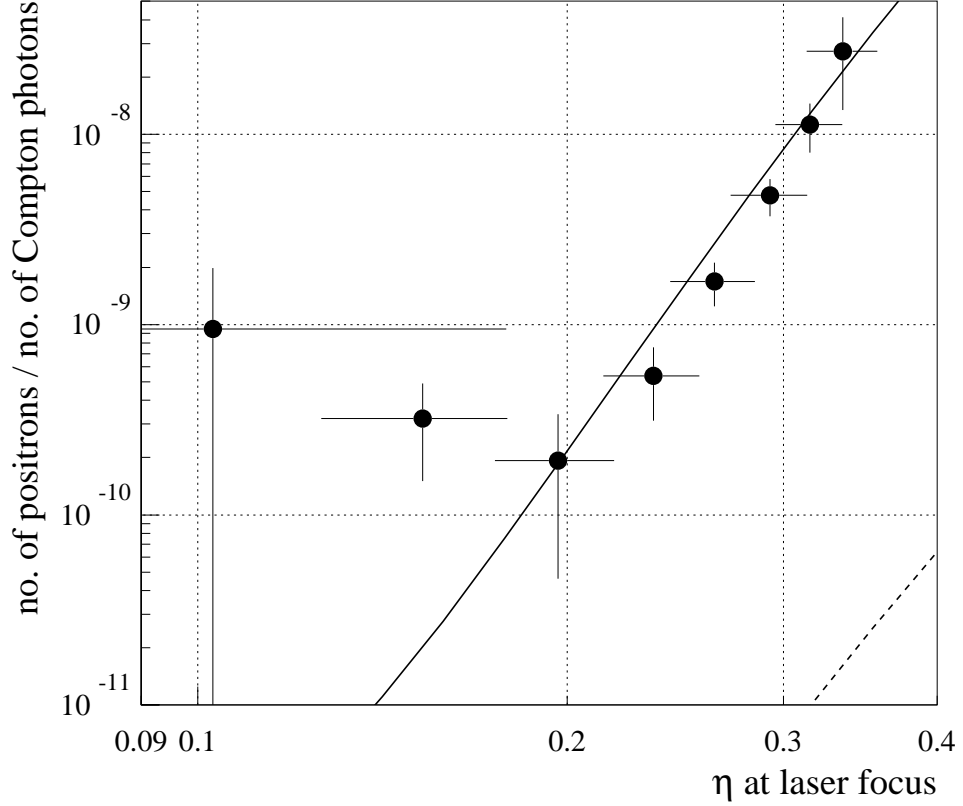


Figure 42: The dependence of the positron rate on the laser field-strength parameter  $\eta$  when the rate is divided by the number of Compton scatters inferred from the EC37 monitor. The solid line is the prediction per Compton photon based the simulation of the two-step Breit-Wheeler process, (1) followed by (2). The dashed line represents the simulation for the one-step trident process (53).

Weizsäcker-Williams approximation, and the virtual photon combined with laser photons to yield electron-positron pairs according to the theory of the multiphoton Breit-Wheeler process (2), as discussed in sec. 2.5. The results of this simulation are shown by the dashed curve in Fig. 42, and indicate that for the present experiment the trident process was negligible. See also Fig. 10 and [28, 68, 69].

Results from a similar analysis of the 49.1 GeV data sample ( $\sim 5000$  laser shots) are shown in Fig. 43, and summarized in Table 14. In this case, the errors on the data points are larger than those for the 46.6 GeV sample because of higher background, lower laser intensity, and a smaller number of events. There are  $22 \pm 10$  positrons above the background. The expected dependence on the laser intensity is obeyed and a power law fit of the form  $R_{e^+} \propto \eta^{2n}$  gives  $n = 3.2 \pm 0.9(\text{stat.})^{+0.7}_{-3.1}(\text{syst.})$ . These data are compared to the prediction of the simulation in Fig. 44.

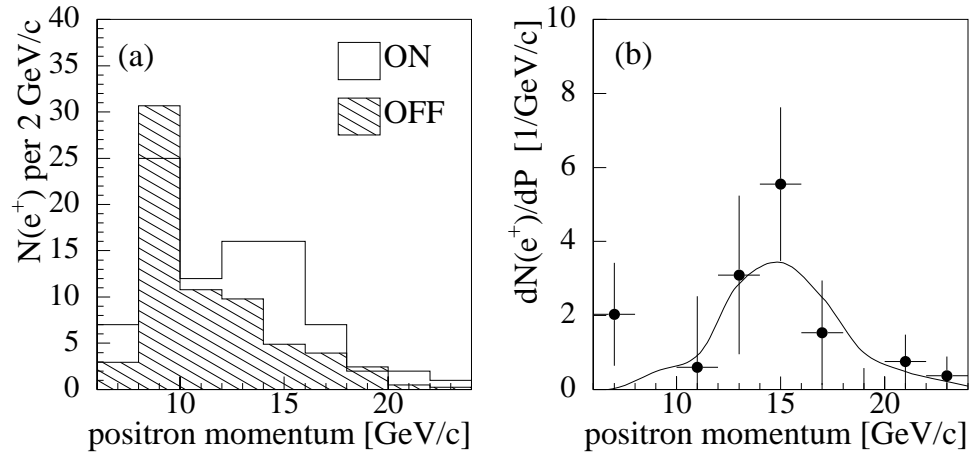


Figure 43: Momentum spectra for the positrons produced by 49.1 GeV electrons, with and without collisions with green laser photons. (a) The momentum spectra of the laser ON and the laser OFF clusters, the latter scaled by the ratio of number of laser ON to laser OFF pulses. (b) The momentum spectrum of the background subtracted positrons. The solid line is the prediction of a simulation of the experiment.

Table 14: The 49.1 GeV positron events in 2 GeV/ $c$  bins, for  $\eta \geq 0$ .

$P$ (GeV/ $c$ )	$N_e^+$ (ON)	$N_e^+$ (OFF)	$dN/dP$ (GeV/ $c$ ) <sup>-1</sup>
7	7	2.9	$2.0 \pm 1.4$
9	25	30.6	$-2.8 \pm 2.8$
11	12	10.8	$0.6 \pm 1.9$
13	16	9.8	$3.1 \pm 2.1$
15	16	4.9	$5.5 \pm 2.1$
17	7	3.9	$1.5 \pm 1.4$
19	2	2.4	$-0.2 \pm 0.8$
21	2	0.5	$0.8 \pm 0.7$
23	1	0.2	$0.4 \pm 0.5$

Table 15: The 49.1 GeV positron yield *vs.*  $\eta$ .

$\eta$	$N_e^+/\text{shot} \times 10^{-3}$	$N_e^+/N_\gamma \times 10^{-10}$
$0.16 \pm 0.02$	$-0.8 \pm 5.4$	$-2.1 \pm 14.4$
$0.20 \pm 0.02$	$1.0 \pm 2.6$	$2.4 \pm 6.1$
$0.23 \pm 0.02$	$8.4 \pm 3.5$	$19.5 \pm 8.0$
$0.27 \pm 0.02$	$13.9 \pm 8.1$	$31.6 \pm 18.4$

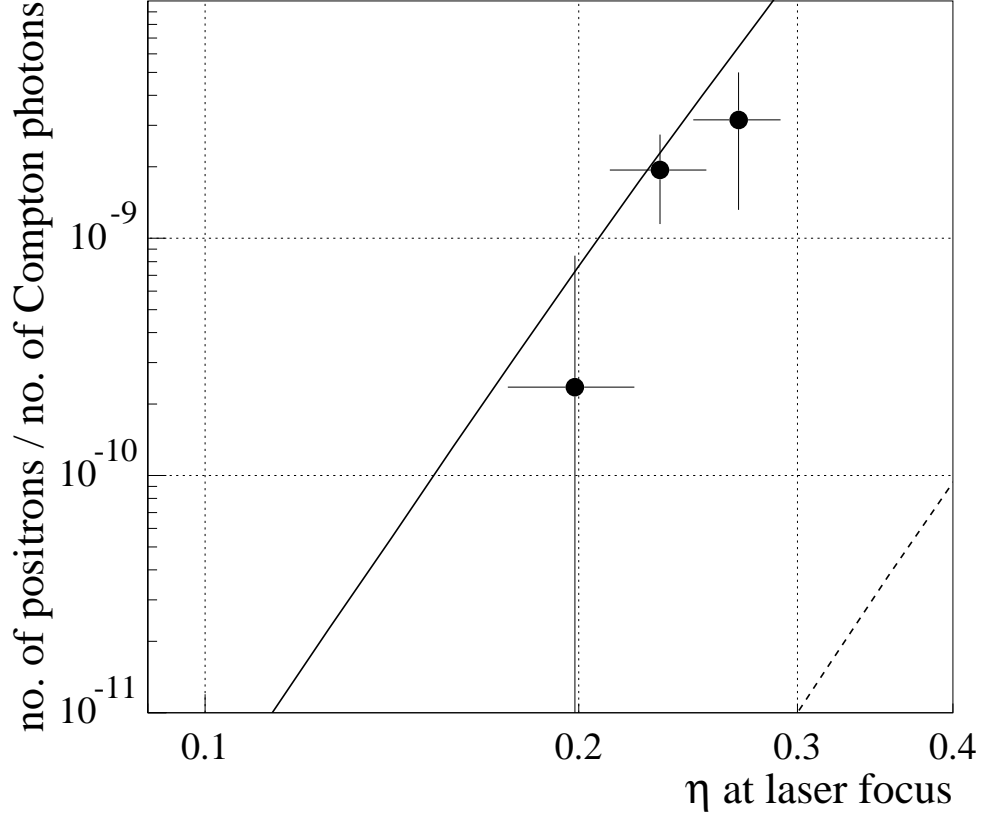


Figure 44: The subtracted laser-on positron rate for 49.1 GeV beam electrons, normalized to the number of the linear Compton photons. The prediction of the simulation is represented by the solid line. The dashed line indicates the results of the simulation of the trident process.

## 6.2 Breakdown of the Vacuum

In the previous section, the data have been interpreted as multiphoton light-by-light scattering, (2). As discussed in sec. 2.4, for large numbers of absorbed laser photons, it becomes valid to interpret the data in terms of production of  $e^+e^-$  pairs by the intense electric field of the laser pulse, in which the initial nonlaser photon plays only a minor role. Figure 41 indicates that typically five laser photons were involved in pair creation in our experiment, so we are nearly in the large- $n$  limit where the form (48) holds.

Therefore, we plot the positron yield as a function of  $1/\Upsilon_\gamma$  in Fig. 45, including both the 46.6 GeV and the 49.1 GeV data. See also Table 16. A fit to the form  $R_{e^+} \propto \exp(-A/\Upsilon_\gamma)$  yields  $A = 1.27 \pm 0.08 \pm 0.25$ , the first error being statistical and the second systematic. This can be compared to the asymptotic expectation of  $8/3\sqrt{2} = 1.89$ , according to eq. (48). Referring to Fig. 9, we infer that for  $\eta$  in the range 0.2-0.4 as holds for our data, the coefficient  $A$  should be about 0.6 of the asymptotic value, *i.e.*, about 1.1.

The agreement between the observed and predicted slope of  $1/\Upsilon_\gamma$  is reasonable, and

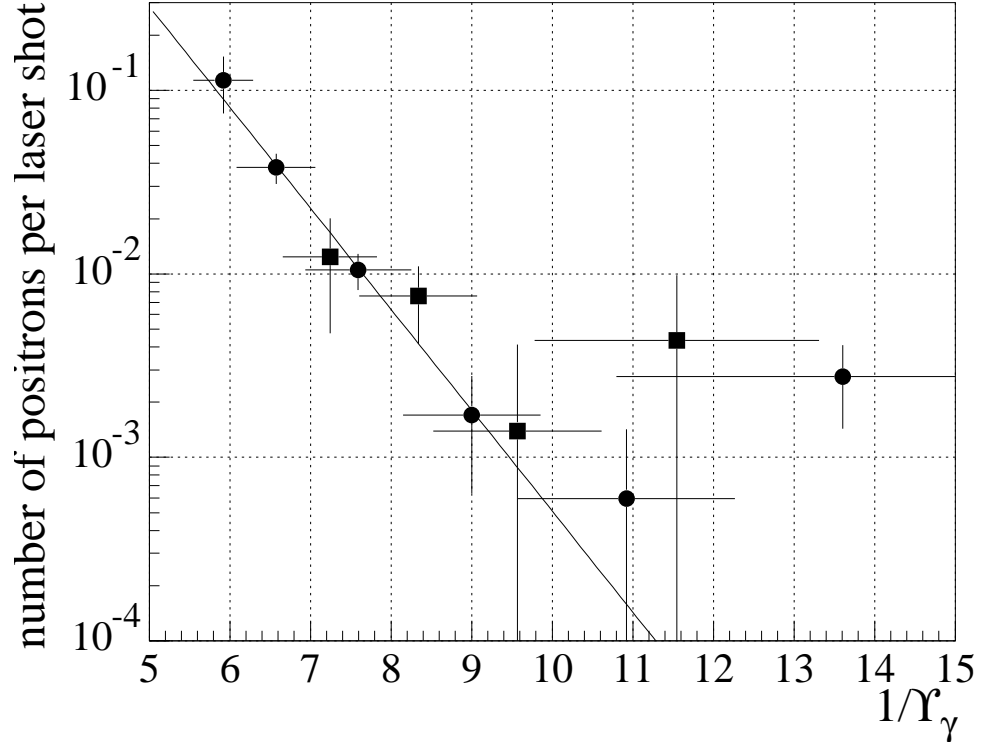


Figure 45: Number of positrons per laser shot as a function of  $1/\Upsilon_\gamma$ . The circles are the 46.6 GeV data whereas the squares are the 49.1 GeV data. The solid line is a fit to the data.

Table 16: Combined 46.6 and 49.1 GeV positron yield *vs.*  $\Upsilon_\gamma$ .

$\Upsilon_\gamma$	$N_e^+/\text{shot} \times 10^{-3}$	Energy (GeV)
$5.92 \pm 0.37$	$113 \pm 39$	46.6
$6.57 \pm 0.49$	$38.0 \pm 7.2$	46.6
$7.24 \pm 0.58$	$12.4 \pm 7.7$	49.1
$7.59 \pm 0.66$	$10.5 \pm 2.3$	46.6
$8.34 \pm 0.73$	$7.6 \pm 3.5$	49.1
$9.00 \pm 0.85$	$1.7 \pm 1.1$	46.6
$9.57 \pm 1.04$	$1.4 \pm 2.7$	49.1
$10.92 \pm 1.35$	$0.6 \pm 1.3$	46.6
$11.55 \pm 1.77$	$4.4 \pm 5.5$	49.1
$13.61 \pm 2.81$	$2.8 \pm 1.3$	46.6

supports the complementary view of pair production as the realization of vacuum polarization loops by a strong laser field, when probed by a high energy photon. For more details, see [66].

## 7 Conclusions

We have observed nonlinear QED effects in the scattering of high-energy electrons from the focus of an intense laser pulse. The peak laser intensity corresponded to a value of 0.4 for the field-strength parameter  $\eta = eE_{\text{rms}}/m\omega c$  introduced in eq. (5). In this regime, interactions involving multiple laser photons are significant.

We measured nonlinear Compton scattering, (1), with up to  $n = 4$  photons absorbed from the laser field, by observing scattered electrons with momenta smaller than those permitted by ordinary Compton scattering, as indicated in Fig. 4. Such low-energy electrons can also be produced by plural incidences of ordinary Compton scattering of a single electron. Details of the observed electron spectra unambiguously identify the presence of nonlinear Compton scattering. Furthermore, we have measured the spectrum of forward photons from  $n = 2$  nonlinear Compton scattering in a region forbidden to plural scattering.

We also observed positrons from  $e^+e^-$  pair production at the  $e$ -laser collision point. This process occurred when a high-energy backscattered photon interacted with the laser field to produce the pair by the multiphoton Breit-Wheeler process, (2). In this case, energy conservation required that at least five photons be absorbed from the laser field.

The rates for these reactions are in excellent agreement with the theoretical predictions, when the errors in the determination of the peak laser intensity are taken into account. The nonlinear dependence of these processes on the laser intensity  $I$  is clearly demonstrated and obeys the form  $I^n$ , where  $n$  is the number of the photons absorbed from the laser field. Such a dependence is predicted when  $\eta \ll 1$ .

When  $\eta$  approaches unity, another dimensionless measure of field strength becomes relevant for pair production, namely  $\Upsilon_\gamma = (2\mathcal{E}_\gamma/mc^2)(E_{\text{rms}}/E_{\text{crit}})$  as introduced in sec. 1.3. In our experiment, a peak value of 0.16 for  $\Upsilon_\gamma$  was obtained when  $\eta = 0.3$ . Our  $e^+e^-$  pair production data are also well fitted by a model of breakdown of the vacuum by the strong laser field (stimulated by a high-energy photon), in which the laser field strength is close to the QED critical field  $E_{\text{crit}} = m^2c^2/e\hbar$ , as measured by  $\Upsilon_\gamma$ .

These data are the first observation of nonlinear electrodynamic phenomena in vacuum, *i.e.*, in the interaction of light with free electrons in the absence of polarizable matter. They are also the first demonstration of light-by-light inelastic scattering with real photons.

## Acknowledgments

We thank the SLAC staff for their extensive support of this experiment. The laser system could not have been completed without support from members of the Laboratory for Laser Energetics at U. Rochester. T. Blalock was instrumental in the construction of the laser system and its installation at SLAC. We also thank U. Haug, A. Kuzmich, and D. Strozzi for participation in recent data collection, and A. Odian and P. Chen for many useful conversations. KTM thanks J.A. Wheeler for continued inspiration. This work was supported in part by DOE grants No. DE-FG02-91ER40671, No. DE-FG02-91ER40685, No. DE-FG05-91ER40627, and contract No. DE-AC03-76SF00515.

## 8 Appendix A: Simulation of the Nonlinear QED Processes

For a detailed simulation of strong field QED effects in electron-laser collisions, two independent programs were used and good agreement was found. The processes considered in these simulations are linear and nonlinear Compton scattering (1), plural Compton scattering (38), multiphoton Breit-Wheeler pair production (2), and trident production (53), in a circularly or linearly polarized laser field. For pair creation, we account for both the production of the high-energy photon (through a single or multiphoton interaction) and its subsequent multiphoton interaction within the same laser focus to produce the pair. Further Compton scatters of the positron (or electron) are also taken into account. The formal expressions for the rates of these processes are taken from [7, 8] and have been summarized in sec. 2 above.

The first simulation [67] tracked individual beam electrons, distributed according to the electron density in the beam bunch, through the laser field. Based on calculated interaction probabilities and random numbers, the program decided at each step along the path whether an interaction occurred, in which case the resulting particles were then tracked from the interaction point on.

In a second approach [70], reaction rates and energy spectra of final particles were obtained by numerical integration of the differential cross sections over a space-time grid around the laser focus. This method has the advantage of being free from statistical fluctuations and was used for comparison with experimental data. Details of this method are presented in secs. 8.2-8.6 of this appendix.

### 8.1 Lookup Tables

Since the parameters characterizing the electron beam and the laser pulse fluctuate from event to event, a simulation of individual collisions was needed for a meaningful comparison between theory and experiment. Because the numerical integration took a considerable amount of time, the final particle spectra were pre-calculated for a variety of interaction parameters and the results were stored in lookup tables. Each of these tables was associated with one of the parameters, and contained the results obtained by stepping this parameter through the range covered by the experiment, while keeping all other parameters at their nominal values. The parameters chosen to describe the laser pulse were  $\eta_{\text{peak}}$  (the  $\eta$ -value of the laser field at the focus), the effective focal spot area  $A_{\text{eff}}$ , and the pulsewidth  $\tau$ , while the electron beam was characterized by  $\sigma_x$ ,  $\sigma_y$  and  $\sigma_t$ . By employing these lookup tables in the analysis program, a simulation of the total yield and spectra of electrons, positrons and high-energy photons produced at the IP was obtained for each event.

To predict the number of particles intercepted by a row of ECAL, the corresponding spectrum was integrated over the momentum range covered by that row. The correlation between the particle momentum and impact point at ECAL was obtained by a detailed calculation of charged particle trajectories originating at the IP (see Fig. 16). The calculation used the measured field maps of the six permanent magnets.

The prediction of the total high-energy photon yield allowed us to calculate  $R_{\text{overlap}} =$



$N_\gamma^{\text{exp}}/N_\gamma^{\text{sim}}$ , the ratio of experimentally observed and simulated number of photons produced in the collision. This ratio served as a measure of overlap quality and was used in the event selection. Furthermore, the ratio  $R_{\text{overlap}}$  allowed an online estimate of the temporal offset  $\Delta t$  between the electron and laser pulse, assuming perfect spatial overlap. For this purpose, an additional lookup table was needed with  $\Delta t$  as parameter.

## 8.2 The Numeric Integration Simulation

In the numeric integration simulation, the electron and laser beams were represented by particle density distributions, and their various interactions were accounted for simultaneously by multiplying the densities with the relevant interaction probabilities. Space and time were divided in small elements, and the interaction yields were computed for each one of them. This method contrasts with the Monte-Carlo approach, where a single high-energy particle was stepped through the laser beam, and at each step a decision was made regarding which one of a number of possible processes took place, based on a pseudo-random number generator. The main advantage of the numeric integration based simulation was speed of execution.

Several processes were simulated with the numeric integration code. The primary process is the  $n^{\text{th}}$ -order Compton scattering (1) of beam electrons with laser photons. A number of secondary processes were considered, involving the scattered electrons and high-energy photons resulting from the Compton scattering inside the laser focal area. These secondary processes include further  $n^{\text{th}}$ -order Compton scatterings off laser photons (*i.e.*, plural Compton scattering (38)), as well as pair production by the high-energy photons via interaction with several laser photons, (2) and (53). In all the above cases, the detailed geometry of the interaction region was taken into account, along with the attenuation of the initial electron beam due to the Compton scattering as it traversed the laser focus.

## 8.3 Beam Densities

To describe the electron and laser beams with crossing angle  $\alpha = 17^\circ$ , two coordinate systems (CS) were defined, as shown in Fig. 46. The first one, called the electron CS,  $(x, y, z)$ , has its  $z$ -axis parallel to the direction of the electron beam propagation. The second coordinate system, called the laser CS,  $(x', y', z')$ , has its  $z'$ -axis parallel to the direction of the laser propagation. The origin  $O'$  of the  $(x', y', z')$  system was at the laser focus, which, in general, was offset from the  $z$  axis of the electron CS. The origin of the electron CS was chosen so that the laser focus has coordinate  $z = 0$ , *i.e.*,  $(x_{\text{off}}, y_{\text{off}}, 0)$ .

The electron beam density  $\rho_e$  was taken as Gaussian:

$$\rho_e(x, y, z, t) \propto \exp \left[ -\frac{x^2}{2\sigma_x^2} - \frac{y^2}{2\sigma_y^2} - \frac{(z - c(t + t_{\text{off}}))^2}{2\sigma_z^2} \right], \quad (77)$$

where the rms quantities  $\sigma_x$ ,  $\sigma_y$ , and  $\sigma_z$  were taken from measurements of the electron beam profile, and  $t_{\text{off}}$  is a possible time offset between the electron and laser pulses. Typically,  $\sigma_x$  was different from  $\sigma_y$ .

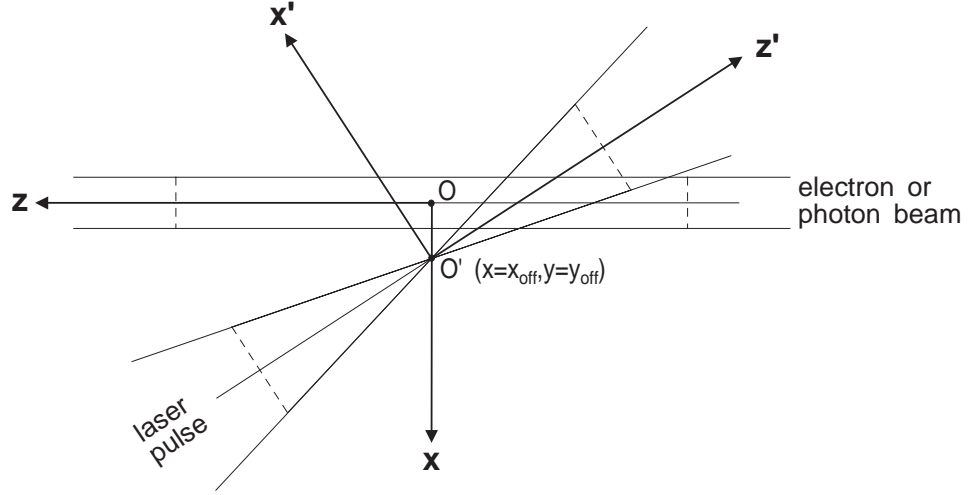


Figure 46: The two coordinate systems employed by the numeric integration code, as described in text.

The laser beam density  $\rho_\omega$  (laser intensity profile) was also taken as Gaussian:

$$\rho_\omega(x', y', z', t) \propto \exp \left[ -\frac{r'^2}{2\sigma_{r'}^2(z')} - \frac{(z' - ct)^2}{2\sigma_{z'}^2} \right], \quad (78)$$

where  $r' = \sqrt{x'^2 + y'^2}$ . While  $\sigma_{z'}$  was a constant taken from measurements of the laser pulses, the transverse size of the laser beam varied according to the laws of diffraction [57]:

$$\sigma_{r'}(z') = \frac{f_\# \lambda}{\pi} \sqrt{\frac{A_{\text{eff}}}{A_0} + \left( \frac{z'}{z_R} \right)^2}, \quad (79)$$

where the Rayleigh range  $z_R$  and the diffraction limited focal-spot area  $A_0$  are related to the laser wavelength  $\lambda$  and the  $f_\#$  of the focusing system ( $\approx 6$  in the present experiment) via

$$z_R = \frac{4}{\pi} f_\#^2 \lambda, \quad A_0 = \frac{2}{\pi} (f_\# \lambda)^2, \quad (80)$$

and  $A_{\text{eff}}$  is the effective focal-spot area measured in the laboratory (see sec. 3.4.3 of [48]).

## 8.4 Effective Crossing Angle

Because the laser beam was focused, the laser photons had a spread of angles relative to the optical axis. When considering an interaction with the laser at point  $(x'_0, y'_0, z'_0)$  in the laser coordinate system, we took the effective direction of the laser-photon momentum to be along the trajectory

$$r'(z') = r'_0 \sqrt{\frac{A_{\text{eff}}/A_0 + (z'/z_R)^2}{A_{\text{eff}}/A_0 + (z'_0/z_R)^2}}, \quad (81)$$

as illustrated in Fig. 47. On this trajectory, the laser intensity (78) remained a constant fraction of its value on the optic axis.

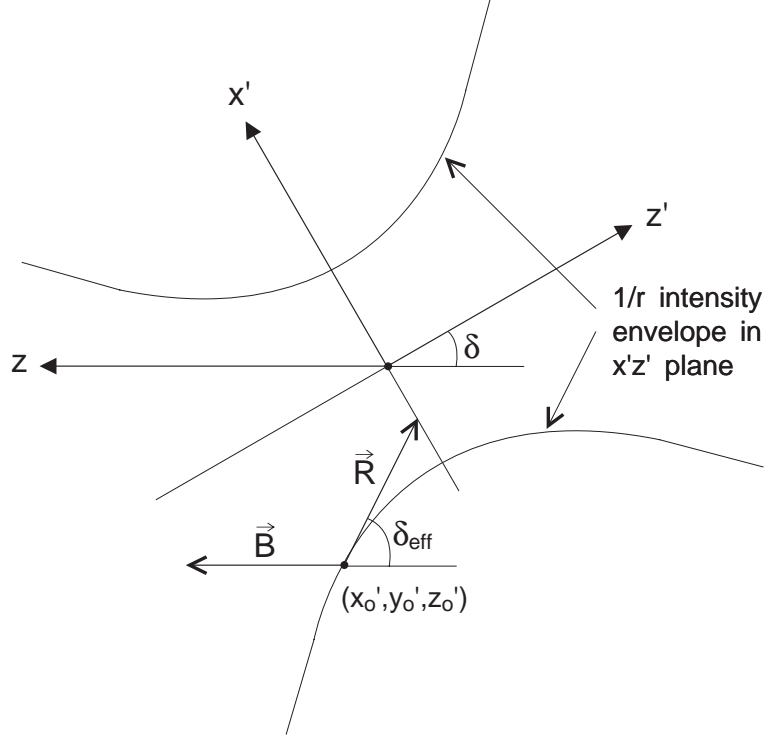


Figure 47: Effective crossing angle between the laser photons propagating along  $\vec{R}$  and the electron beam moving along  $\vec{B}$  at the interaction point  $(x'_0, y'_0, z'_0)$ .

## 8.5 Space-Time Integration

To find the total interaction rates for the various processes discussed in the previous section, we needed to integrate them over space and time. For this purpose, both space and time were divided into small space-time elements (STE), and for each of them the yields of the beam-laser interactions were calculated. At the end of the integration, the different space-time element results were combined to give the total interaction rate. In this approach, it was assumed that the electron and laser photon densities remained constant within each STE, and therefore the integration grid needed to be fine enough that this was accurately true. In addition, the definition of the integration grid needed to take into account the fact that the laser beam was focused, and therefore the step sizes should become smaller as we approached closer to the laser focus.

The integration grid in space was defined in the laser CS, and in units of  $\sigma_{x'}(z')$ ,  $\sigma_{y'}(z')$ , and  $\sigma_{z'}$ . In this case, a single STE had a spatial volume

$$\begin{aligned} dV(z') &= dx'(z') \cdot dy'(z') \cdot dz' \\ &= \frac{2n_{x'}^\sigma \sigma_{x'}(z')}{n_x^\Delta} \cdot \frac{2n_{y'}^\sigma \sigma_{y'}(z')}{n_y^\Delta} \cdot \frac{2n_{z'}^\sigma \sigma_{z'}}{n_z^\Delta}, \end{aligned} \quad (82)$$

where

$$\begin{aligned}
n_{x'}^\sigma, n_{y'}^\sigma, n_{z'}^\sigma &: \text{size of the integration volume in } x', y', z', \\
&\text{in units of } \sigma_{x'}(z'), \sigma_{y'}(z'), \sigma_{z'} \\
n_{x'}^\Delta, n_{y'}^\Delta, n_{z'}^\Delta &: \text{number of elements in the integration} \\
&\text{volume along } x', y', z' .
\end{aligned}$$

It is clear from the above expressions that the STE dimensions along the  $x'$ -axis and the  $y'$ -axis depend on  $z'$ . An example of the integration grid in the  $x' - z'$  plane is shown in Fig. 48, in which  $n_{x'}^\sigma = n_{z'}^\sigma = 3$  and  $n_{x'}^\Delta = n_{z'}^\Delta = 8$ . The step size  $c \, dt$  in time was kept comparable to the step size  $dz'$  along the  $z'$ -axis.

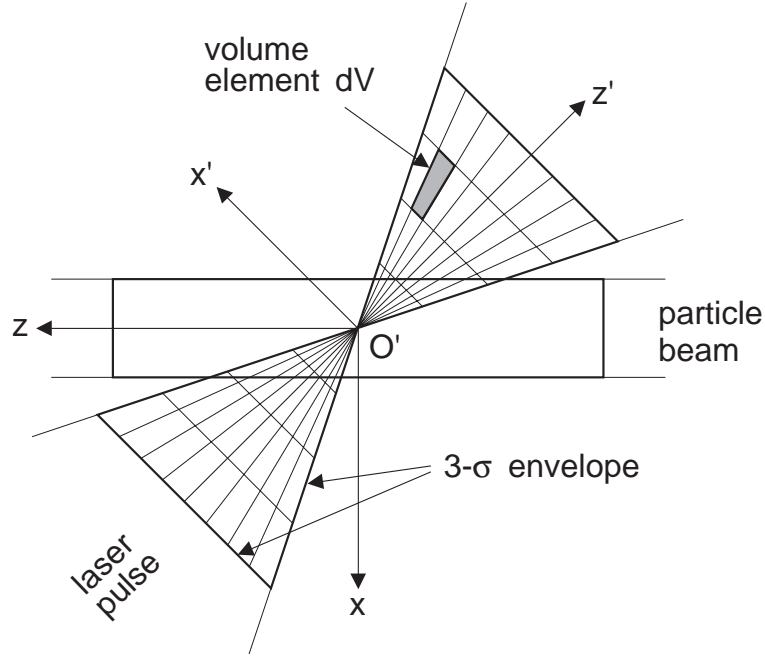


Figure 48: Schematic of the integration grid along the  $x'$ -axis and the  $z'$ -axis. The variable size of the volume element  $dV$  as a function of  $z'$  is evident. For this example  $n_{x'}^\sigma = n_{z'}^\sigma = 3$  and  $n_{x'}^\Delta = n_{z'}^\Delta = 8$ .

The integration over space and time for a specific process  $X$  (illustrated here as nonlinear Compton scattering) proceeded as follows:

1. For a given time  $t$ , loop over all the volume elements  $dV$  in the integration grid.
2. Use the expressions given in sec. 2 to find the interaction rate  $W_X$  (this involved integration over the energy, with a specified step size), and thus the interaction yield from:

$$N_X^{\text{STE}} = W_X \cdot dV \cdot dt. \quad (83)$$

3. Add the yield found to the total up to this point yield for process  $X$ , *i.e.*:

$$N_X^{\text{total}} = N_{X_0}^{\text{total}} + N_X^{\text{STE}}. \quad (84)$$

4. Advance in time by a step size of  $c \, dt$ , and start over at step 1.

Figure 49 shows how the spatial integration grid moved to stay centered on the beam pulses during two consecutive time steps at  $t$  and  $t + dt$ .

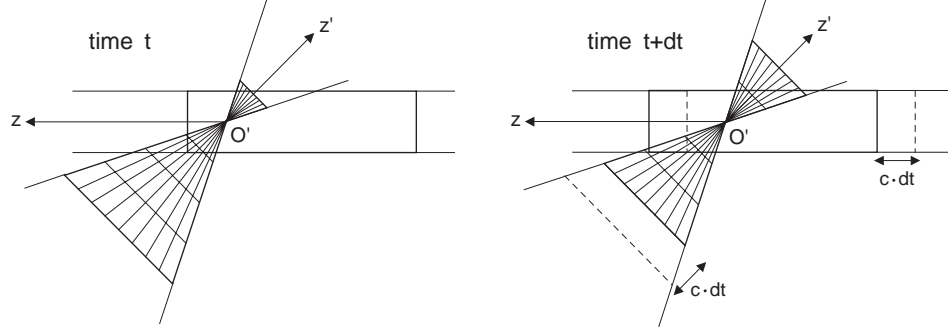


Figure 49: The spatial integration grid at two consecutive time steps.

## 8.6 Secondary Processes

The above space-time integration essentially refers only to the interaction of the initial electron beam with the laser photons, *i.e.*, the  $n^{\text{th}}$ -order Compton scattering. We will refer to this process as the primary process. The products of such an interaction remained inside the laser field for some time, and therefore could undergo further interactions with the laser photons. These are the so-called secondary processes. In particular, the scattered electrons could undergo further Compton scatterings, while the produced high-energy photons could absorb several laser photons, resulting in pair production according to the multiphoton Breit-Wheeler process.

This led to an additional integration, over time  $t'$  for each volume element  $dV$ , to account for the secondary processes. The volume element was kept constant in size as it moved along the  $z$ -axis of the electron beam, while at the same time the laser pulse continued to propagate along the  $z'$ -axis. This is shown schematically in Fig. 50. Here, the basic assumption was made that all the produced particles were moving along the  $z$ -axis. This is fairly accurate, since the angular divergence of the products of the Compton scattering are of the order of  $\sim 1/\gamma$ , *i.e.*, about  $10 \, \mu\text{rad}$ . The step size  $c \, dt'$  was kept comparable to the linear dimensions of the volume element  $dV$  at the current location  $(x'_s, y'_s, z'_s)$ . The starting point for the time integration was, of course, the location in time of the primary STE. The end point was taken to be the time at which the secondary particle left the laser field. During the computation of the secondary processes, the interactions of the produced particles with the electron beam were ignored.

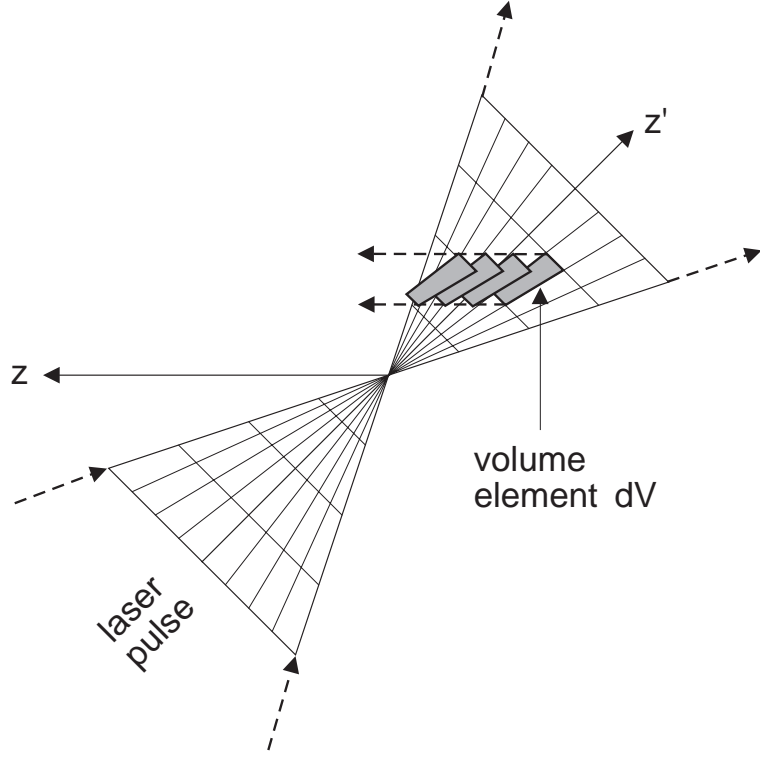


Figure 50: Integration grid for secondary processes, as defined in text.

## 8.7 Simulation of the CCD Tracking Spectrometer

For Monte-Carlo studies of systematic effects in the CCD tracking spectrometer, data sets were created by generating a Poisson-distributed number of pairs for each simulated event [67]. Gaussian-distributed angular displacements were introduced to account for the electron beam divergence, the Bethe-Heitler pair-creation process, and multiple-scattering in each CCD plane. The CCD-plane intercept positions were converted into CCD hit coordinates for each CCD plane. Simulated thermal noise hits were then added, and “raw hit” records written for each event in the same format as written by the data-acquisition system. These Monte-Carlo data sets were used for studies of systematic effects in the reconstruction and spectra-fitting algorithms.

## 9 Appendix B: ECAL Analysis Details

### 9.1 Calibration Data

#### 9.1.1 Coordinates, Indices, and ECAL Segmentation

The FFTB dump magnets dispersed the Compton scattered electrons vertically, which we call the  $y$  direction. There was therefore a correlation between an electron’s momentum and the  $y$ -coordinate at which the electron entered the ECAL, as shown in Fig. 16.

The ECAL (see Fig. 17) was segmented into horizontal rows, which we label by subscript  $i$ . Usable signal could be found in only the top four rows. Typically, signals in row 4 were of order 1% of those in row 1.

The ECAL was segmented vertically into four columns, often grouped as ‘inner’ and ‘outer’. The ECAL was segmented longitudinally into four segments. The last segment contained little signal from electrons that entered the front of the ECAL, but was useful in characterizing backgrounds from the “splash” of  $n = 1$  Compton scattered electrons that struck nearby obstacles.

In the iterative analysis, described below in sec. 9.2.1, the first three longitudinal segments were summed, and the two inner columns of each row were summed together into a logical segment  $I$  consisting of the two inner physical segments; likewise, a logical segment  $O$  was formed from the two outer physical segments. The index  $i$  refers to these logical segments.

### 9.1.2 ECAL Calibrations and Response Kernels

Extensive studies of ECAL performance have been made in parasitic runs of the FFTB. Pulses of 1-100 electrons were obtained at selected momenta in the range 5-30 GeV. The beam-spot size was about 1 mm. The vertical position of the ECAL was varied in small steps.

**ECAL Response Functions  $X_i(y)$**  From the calibration data, the energy response of each ECAL segment  $i$  to an electron entering the front of ECAL at height  $y$  with energy  $E$  was determined. The fractional (or normalized) response,  $X_i(y, E)$ , for a given geometrical configuration was found to be reasonably independent of energy in the range 5-30 GeV. Hence, we summarized calibration data with the energy-independent response  $X_i(y)$ , where the normalization condition was

$$\sum_i X_i(y) = 1. \quad (85)$$

The ADC gain conversion constant was normalized so that the energy deposited by an electron in the inner segments was equal to 100% of the electron’s energy. That is,

$$\sum_i X_{I,i}(y) = 1, \quad (86)$$

where subscript  $I$  refers to the inner segments.

The ECAL calibrations revealed that the ratio of the energy deposited in the outer segments to that deposited in the inner segments is 0.0713. Therefore,

$$\sum_i X_{O,i}(y) = 0.0713. \quad (87)$$

Figure 51 shows calibration data for response functions  $X_I$  and  $X_O$ , along with fits described below.

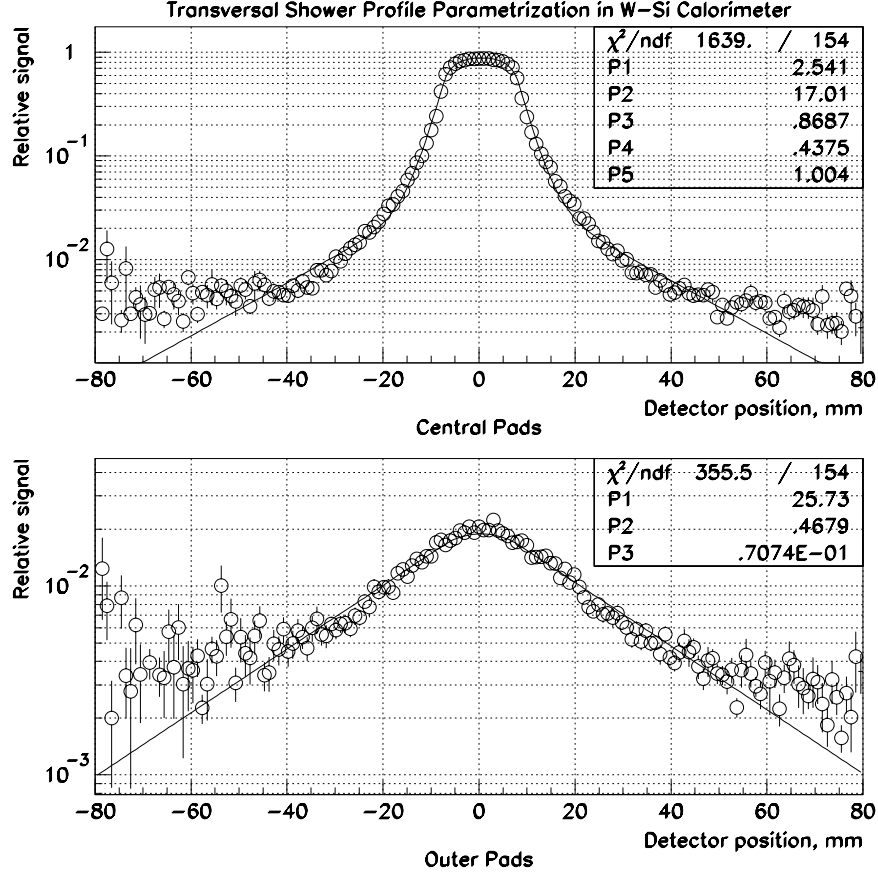


Figure 51: Top: the response function  $X_I(\Delta y)$  for inner columns of the ECAL, summed over longitudinal segments 1-3. Bottom: the function  $X_O(\Delta y)$  for outer columns. Circles = data; curve = calculation based on eq. (90).

**The Response Kernels  $K_i(y, y')$**  Guided in part by EGS simulations [64], the calibration data were analyzed to extract the response kernel  $K_i(y, y')$ , defined such that when an electron entered the ECAL at height  $y$ , it deposited fractional energy  $K\delta y/1.0713$  in a horizontal slice of thickness  $\delta y$  at height  $y'$  within segment  $i$ . To a good approximation, the kernel depends on positions  $y$  and  $y'$  only through the absolute value of their difference:  $|y - y'|$ . The factor  $1/1.0713$  in the definition of  $K$  arose from the convention that the channel gains were adjusted until the nominal energy deposited in the inner segments is exactly the incident energy, so the nominal energy deposited in inner plus outer segments was 1.0713 times the incident energy.

A different form of the kernel was assumed for the inner and outer segments. All segments in inner columns had kernels of the form

$$K_I(y, y') = \frac{w \exp(-|y - y'|/b_1)}{2b_1} +$$



$$+\frac{(1-w)\exp(-|y-y'|/b_2)}{2b_2}, \quad (88)$$

and all segments in outer columns had kernels of form

$$K_O(y, y') = 0.0713 \frac{\exp(-|y-y'|/b_3)}{2b_3}. \quad (89)$$

where  $b_1 = 1.940$ ,  $b_2 = 9.561$ ,  $b_3 = 16.908$ , and  $w = 0.703$ .

The ECAL response function,  $X_i(y)$ , were then represented in terms of an integral over the response kernel. Thus

$$X_i(y) = \int_{y_i}^{y_{i+1}} K_i(y, y') dy', \quad (90)$$

where row  $i$  spans the interval  $[y_i, y_{i+1}]$ .

### 9.1.3 Splash Coefficients

Signal electrons could only enter the front of the inner columns of the ECAL. However, many Compton-scattered electrons, primarily from  $n = 1$  scattering, initiated showers in the beampipe and other shielding above the ECAL, causing a spray of electrons and photons into the top and back of ECAL. This was the principal type of background in the ECAL, and is called “splash”. It has been characterized using  $x$ - $t$  scans, as discussed in sec. 4.3.1.

There also exists electronic crosstalk at the level of a few percent between various segments of the ECAL.

Correction for the splash background was made using the observed energy in the outer ECAL columns, in which little energy from the signal electrons was deposited, as described in sec. 9.2.2 below. For this, we used the ratio of the “splash” background in the inner segments of row  $i$  to that in the outer segments, called  $L_{ii}$ . This ratio was largest when ECAL was positioned close to the electron beam, and hence close to the trajectories of  $n = 1$  Compton-scattered electrons. Figure 52 shows the  $L_{ii}$ . To a first approximation, the “splash” ratio  $L$  is only a function of the  $y$ -coordinate of the ECAL row.

## 9.2 The Main Analysis Algorithms

The nonlinear Compton Scattering process (1) produced an energy spectrum  $f(y)$  of scattered electrons hitting the ECAL at height  $y$ . Because of fluctuations in the  $e$ -laser beam overlap, this spectrum varied from pulse to pulse. The general strategy was to reconstruct the spectrum  $f$  for each pulse and then sum over pulses.

Of course, we cannot fully reconstruct a continuous spectrum such as  $f$  from data in a detector with a finite number of segments. Rather, what we desire to reconstruct is the integral  $F_i$  of the spectrum  $f$  over segment  $i$ :

$$F_i = \int_{y_i}^{y_{i+1}} f(y) dy. \quad (91)$$

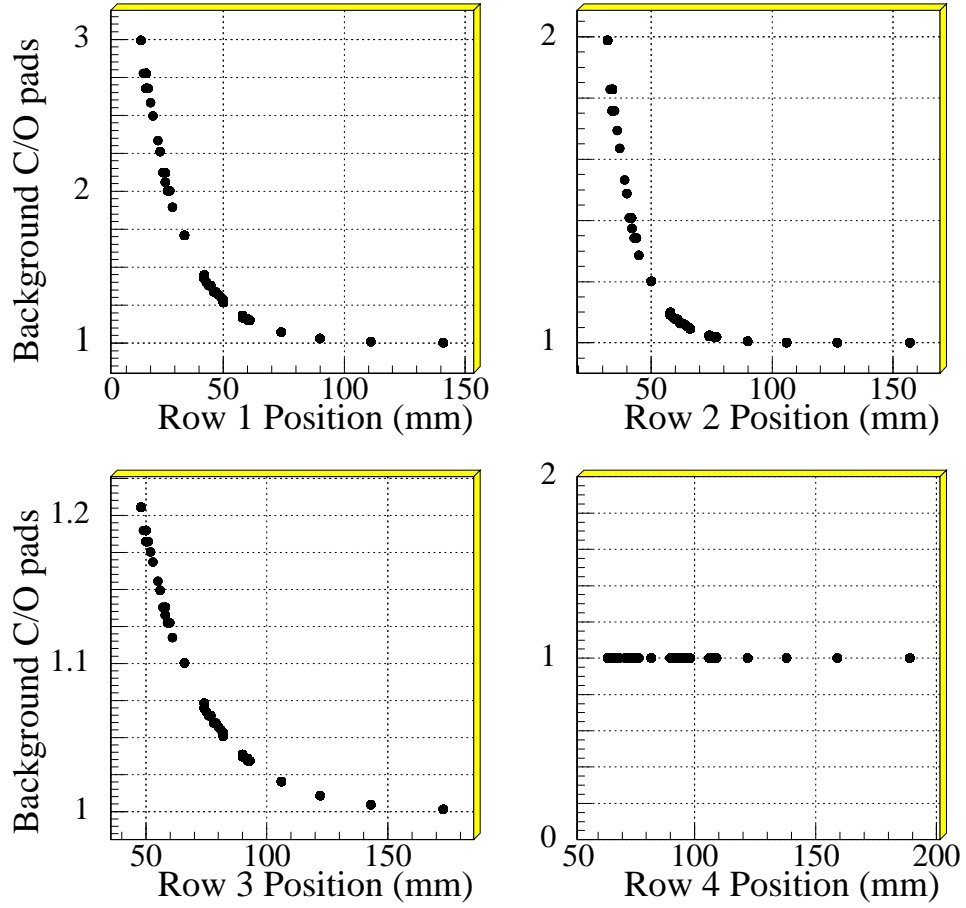


Figure 52: The “splash” coefficients  $L_{ii}$  as function of ECAL vertical position.

The spectrum  $F_i$  was obtained from the observed energy  $D_i$  in segment  $i$ . In terms of the Compton spectrum  $f$  and the detector response function  $K$ , we have

$$\begin{aligned}
 D_i &= \int dy f(y) \int_{y_i}^{y_{i+1}} K_i(y, y') dy' \\
 &= \int dy f(y) X_i(y),
 \end{aligned} \tag{92}$$

recalling eq. (90). Expression (92) is a Fredholm linear integral equation of the first kind. We solved this by constructing a matrix  $R$ , by two different methods, such that

$$F_i = \sum_j R_{ij} D_j. \tag{93}$$

### 9.2.1 Iterative method

For every laser pulse, we determined a matrix  $M_{ij}$  such that the observed data  $D_i$  was related to the desired spectrum  $F_i$  by

$$D_i = \sum_j M_{ij} F_j, \quad (94)$$

and then we inverted this matrix to yield

$$F_i = \sum_j R_{ij} D_j, \quad \text{where} \quad R_{ij} = M_{ij}^{-1}. \quad (95)$$

The matrix  $M_{ij}$  was found by an iterative process [39] in which the integrals (92) were performed analytically for a “polyline” approximation to a spectrum  $f$  derived from the  $F_i$  of the previous iteration. The initial hypothesis was that  $F_i = D_i$ . Only two iterations were needed to find the reconstructed  $F_i$  to good accuracy. The index  $i$  runs from 1 to 4, corresponding to the top four rows of ECAL. For additional details, see [71].

### 9.2.2 Background Subtraction

As noted in sec. 9.1.2, about 93% of the energy from Compton-scattered electrons was deposited in the inner columns of ECAL. However, energy from background processes was more uniformly divided between the inner and outer columns. The background subtraction method is an extension of the simple prescription that the Compton signal could be obtained by subtracting the energy in the outer segments from that in the inner segments.

Let  $S$  designate energy deposited from Compton-scattered electrons entering the front of ECAL and  $B$  that deposited by the background processes (predominantly “splash” from scattered electrons that hit shielding rather than the front of ECAL). Then the observed energy  $D_I$  in the inner columns can be written as a vector with index  $i$  suppressed:

$$D_I = D_{I,S} + D_{I,B}. \quad (96)$$

We also introduced vector  $D_O$  as the observed energy in the outer columns of ECAL, which was partly due to the small leakage from electrons that entered the front of ECAL, and partly due to “splash” energy:

$$D_O = D_{O,S} + D_{O,B}. \quad (97)$$

Just as the Compton signal  $D_{I,S}$  in the inner segments was related to the Compton-spectrum vector  $F$  by eq. (94),

$$D_{I,S} = M F, \quad (98)$$

there exists a matrix  $N$  such that the Compton-leakage signal  $D_{O,S}$  in the outer segments is related by

$$D_{O,S} = N F. \quad (99)$$

The key to background subtraction is that we can relate the background energy in the inner segments to that in the outer segments according to

$$D_{I,B} = L D_{O,B}, \quad (100)$$

where matrix  $L$  is diagonal, with diagonal elements as discussed sec. 9.1.3.

Once matrices  $L$  and  $N$  were known the analysis was readily completed. The observed energy in the inner segments could then be written as

$$D_I = D_{I,S} + D_{I,B} = MF + LD_{O,B}, \quad (101)$$

while that in the outer segments was

$$D_O = D_{O,S} + D_{O,B} = NF + D_{O,B}. \quad (102)$$

On subtracting  $L$  times eq. (102) from eq. (101) and noting eq. (100) we have

$$D_I - LD_O = [M - LN]F, \quad (103)$$

and hence

$$F = [M - LN]^{-1}(D_I - LD_O). \quad (104)$$

### 9.2.3 Error Estimates

In addition to the statistical errors related directly to the number of electrons hitting the ECAL, the analysis assigned errors that represent the systematic uncertainty due to limitations of the numerical algorithms.

Since an iterative procedure was used to unfold the Compton spectrum, it was easy to generate trial data from a known hypothesis  $f(y)$ , calculating both the corresponding ideal spectrum  $F_i$  and the ‘observed’ data  $D_i$ , and finally reconstructing a spectrum  $F'_i$  from the  $D_i$ . This was done in the presence of some model background as well. We then repeated this check for a reasonable class of trial spectra  $f(y)$  and accumulated error estimates:

$$\sigma_i^2 = \langle (F_i - F'_i)^2 \rangle. \quad (105)$$

The result of the study for row 1 was that  $\sigma_1/F_1 \approx 0.05$ .

However, the data in a lower row was heavily influenced by feed-down from the rows above, given that the Compton spectrum is steeply falling. Therefore, the biggest uncertainty in row  $j$  was the uncertainty in the feed-down from rows with  $i < j$ , and the uncertainty in row  $j$  could be propagated all the way back to that in row 1 [39]

### 9.2.4 Aperture Function Method

In the second method [67], the calorimeter segments were not combined, but were treated individually. As remarked in sec. 4.3.1, the integral  $F_i$  of the spectrum over segment  $i$  can be expressed as

$$\begin{aligned} F_i &= \sum_j R_{ij} D_j = \int dy f(y) \sum_j R_{ij} X_j(y) \\ &= \int dy f(y) g_i(y), \end{aligned} \quad (106)$$

where

$$g_i(y) = \sum_j R_{ij} X_j(y). \quad (107)$$

Comparing eq. (107) with eq. (91), we see that the  $g_i$  (called “aperture functions”) should obey

$$g_i(y) = \begin{cases} 1, & y_i < y < y_{i+1}, \\ 0, & \text{otherwise.} \end{cases} \quad (108)$$

The matrix elements  $R_{ij}$  for a given geometric configuration of ECAL and shielding were found by a  $\chi^2$ -minimization process involving the  $g_i$ . Briefly

$$\chi^2 = \sum_{i,k} \frac{\left( \sum_j R_{ij} X_j(y_k) - g_i(y_k) \right)^2}{\sigma_{ik}^2}, \quad (109)$$

where the deviates were evaluated at  $y_k$  spaced 1 mm apart. Some care in choosing the ‘errors’ (or tolerances)  $\sigma_{ik}$  was required. A sense of how well the procedure worked is given in Fig. 53, which shows the aperture functions  $g_i$  for four rows in ECAL.

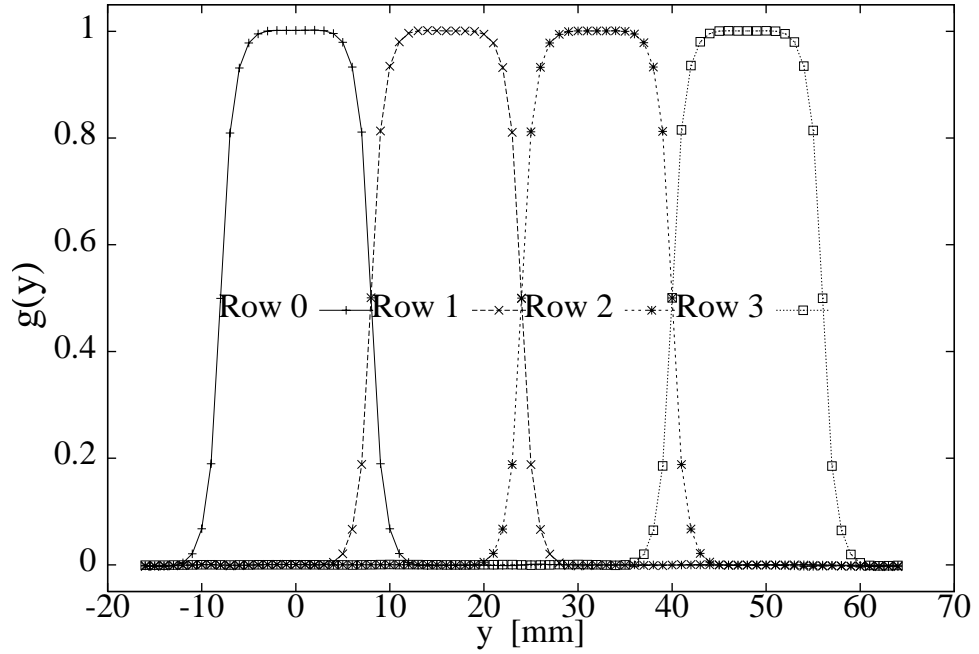


Figure 53: The aperture functions defined by eq. (107) for the top four rows of ECAL.

In this analysis, the background energy in segment  $i$  was written as  $B_i$ . Since this background was dominated by showers of  $n = 1$  Compton scatters (rather than nonlinear Compton scatters), we expect that vector  $B_i$  varied from event to event only in overall

normalization. The relative values of  $B_i$  were determined from  $x$ - $t$  scans, and normalized such that  $\sum B_i$  was the total background energy from a single Compton scattering.

The reconstruction matrix  $R_{ij}$  introduced in eqs. (95) and (106) should produce no signal when applied to the background vector:

$$\sum_j R_{ij} B_j = 0. \quad (110)$$

This condition was enforced during the determination of the  $R_{ij}$  by adding a term to the  $\chi^2$  (109):

$$\begin{aligned} \chi^2 = & \sum_{i,k} \frac{\left(\sum_j R_{ij} X_j(y_k) - g_i(y_k)\right)^2}{\sigma_{ik}^2} + \\ & + \sum_{i,k} \frac{\left(\sum_j R_{ij} B_j\right)^2}{\sigma'^2}, \end{aligned} \quad (111)$$

The two analyses for the nonlinear Compton spectrum  $F_i$  yielded results that were equal within the assigned errors [71]. Another indication of the equivalence of the two analyses is that the iterative background subtraction procedure formally satisfies the condition (110). Thus, the basic difference between the two methods was in their procedures to calculate the matrix  $R$ .

## References

- [1] C. Bula *et al.*, Phys. Rev. Lett. **76**, 3116 (1996).
- [2] D. Burke *et al.*, Phys. Rev. Lett. **79**, 1626 (1997).
- [3] N.D. Sengupta, Bull. Math. Soc. (Calcutta) **44**, 175 (1952).
- [4] H.R. Reiss, J. Math. Phys. **3**, 59 (1962); Phys. Rev. Lett. **26**, 1072 (1971).
- [5] L.S. Brown and T.W.B. Kibble, Phys. Rev. **133A**, 705 (1964).
- [6] I.I. Goldman, Sov. Phys. JETP **19**, 954 (1964); Phys. Lett. **8**, 103 (1964).
- [7] A.I. Nikishov and V.I. Ritus, Sov. Phys. JETP **19**, 529, 1191 (1964); **20**, 757 (1965); **25**, 1135 (1967).
- [8] N.B. Narozhnyi, A.I. Nikishov and V.I. Ritus, Sov. Phys. JETP **20**, 622 (1965).
- [9] For a review, see J.H. Eberly, Prog. in Opt. **VII**, 359 (1969).
- [10] V.B. Berestetskii, E.M. Lifshitz and L.P. Pitaevskii, *Quantum Electrodynamics*, 2nd ed. (Pergamon Press, New York, 1982), secs. 40 and 101.

- [11] T.W.B. Kibble, Phys. Rev. **138**, B740, (1965); **150**, 1060 (1966); Phys. Rev. Lett. **16**, 1054 (1966); *Cargèse Lectures in Physics*, Vol. 2, ed. by M. Lévy (Gordon and Breach, New York, 1968), p. 299.
- [12] F. Sauter, Z. Phys. **69**, 742 (1931); **73**, 547 (1931).
- [13] O. Klein, Z. Phys. **53**, 157 (1929);
- [14] W. Heisenberg and H. Euler, Z. Phys. **98**, 718 (1936).
- [15] J. Schwinger, Phys. Rev. **82**, 664 (1951).
- [16] T.J. Englert and E.A. Rinehart, Phys. Rev. A **28**, 1539 (1983).
- [17] S.-Y. Chen, A. Maksimchuk and D. Umstadter, Nature **396**, 653 (1998);  
<http://xxx.lanl.gov/ps/physics/9810036>
- [18] K.T. McDonald and K. Shmakov, Princeton U. preprint (Feb. 28, 1998);  
<http://puhep1.princeton.edu/~mcdonald/accel/dressing.ps>
- [19] C.I. Moore, J.P. Knauer, and D.D. Meyerhofer, Phys. Rev. Lett. **74**, 2439 (1995).
- [20] D.D. Meyerhofer, J.P. Knauer, S.J. McKnaught, and C.I. Moore, J. Opt. Soc. Am. **B13**, 113 (1996).
- [21] J.L. Hsu *et al.*, Proc. PAC97 (IEEE, Vancouver, Canada, 1997), p. 684;  
<http://www.triumf.ca/pac97/papers/pdf/7V021.PDF>
- [22] M.S. Zolotorev, S. Chattopadhyay and K.T. McDonald, Princeton U. preprint (Feb. 21, 1998);  
<http://puhep1.princeton.edu/~mcdonald/accel/vacuumaccel.ps>
- [23] P.H. Bucksbaum *et al.*, Phys. Rev. Lett. **58**, 349 (1987).
- [24] G. Malka, E. Lefebvre and J.L. Miquel, Phys. Rev. Lett. **78**, 3314 (1997).
- [25] I. Pomeranchuk, J. Phys. (USSR) **2**, 65 (1940).
- [26] J. Schwinger, Proc. Nat. Acad. Sci. **40**, 132 (1954).
- [27] C. Kouveliotou *et al.*, Nature **393**, 235 (1998);  
<http://xxx.lanl.gov/ps/astro-ph/9809140>
- [28] T. Erber, Rev. Mod. Phys. **38**, 626, (1966).
- [29] A. Belkacem *et al.*, Phys. Lett. **B177**, 211 (1986); **B206**, 561 (1988); R. Medenwaldt *et al.*, Phys. Lett. **B227**, 483 (1989).

- [30] J. Schweppe *et al.*, Phys. Rev. Lett. **51**, 2261 (1983); T. Cowan *et al.*, Phys. Rev. Lett. **56**, 444 (1986); W. Koenig *et al.*, Phys. Lett. **B218**, 12 (1989); P. Salabura *et al.*, Phys. Lett. **B245**, 153 (1990); H. Tsertos *et al.*, Z. Phys. A **342**, 79 (1992).
- [31] M. Bell and J.S. Bell, Part. Acc. **24**, 1 (1988).
- [32] R. Blankenbecler and S.D. Drell, Phys. Rev. Lett. **61**, 2324 (1988).
- [33] M. Jacob and T.T. Wu, Nucl. Phys. **B303**, 373, 389 (1989).
- [34] P. Chen and K. Yokoya, Phys. Rev. Lett. **61**, 1101 (1988); V.N. Baier, V.M. Katkov and V.M. Strakhovenko, Nucl. Phys. **B328**, 387 (1989).
- [35] R. Bonvincini *et al.*, Phys. Rev. Lett. **62**, 2381 (1989).
- [36] The NLC Design Group, SLAC-474/LBNL-5424/UCRL-ID-124161/UC-414 (1996).
- [37] D.M. Volkov, Z. Phys. **94**, 250 (1935).
- [38] O. Klein and Y. Nishina, Z. Phys. **52**, 853 (1929).
- [39] K.D. Shmakov, Ph.D. Dissertation, U. Tennessee (1997);  
<http://www.slac.stanford.edu/~shmakov/phd.ps>
- [40] U. Fano, J. Opt. Soc. **39**, 859 (1949).
- [41] G. Breit and J.A. Wheeler, Phys. Rev. **46**, 1087 (1934).
- [42] E. Brezin and C. Itzykson, Phys. Rev. D **2**, 1191 (1970).
- [43] C. Bula and K.T. McDonald, E-144 Internal Note (Feb. 28, 1997);  
<http://www.slac.stanford.edu/exp.e144/ps/trident.ps>
- [44] T. Koffas and A.C. Melissinos, E-144 Internal Note (Apr. 10, 1998);  
[http://www.slac.stanford.edu/exp.e144/ps/trident\\_note.ps](http://www.slac.stanford.edu/exp.e144/ps/trident_note.ps)
- [45] V. Balakin *et al.*, Phys. Rev. Lett. **74**, 2479 (1995).
- [46] T. Kotseroglou, Ph.D. Thesis, U. Rochester, UR-1459 (1996).
- [47] T. Kotseroglou *et al.*, Nucl. Instr. and Meth. **A383**, 309 (1996).
- [48] S.J. Boege, Ph.D. Thesis, U. Rochester, UR-1458 (1996);  
<http://www.slac.stanford.edu/~boege/ps/clq.ps>
- [49] C. Bamber *et al.*, Laser Phys. **7**, 135 (1997).
- [50] D. Strickland and G. Mourou, Opt. Comm. **55**, 447 (1985); M. Pessot, P. Maine and G. Mourou, Opt. Comm. **62**, 419 (1987).



- [51] W.S. Martin and J.P. Chernoch, U.S. Patent 3633126 (1972); M.J. Shoup III and J.H. Kelly, presented at CLEO '89, Baltimore, MD, (April 1989).
- [52] O.E. Martinez, IEEE J. Quan. Elec. **QE-23**, 59 (1987).
- [53] R.S. Craxton *et al.*, IEEE J. Quan. Elec. **QE-17**, 1782 (1981).
- [54] Model OAP 12-017-036Q, Space Optics Research Labs (Chelmsford, MA).
- [55] M.C. Ross, *et al.*, 1991 IEEE Part. Accel. Conf. (1991), Vol. 2, p. 1201.
- [56] G. Bowden, *et al.*, Nucl. Instr and Meth. **A368**, 579 (1996).
- [57] A.E. Siegman, *Lasers*, University Science Books (1986), p. 386.
- [58] RF/Microwave fiber-optic transmitter, model 3540A; receiver, model 4510A, Ortel Co.; Optical fiber cable, model 6HJ-9336A, Sumitomo Electric Industries Ltd., (Yokohama, Japan).
- [59] Model 1000 Timing Stabilizer, Lightwave Electronics Co., (Mountain View, CA); see also M.J.W. Rodwell, D.M. Bloom and K.J. Weingarten, IEEE J. Quant. Elec. **25**, 817 (1989).
- [60] S.H. Rokni *et al.*, SLAC-PUB-6784-REV (1996); submitted to Health Phys.
- [61] R. Holtzapple, Ph.D. thesis, Stanford University; SLAC-0487 (1996).
- [62] S.C. Berridge *et al.*, IEEE Trans. Nuc. Sci. **NS-37**, 1191 (1990).
- [63] E. Prebys, E-144 Internal Note (1992);  
<http://www.slac.stanford.edu/exp/e144/ps/rabbit.ps>
- [64] *The Electron-Gamma Shower (EGS4) Code System*, SLAC-Report-265 (Dec. 1985).
- [65] C. Field, Nucl. Instr. and Meth. **360**, 467 (1995).
- [66] T. Koffas, Ph.D. Dissertation, U. Rochester UR-1521 (1998).
- [67] Glenn A. Horton-Smith, Ph.D. Dissertation, Stanford U., SLAC-Report-529 (1998);  
<http://www.slac.stanford.edu/pubs/slacreports/slac-r-529.htm>
- [68] V.I. Ritus, Nucl. Phys. **B44**, 236 (1972).
- [69] K.A. Thompson and P. Chen, SLAC-PUB-7776, SLAC-PUB-7869) (Oct. 1998);  
<http://www.slac.stanford.edu/pubs/slacpubs/7000/slac-pub-7776.html>  
<http://www.slac.stanford.edu/pubs/slacpubs/7000/slac-pub-7869.html>
- [70] C. Bula, E-144 Internal Note (June 1997);  
<http://www.slac.stanford.edu/exp/e144/ps/nidoc.ps>
- [71] K.T. McDonald, E-144 Internal Note (Dec. 1996);  
[http://www.slac.stanford.edu/exp/e144/ps/glenn\\_kostya.ps](http://www.slac.stanford.edu/exp/e144/ps/glenn_kostya.ps)